Design and Control of a Compliant Joint for Upper-body Exoskeletons in Physical Assistance

li, zhongyi

Publication date:
2020

Document Version
Publisher's PDF, also known as Version of record

DESIGN AND CONTROL OF A COMPLIANT JOINT FOR UPPER-BODY EXOSKELETONS IN PHYSICAL ASSISTANCE

BY
ZHONGYI LI

DISSERTATION SUBMITTED 2020

AALBORG UNIVERSITY
DENMARK

Design and Control of a Compliant Joint for Upper-body Exoskeletons in Physical Assistance

Ph.D. Dissertation

by

Zhongyi Li

Department of Materials and Production, Aalborg University
Fibigerstræde 16, 9220, Aalborg, Denmark
E-mail: li@m-tech.aau.dk

Dissertation submitted August 10, 2020

Dissertation submitted: August 13, 2020

PhD supervisor: Shaoping Bai, Professor
Aalborg University

PhD Co-supervisor: Ole Madsen, Professor
Aalborg University

PhD committee: Associate Professor Johnny Jakobsen (chairman)
Aalborg University

Professor Andreas Müller
Johannes Kepler University

Associate Professor Xuping Zhang
Aarhus University

PhD Series: Faculty of Engineering and Science, Aalborg University

Department: Department of Materials and Production

ISSN (online): 2446-1636
ISBN (online): 978-87-7210-689-2

Published by:
Aalborg University Press
Kroghstræde 3
DK – 9220 Aalborg Ø
Phone: +45 99407140
aauf@forlag.aau.dk
forlag.aau.dk

Printed in Denmark by Rosendahls, 2020

Abstract

Robotic exoskeletons can provide solutions of motion assistance for human such as rehabilitation training, strength enhancement for elders, workers or soldiers. While many exoskeletons for physical assistance have been developed, most of them show limitations in achieving high performances in safety and interaction with human subjects due to their rigid actuation systems. Compliant exoskeleton which incorporates with a compliant actuation system is needed to overcome the limitation for safe and comfortable physical human-robot interaction (pHRI).

This thesis deals with compliant actuator and its use in upper-body exoskeletons. The focus is on the design, modelling and testing of compliant actuator with variable stiffness. The control methods of the actuator applicable for upper-body exoskeletons are also presented.

The thesis first introduces a novel mechanism design to realize a compliant joint with multiple stiffness behaviors. Stiffness model is developed for the mechanism to analyse the influences of design parameters. Variable stiffness can be realized, and three working modes including linear, hardening and softening modes can be observed by adjusting design parameters. A prototype is built, with which its stiffness model is validated experimentally.

The model of the novel compliant joint was extended for general cases. A unified stiffness model is developed for comprehensive stiffness analysis. The model allows designing new mechanisms for desired stiffness performances.

The dynamic modelling of the compliant joint was studied, showing that the dynamic performance varies widely with the stiffness of joint. New actuator is developed and demonstrated experimentally with a prototype in dynamic test. Dynamic characteristics of the actuator is obtained for further use in the exoskeleton control.

A control method for the compliant joint is finally investigated, which can deal with the variable stiffness of designed actuator. Both simulations and experiments are conducted to evaluate the control performance, and results reveal the effectiveness of designed actuator for exoskeleton system in improving the dynamic adaptability.

This thesis contributes the state-of-the-art of compliant actuator design.

A novel mechanism design is employed in designing new compliant actuator for desired stiffness performances. The new design in the project features the capabilities of stiffness adjustment in multiple modes, namely, hardening, softening and linear modes, which are desirable for improving performance of compliant actuator in exoskeletons.

Resumé

Exoskeletter anvendes til understøtte, forstærke eller skabe menneskelig bevægelse. De kan anvendes til en lang række formål indenfor områder såsom genoptræning, support til ældre og produktion Der er idag udviklet en lang række forskellige eksoskeletter. De fleste af disse er karakteriseret ved anvendelsen af stive strukturer, som giver begrænsninger i deres brug på grund af udfordringer med sikkerhed og brugervenlighed. For at kunne realisere sikre såvel som brugervenlige exoskeletter, der det derfor nødvendigt at udvikle fleksible og eftergivende (compliant) exoskeletter, baseret på fleksible (compliant) aktueringssystemer.

Denne afhandling omhandler fleksible aktuatorer og deres anvendelse exoskeletter for overkroppen. Fokus er på design, modellering og test af aktuatorer med variabel stivhed. Derudover behandles også styringen af aktuatorerne.

Afhandlingen introducerer først et nyt mekanismedesign til at realisere en aktuator med variabel stivhed. En stivhedsmodel for mekanismen er udviklet for at analysere effekten af forskellige designparametre. Variabel stivhed kan realiseres ved at justere designparametre. En prototype er bygget, hvormed stivhedsmodellen kan valideres eksperimentelt.

Modellen for den aktuatoren blev derefter udvidet til det generelle tilfælde. En samlet stivhedsmodel er udviklet til brug for mere omfattende stivhedsanalyser. Modellen muliggør designet af nye mekanismer baseret på ønsker om stivheden.

En model af de dynamiske egenskaber af aktuatoren blev udformet, hvilket viste det at de dynamiske egenskaber varierer meget med aktuatorens stivhed. En ny aktuator blev udviklet og testet eksperimentelt med en prototype i dynamiske test. Dynamiske egenskaber for aktuatoren identificeres for yderligere brug til styring af exoskelettet.

Slutteligt udvikles en styring for den udviklede aktuator, som kan realisere den variable stivhed. Simuleringer såvel som eksperimenter udføres for at evaluere den udviklede styring og for at undersøge effektiviteten af den udviklede aktuator.

Afhandlingen bidrager til state-of-art indenfor compliant aktuator design.

Et nyt mekanisme design er anvendt til at realisere en aktuator med de ønskede stivhedsegenskaber. Det nye design giver mulighed for at justere stivheden i flere tilstande, som er ønskelige for at kunne realisere compliant aktuatorer til exoskeletter.

Publications

Parts of PhD study work have been published in or submitted to peer-reviewed scientific journals and international conferences. Moreover, one patent has been published.

Journal Papers

1. Zhongyi Li, and Shaoping Bai. "A novel revolute joint of variable stiffness with reconfigurability." *Mechanism and Machine Theory*, 133 (2019): 720-736. doi:10.1016/j.mechmachtheory.2018.12.011

2. Zhongyi Li, Shaoping Bai, Weihai Chen, and Jianbin Zhang. "Nonlinear stiffness analysis of spring-loaded inverted slider crank mechanisms with a unified model." *Journal of Mechanisms and Robotics*, 12(3) (2020): 031011. doi:10.1115/1.4045649

3. Zhongyi Li, Shaoping Bai, Ole Madsen, Weihai Chen, and Jianbin Zhang. "Design, modeling and testing of a compact variable stiffness mechanism for exoskeletons." *Mechanism and Machine Theory*, 151 (2020): 103905. doi:10.1016/j.mechmachtheory.2020.103905

4. Zhongyi Li, Muhammad Raza Ul Islam, Weihai Chen, Jianbin Zhang, and Shaoping Bai. "Mechatronics design and testing of a novel actuator with nonlinear compliances." *IEEE/ASME Transactions on Mechatronics*, (submitted in July, 2020)

5. Shaoping Bai, Zhongyi Li, and Ruiqin Li. "Exact synthesis and input-output analysis of 1-dof planar linkages for visiting 10 poses." *Mechanism and Machine Theory*, 143 (2020): 103625. doi:10.1016/j.mechmachth-eory.2019.103625

6. Kun Wang, Zhijiang Xie, Zhongyi Li, and Shaoping Bai. "Optimum configuration design and sensitivity analysis of the 3-RRR PPMs with a general kinematic model." *Mechanics Based Design of Structures and Machines*, (2020). doi:10.1080/15397734.2020.1766490

Conference Papers

1. Zhongyi Li, Weihai Chen, and Shaoping Bai. "A novel reconfigurable revolute joint with adjustable stiffness." In *2019 IEEE International Conference on Robotics and Automation (ICRA)*, Montreal, Canada, pp. 8388-8393, May, 2019. doi:10.1109/ICRA.2019.8793906

2. Zhongyi Li, Shaoping Bai, Weihai Chen, and Jianbin Zhang. "Unified stiffness modeling and analysis of compliant crank-slider mechanisms." In *IFToMM World Congress on Mechanism and Machine Science*, Krakow, Poland, pp. 1315-1324, June, 2019. doi:10.1007/978-3-030-20131-9_129

3. Zhongyi Li, and Shaoping Bai. "Design and modelling of a compact variable stiffness mechanism for wearable elbow exoskeletons." In *2019 International Conference on Control, Mechatronics and Automation (ICCMA)*, Delft, Netherlands, pp. 342-346, November, 2019. doi: 10.1109/ICCMA46720.2019.8988697

Patent

1. Shaoping Bai, and Zhongyi Li. "A reconfigurable compliant revolute mechanism with nonlinear stiffness." IPC No.: F16D 3/ 62 A I. Patent No.: WO2020052724. March 19, 2020.

Contents

List of Figures

Preface

This thesis is submitted to the Faculty of Engineering and Science, Aalborg University (AAU), with fulfilment of the requirements for the Doctor of Philosophy. The work has been carried out during the period from February 2018 to September 2020, at the Department of Materials and Production (MP), AAU. This work is supervised by Prof. Shaoping Bai and co-supervised by Prof. Ole Madsen.

I would like to express the deepest appreciation to my supervisors Prof. Shaoping Bai and Prof. Ole Madsen. In my PhD study, Prof. Shaoping Bai gave splendid supervision and assistance, and his expertise is invaluable to my research work.

I also would like send my appreciation to Prof. Weihai Chen, who gave me help and guidance in project.

I would like to express my gratitude to my colleagues, Harun Leto, Long Teng, Muhammad Ahsan Gull, Muhammad Raza Ul Islam, Xuerong Li et al. In the past three years, we worked together and shared thoughts about research work, which are very helpful in pushing my PhD study.

Last but not least, I would like to express my gratitude to my family members. My PhD study would not have been accomplished without their help and support to my life.

Zhongyi Li
Aalborg University, August 10, 2020

Chapter 1

Background and motivation

Traditional robots are commonly working in isolated environments. Their joints are made very rigid to achieve high position accuracy. However, this leads to the fact that these robots are impossible to perform safe pHRI if using them directly to interactions with human. With the development of technology, the need of advanced robots having close collaboration and direct interaction with human has became necessity. In this regard, traditional stiff joints cannot meet this requirement. An effective solution for this problem is to introduce mechanical compliance into robotic joint, thereby realizing a compliant joint. On one hand, the compliance is able to improve the system adaptability in dealing with unstructured environments. On the other hand, it enables the energy storage capacity of joint, which helps to reduce or eliminate the damage to both actuation system and human in case of collision.

Figure. 1.1. AXO-SUIT [5].

Compliant joints were developed first for applications in humanoid robot [1, 2] and legged robots [3]. In recent years, the compliant joints have found increasing applications in robotic exoskeletons. Exoskeleton is wearable device attached to the human body to assist human motion for strength enhancement or rehabilitation training [4–12]. Fig. 1.1 shows a wearable exoskeleton, namely AXO-SUIT, which was developed at Aalborg University [5]. For such a system, the human safety is of the highest priority. Use of compliant joints in exoskeleton system will be helpful in achieving a safe and comfortable pHRI, as well as a good torque control. A large number of compliant joints have been developed, and some of them have been employed in exoskeleton systems. Some noticeable devices such as MINDWALKER [13], HARMONY [14], NEUROExos [15] and LOPES [16] et al. have been tested and evaluated in laboratories, showing advantages of compliant joints in improving pHRI safety and comfort. However, designing such compliant joint for exoskeleton applications is still a tough task, and the following factors potentially bring challenges to the development of compliant joint for upper-body exoskeletons.

- *Size and weight*: The compliant joint should be designed very compact in the fact that the size and weight of an exoskeleton are very limited. A light-weight compliant joint is desirable to reduce the inertia of exoskeleton links which is considered as a dominant factor to the system bandwidth. Most of adjustable compliance joints use at least two actuation units, usually one for joint stiffness and the other for position. By this way, it is possible to regulate the joint stiffness online [17, 18], and to adapt the compliance to different tasks automatically. However, two-motor setup highly increase the size and weight of the compliant joint, which are not desirable for the wearable exoskeleton applications. Moreover, to be able to adjust stiffness, these joints are usually designed much more complex than a traditional rigid actuator.

- *Stiffness range*: A broad stiffness range is beneficial to increase exoskeleton adaptability to task change. For example, a high stiffness setting may be desirable for robot-in-charge task, where the human body is drove to follow the exoskeleton motion, while a soft setting make the exoskeleton compliant to human motion, which is needed for human-in-charge task. The exoskeleton for the task in this work, i.e. physical assistance, needs to be worked in the mode of human-in-charge. Therefore, the exoskeleton can achieve a completely soft setting is preferable.

- *Stiffness behavior*: A linear behavior makes it easy to model the system dynamics. However, a nonlinear behavior is more flexible in changing its stiffness curve than a linear one. Some compliant joints with nonlinear behaviors might be beneficial to improve pHRI safety, system

stability and energy efficiency [19–22]. However, most of them only have fixed stiffness behaviors. In other words, they cannot adjust stiffness performance achieving multiple behaviors. Thus, new compliant joint design that has ability to change stiffness behavior is desirable for improvement of system performance.

- *Potential energy*: The potential energy stored in the compliant joint is determined by the used elastic element, which can be formulated as

$$U = \int \tau(\theta, k_s)\, d\theta \tag{1.1}$$

where θ is joint deflection, k_s is the stiffness of elastic element, and τ is joint torque which is a function of θ and k_s. A compliant joint allowing to conveniently change elastic element of different stiffness will make it flexible for different tasks. Moreover, as can been from Eq. (1.1), the potential energy is closely related to joint torque and deflection. For any given potential energy capacity, the maximum torque and deflection of compliant joint can be changed through modifying the torque function $\tau(\theta, k_s)$. For example, to enlarge the maximum joint torque and deflection, a method is to modify the joint to exhibit hardening behavior which has low torque/stiffness for small deflection and high torque/stiffness for large deflection [19]. This has implication in the necessity of designing a compliant joint with multiple stiffness behaviors.

- *Torque resolution and bandwidth*: For compliant joints with fixed compliance or with constant stiffness behaviors, a common problem is the tradeoff between torque resolution and bandwidth. A soft setting of the compliant joint results in a high torque resolution but a low bandwidth, while a stiff setting achieves an increased bandwidth but reduces torque resolution. To overcome this limitation, some research efforts have been made. A solution is to optimize the stiffness for compliant joint with nonlinear stiffness behavior [22, 23]. In a very recent work [22], Zhao et al. have proposed a method using the perceptivity and responsiveness index (PRI) to achieve optimal stiffness behaviors enabling increased torque resolution and bandwidth. However, the optimal stiffness behavior varies with application change. For practical reasons, it is still a difficult work to achieve such a variable stiffness mechanism with desired behavior.

In the light of the above challenges, novel design principles and implementation methods of compliant joints are needed to enhance their performance of physical HRI. Therefore, the initial objective of this thesis is to investigate a novel compliant joint design which is applicable for upper-body exoskeletons to improve physical HRI.

This thesis consists of eight chapters.

Chapter 1-3 presents the background and motivation, and gives a through review of the compliant joints including their mechanical designs and control methods. Based on the review studies, objectives of this thesis are given.

Chapter 4-7 are the representative articles corresponding to the thesis subjects, which is described as follows:

- **Chapter 4** proposes a novel design of joint mechanism to realize compliant joint with multiple stiffness behaviors.
- **Chapter 5** extends the work from **Chapter 4** by investigating a unified stiffness model of the compliant joint. Based on the unified model, mechanism design method for desired stiffness performances is also studied in this chapter.
- **Chapter 6** focuses on the dynamic modelling of the compliant joint.
- **Chapter 7** presents mechatronics design and control method of the compliant joint.

Chapter 8 concludes the work in this thesis, with a summary from the results of the Ph.D. project and contributions. Future works are also suggested for further investigations.

Chapter 2

Review of compliant joints

This chapter gives an overview of the compliant joint. The mechanical designs of the compliant joints were explored at first. Implementation of nonlinear stiffness systems were reviewed. The control methods for the compliant joint are investigated finally.

2.1 Compliant joints

In this thesis, a compliant robot joint is defined as the joint with mechanical compliance, which allows deviations from its equilibrium position when the external torque/force exerted on the joint [24]. According to stiffness characteristics, compliant joints can be classified into two main categories [25], i.e. the joints of fixed compliance and the joints of adjustable compliance, are used to classify the compliant joints, as shown in Fig. 2.1. In this section, the state-of-the-art of compliant joints in each category will be presented to give an overall review of the compliant joint, and their applications in wearable exoskeletons will also be introduced.

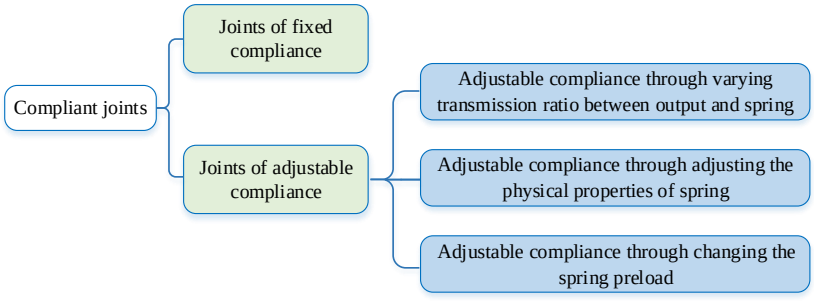

Figure. 2.1. Classification of compliant joints.

2.1.1 Joints of fixed compliance

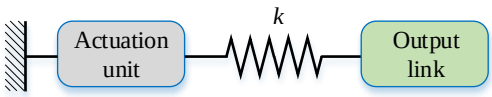

Figure. 2.2. Basic configuration of the fixed compliance type joint.

In this category, the Series Elastic Actuator (SEA) is the most well-known example, and it is also considered as the first attempts towards the implementation of active compliant joints. In 1995, Pratt and Williamson first presented the concept of SEA. In their work [1], the SEA is realized by integrating a spring between the actuator output and the motor gearbox. The introduced elasticity from spring reduces the mechanical impedance of the system, thus help to improve the adaptability of the actuator in dealing with unstructured environments. Moreover, the spring isolates the motor gearbox from load, which brings benefits in protecting drivetrain from external shocks. Afterwards, many SEAs have been developed for robotic applications including assistive exoskeletons, rehabilitation robots and legged robots. The basic configuration of SEA is shown in Fig. 2.2. The spring in SEA can be used as a force sensor and a force generator in consideration of the spring force-elongation relationship. The spring constant builds a linear relationship between the force applied by the actuation unit and the compression of the spring, which is expressed as

$$k = \frac{F}{x} \tag{2.1}$$

where F is the force delivered by the actuation unit, x is the spring compression, and k is the spring constant.

SEA, as a new actuation technology, has advanced in recent years. In [14], Kim et al. proposed a SEA which has been used in an upper-body rehabilitation exoskeleton, namely Harmony, as shown in Fig. 2.3 (a). In Harmony system, the SEA used can provide low impedance and precise torque control, which are essential in robot-aided therapeutic exercises. Yu et al. [26] proposed a SEA which is used in a lower-body exoskeleton, as shown in Fig. 2.3 (b). This actuator has similar mechanical structure to the one proposed by Pratt and Williamson [1], but it is of more compact size. In [27], Yu et al. has further verified the feasibility of the actuator in human-robot interaction control. In [28], Kong et al. developed an orthosis robot for lower-limb rehabilitation training, in which rotary SEAs were used, as shown in Fig. 2.3 (c). The rotary SEA can generate ideal torque for the control in human gait rehabilitation training. In [29], another SEA for knee orthosis was also proposed by Kong et al. Compared with the SEA presented in [28], the new one used

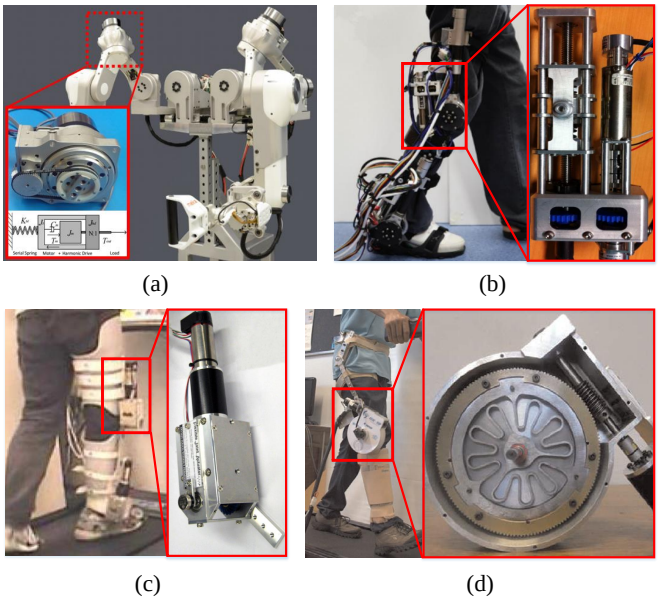

Figure. 2.3. (a) Harmony [14], (b) knee-ankle-foot robot integrated with SEAs [26, 27], (c) lower-limb orthosis actuated by RSEA [28], and (d) active knee orthosis integrated with a rotary SEA [30].

a torsional spring with a lower stiffness to achieve a lower impedance and a higher torque resolution for the actuator. As shown in Fig. 2.3 (d), a custom-designed spring was presented and used in an active knee orthosis to achieve an accurate torque sensing capability [30]. In [31], a SEA proposed by Kim et al. was used for a lower extremity exoskeleton to generate accurate interaction forces between robot and user during walking. The above mentioned compliant actuators were used for exoskeleton applications, and some other applications can be found in legged robots. For example, Curran and Orin used a SEA in an articulated leg to improve its jump performance [32]. Another noticeable example can be found in [33], in which serial elasticity was introduced in a legged robot to enhance its power modulation. Verstraten et al. have made a systematic investigation on the influence of the serial elasticity on the power and energy consumption [34]. Studies show that due to the fixed compliance, the energy efficiency can only be improved when the joint motion frequency matches the system natural frequency.

The fixed compliance type joints have been used to various applications, especially in the field where human friendly environment is needed. However, since the fixed compliance, this type of joint commonly has a very limited force/torque resolution and bandwidth [24, 35, 36]. For example, a joint with high compliance is sensitive to small force/torque, but results in a low

bandwidth of system. A low compliance has advantage in increasing the bandwidth, but reduces the torque resolution. These limitations highly reduce the adaptability of the fixed compliance type joint to application variability and change.

2.1.2 Joints of adjustable compliance

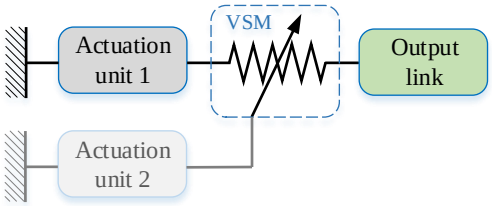

Figure. 2.4. Basic configuration of adjustable compliance type joints.

Another category is the joints with adjustable compliance. Their applications can be found in exoskeletons [37, 38], legged locomotion robots [39–41] and robotic prosthetics [49, 50]. A typical configuration of the adjustable compliance type joints is shown in Fig. 2.4. As can be seen from this figure, two actuation units are usually used in the joint, one for joint position and the other for joint stiffness.

The joint can achieve adjustable stiffness through integrating a variable stiffness mechanism (VSM) between the actuation unit and the output. The VSM can be implemented by taking advantage of the following three methods [25]: varying transmission ratio, adjusting the physical properties of a spring, and changing the preload. In this section, we will investigate the development of the adjustable compliance type joints based on the stiffness variation methods.

Varying transmission ratio between output and spring

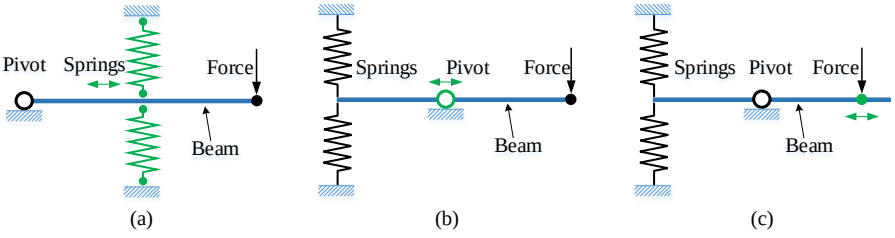

Figure. 2.5. Three configurations of lever mechanism.

Changing the transmission ratio between output and spring is an effective way to vary stiffness, thus it has been widely adopted in the designs of compliant joint. The lever mechanisms shown in Fig. 2.5 are commonly used to realize the change of the transmission ratio. A lever mechanism consists of a beam, spring and three principal points (the pivot, the spring attachment and force points). The effective lever arm between the pivot point and the spring point can be adjusted by altering the position of any of the three points. For example, as shown in Fig. 2.5 (a), the pivot and force points are kept fixed, and the spring attachment point can be moved along the beam to change the effective length of lever arm, thereby enabling transmission ratio change. The joint stiffness of the lever mechanism can be expressed as [42]

$$K = 2k_s l \tag{2.2}$$

where K is the equivalent stiffness of the lever mechanism, k_s is spring stiffness, and l is the effective length of lever arm.

In recent years, numerous compliant joints based on lever mechanism have been developed. Among of them, AwAS [42], AwAS-II [43], CompAct-VSA [44], vsaUT [45] and vsaUT-II [46] are very noticeable.

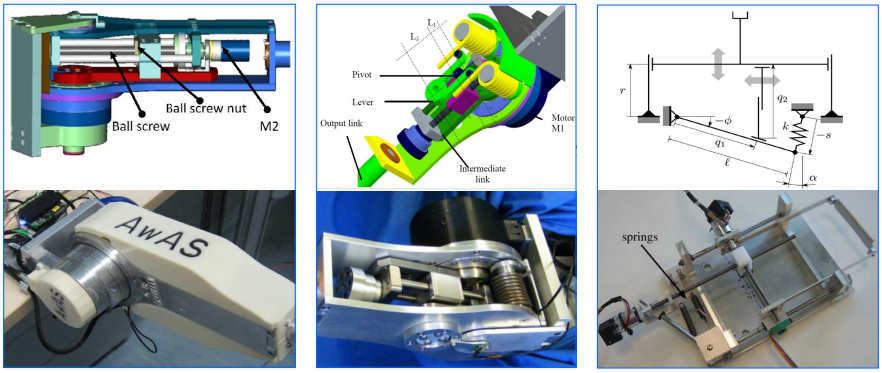

(a) (b) (c)

Figure. 2.6. (a) AwAS [42], (b) AwAS-II [43], and (c) vsaUT [45].

Fig. 2.6 (a) shows the design of AwAS, which was reported by Jafari et al [43]. AwAS was designed with the lever mechanism shown in Fig. 2.5 (a), in which the stiffness adjustment is achieved through altering the spring position. In the prototype of AwAS, two motors were used, one for regulating joint position, and the other motor (M2) attached to a ball screw is used to vary the spring position for stiffness adjustment, as shown in Fig. 2.6 (a).

Jafari et al. also proposed another compliant actuator, namely AwAS-II, as shown in Fig. 2.6 (b). This actuator can be considered as the evolution of

AwAS. AwAS-II was designed with the lever mechanism shown in Fig. 2.5 (b), in which the position of pivot point is moved along the beam. The joint stiffness of AwAS-II is zero when the pivot and spring attachment points coincide, and the joint can achieve infinity stiffness when the pivot point reaches to the force point. As the very high stiffness range does not depend on the length of lever, AwAS-II was designed to be more compact than AwAS. Due to the very large stiffness adjustment range of the lever mechanism shown in Fig. 2.5 (b), this mechanism is also used in other compliant joints, such as CompAct-VSA [44] and vsaUT-II [46].

Fig. 2.6 (c) shows the design of vsaUT presented by Visser et al. [45]. Variable stiffness of vsaUT is achieved through changing the position of force point in lever mechanism. A main property of vsaUT is that its stiffness can be regulated without changing the potential energy of spring, which enhances the energy efficiency of system. However, vsaUT has a very complex structure, which bring limitations in robotic applications.

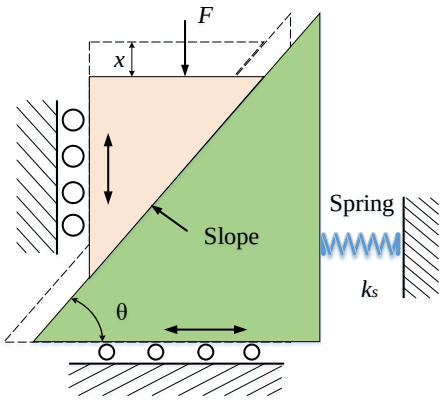

Figure. 2.7. Variable stiffness achieved by changing transmission angle θ.

The mechanism shown in Fig. 2.7 is also able to achieve variable stiffness, which is done by changing the transmission angle. In this mechanism, an external force F can be balanced by spring force, and cause a displacement x. The stiffness along the force direction can be formulated as [39]

$$k_{eq} = \frac{k_s}{(\tan\theta)^2} \tag{2.3}$$

where k_{eq} is equivalent stiffness, k_s is spring stiffness, and θ is slope angle, i.e. transmission angle. We can see from Eq. (2.3), the equivalent stiffness is a function of θ. In other words, the stiffness can be adjusted by changing the transmission angle. Based on this stiffness adjustment method, Vu et al. have developed a compliant actuator, namely MESTRAN, for legged robot [47,

48]. In MESTRAN, two motors were used, enabling independent control of position and stiffness. Moreover, MESTRAN is capable of regulating stiffness with a high speed and a very large range. In [39], Vu et al. further verified that the actuator with proper stiffness is able to improve the hopping energy efficiency of the legged robot at a particular hopping frequency.

For the compliant joint based on varying transmission ratio, its main advantage is that the potential energy in the springs is not reduced by adjusting the joint stiffness, which means no energy is need to tune the stiffness. Thus, this type of joint is suitable for legged robots where high energy efficiency is needed. Moreover, the joint is able to achieve a very wide stiffness range, which bring benefits in improvement of system adaptability. However, this type of joint is very complex, which brings limitations to use them in lightweight and portable devices, such as wearable exoskeletons.

Adjusting the physical properties of spring

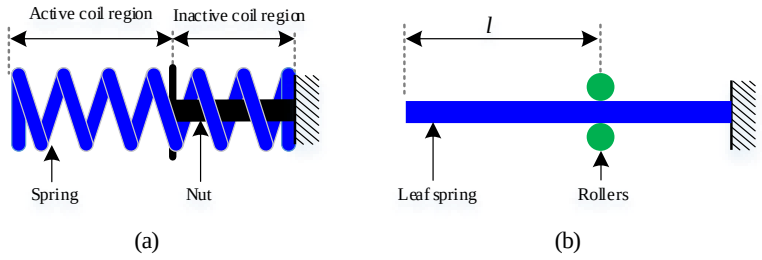

Figure. 2.8. (a) Jack spring and (b) leaf spring.

Stiffness variation can be achieved by changing the physical properties of a linear spring. To understand this method, the elasticity of the spring is considered herein, which is

$$k_s = \frac{Gd^4}{8 \times D^3 n} \tag{2.4}$$

where G is shear modulus, d is spring wire diameter, D is spring coil diameter, and n is the number of active coils of spring. Eq. (2.5) implies that the stiffness can be adjusted through changing any of four parameters G, d, D or n. In reality, the simplest way is to adjust the active coils' number, n. Fig. 2.8 (a) shows the design of Jack spring mechanism which was proposed by Hollander et al. [49, 50]. Jack spring mechanism can be treated as a helical spring which is able to change its number of active coils through rotating the nut as shown in Fig. 2.8 (a).

Stiffness variation can also be achieved by changing the physical properties of a leaf spring. For a leaf spring, its elasticity can be expressed as [51]

$$k_s = \frac{EA}{l} \tag{2.5}$$

where l is the effective length of leaf spring, E is the material modulus, and A is the cross-sectional area of leaf spring. According to Eq. (2.5), stiffness adjustment can be achieved by changing the design parameters of leaf spring. Fig. 2.8 (b) shows a method to change the effective length l. We can see from Fig. 2.8 (b), the effective length l can be easily changed through moving the roller. The leaf spring with variable effective length have been adopted in some compliant joints. Fig. 2.9 shows some design examples of compliant joint using leaf spring. Among of them, MeRIA was successfully used in a lower limb exoskeleton for motion assistance or rehabilitation training [54], as shown in Fig. 2.9 (c).

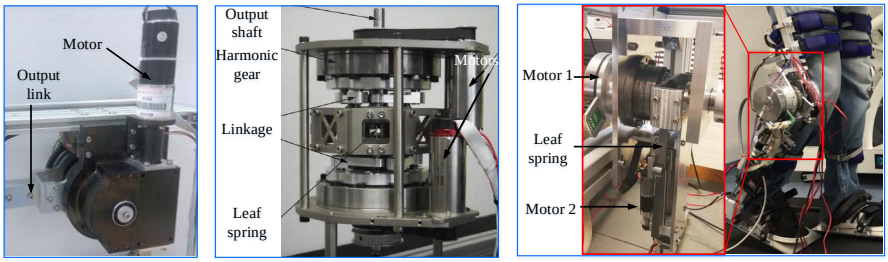

Figure. 2.9. (a) Leaf spring-based VSA [52], (b) VSJ [53], and (c) MeRIA [54].

An advantage of compliant joints using either Jack spring or leaf spring is that they are easy to construct due to their simple structure and easy to control since the stiffness and position variation are totally independent [25]. However, compliant joints using Jack spring or leaf spring have a lower energy storage capacity than the ones using the transmission ratio variation or spring preload methods respective to the weight and size [55].

Changing the spring preload

Compared with methods of variation of transmission ratio or adjusting the physical properties, changing the spring preload is the easiest way to tune the stiffness setting, which has been received increasing interests in recent years. This method can be employed in combination with an antagonistic or independent motor setup, as shown in Fig. 2.10.

In the joint with antagonistic motor setup, two motors and two nonlinear springs are arranged in a bidirectional antagonistic configuration. The joint position can be controlled through rotating the motors in the same direction,

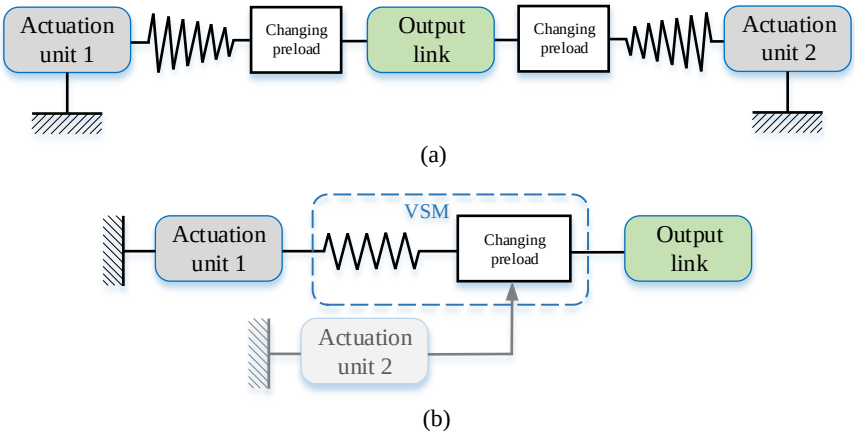

Figure. 2.10. Compliant actuators with (a) antagonistic motor setup and (b) independent motor setup.

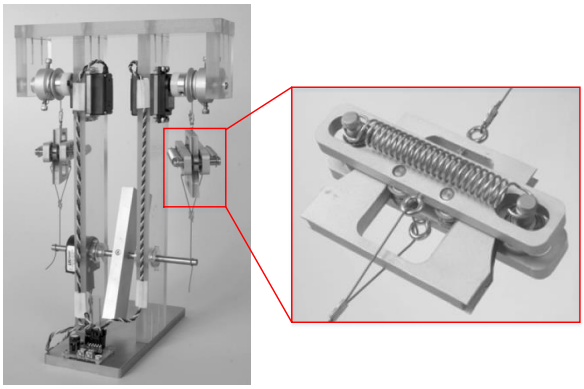

Figure. 2.11. Biological inspired joint and nonlinear spring device proposed by Migliore et al. [56].

while the joint stiffness is adjusted by changing the spring preload through a counter-rotation of motors.

The antagonistic type joints have been studied extensively, and they are used mainly in biological systems, because antagonistic actuations are common in biology. Fig. 2.11 shows a biological inspired joint with a basic antagonistic setup, presented by Migilore [56]. The stiffness variation of joint can be achieved by changing the preloads of two nonlinear spring devices. Noting that, for an antagonistic type joints, the spring needs to be nonlinear to obtain the adaptable stiffness of the joint. Other noticeable joints in this type can be found in [15, 55, 57]. Some of them have been used in exoskeletons. NEUROexos is one of the most well-known example, which was designed by Vitiello [15]. The elbow joint of NEUROexost was actuated by hydraulic pistons through Bowden cables. As such, the actuation system can be mounted away from the exoskeleton joint. In [57], an upper limb exoskeleton, namely One-DOF PEHA was presented, in which two pneumatic artificial muscles were used to actuate the exoskeleton joint through generating antagonistic contraction forces. Bowden cables were also used in One-DOF PEHA to transmit contraction forces to the joint. The actuation system can thus be located apart from the joint, which makes it easy to achieve a compact and low-weight joint design. However, using two actuation units to actuate single joint makes the system bulky and heavy. Moreover, the spring used in the systems with antagonistic setup needs to be nonlinear to enable the joint positioning and stiffness variation simultaneously.

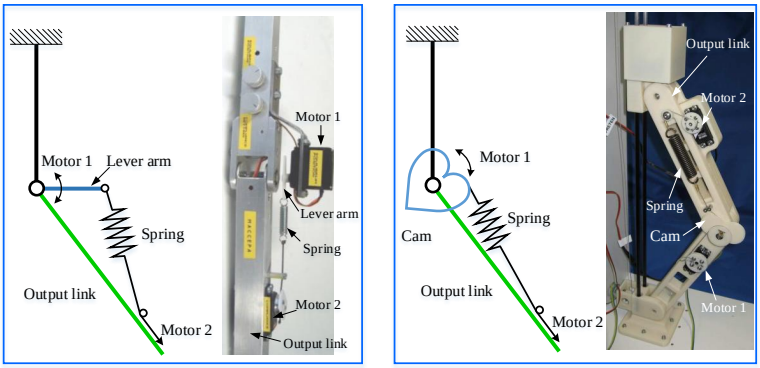

Figure. 2.12. (a) MACCEPA [3] and (b) MACCEPA 2.0 [58].

Many compliant joints have also been designed with independent motor setup, in which some examples such as MACCEPA [3], MACCEPA 2.0 [58], VS-joint [59], FSJ [60], SJM I [61] and SJM II [62] et al. are very noticeable. Fig. 2.12 (a) shows the design of MACCEPA proposed by Van Ham et al. [3].

In MACCEPA, two motors are used, one for controlling lever arm position, and the other for controlling spring preload. Noting that a linear spring is used, but MACCEPA exhibits nonlinear stiffness performance due to the nonlinearity from the geometry of MACCEPA. Van Ham et al. also proposed an evolution version of MACCEPA, namely MACCEPA 2.0, as shown in Fig. 2.12 (b). In the new version, a profiled cam replaced the lever arm in MACCEPA, hence a desired stiffness behavior can be obtained by shaping the cam profile. MACCEPA has a very simple structure allowing it to fit in the wearable exoskeleton applications. Some examples based on MACCEPA concept are shown in Fig. 2.13. Other spring preload based actuators can be found in [68–72].

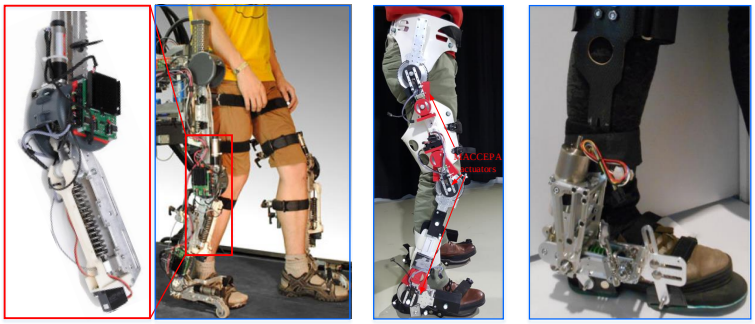

Figure. 2.13. (a) Lower limb exoskeleton proposed by Grosu et al. [63], (b) MIRAD sit-to-stand exoskeleton developed by Vantilt et al. [64], and (c) active ankle foot orthosis developed by Moltedo et al. [65–67].

2.2 Nonlinear stiffness systems

A nonlinear stiffness system has a nonlinear relationship between force/torque and displacement/deflection. Compared with the compliant joint with constant stiffness, the joint with nonlinear stiffness is more flexible in shaping its behavior to match different requirements in applications. Some compliant joints which can produce nonlinear stiffness behaviors have been developed. They are desired in enhancing pHRI safety, increasing energy efficiency or improving system bandwidth and torque resolution [19, 20, 78]. Nonlinear behaviors in compliant joints can be generally divided into two categories: hardening and softening behaviors. Stiffness hardening means an increase in the stiffness with increasing of joint deflection, while softening is the opposite, i.e. a reduction in the joint stiffness [73]. Fig. 2.14 shows the torque-deflection relationships with hardening and softening behaviors.

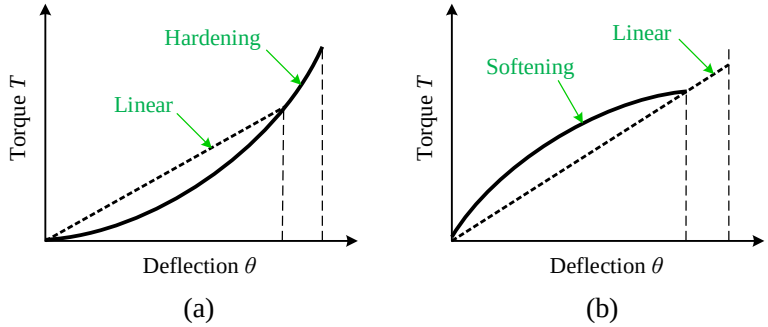

Figure. 2.14. Torque-deflection relationships with (a) hardening behavior and (b) softening behavior.

In [20], a compliant joint with hardening stiffness behavior was developed by Austin et al. The hardening behavior allows this joint to achieve a good compromise in terms of obtaining both high bandwidth and high torque resolution. In [55], Wolf et al. suggested to modify the torque function as a hardening behavior to enlarge the torque and deflection ranges of the compliant joint with the same elastic energy, as shown in Fig. 2.14 (a). In [74, 75], two springs, i.e. one with low stiffness and the other with high stiffness, were used in one robotic joint to achieve both high force fidelity and bandwidth. When a low torque is applied on the joint, the spring with low stiffness is compressed, and the joint stiffness is thus low. With the increase of applied torque, the low stiffness spring is fully compressed becoming inactive, then the spring with high stiffness is active, thus the system has a high stiffness. In [76–78], a compliant joint with softening stiffness behavior was presented by Park et al. The softening stiffness behavior can guarantee that the joint maintains high position accuracy for a low external force and has high collision safety for a large external force. In [22], Zhao et al. focused on the optimization of nonlinear stiffness behavior. In their work, a stiffness optimization method was used to achieve both high torque resolution and high bandwidth for a compliant joint. In [79], a predefined stiffness profile can be obtained by adopting a custom-designed cam and linear spring. Different stiffness behaviors can be obtained by redesigning the cam shape. However, the geometry of the cam is needed to be changed, which is not convenient for the adjustment of stiffness behavior.

Nonlinear stiffness is also usually found in antagonistic joints, as introduced in Section 2.1.2. With a pair nonlinear springs, the antagonistic joint is possible to control both position and stiffness, and its working principle is very close to the mammalian joint which is commonly actuated by several muscles and tendons that are arranged in an antagonistic way. The spring or

mechanisms shown in Fig. 2.15 can be used in an antagonistic joint. A first option is to use progressive spring shown in Fig. 2.15 (a), in which the coils are spaced differently or with different spring coil diameters. Cam-spring mechanism shown in Fig. 2.15 (b) is also used to produce nonlinear behavior. In this mechanism, the stiffness characteristic can be shaped by designing the cam shape. Nonlinear stiffness behavior can also be generated by a four-bar mechanism, as shown in Fig. 2.15 (c). Based on the nonlinear relationship between input and output angles of the four-bar mechanism, a spring with constant stiffness can be stretched in a nonlinear way. By appropriate selection of design parameters, the mechanism can be designed to realize desired stiffness behaviors.

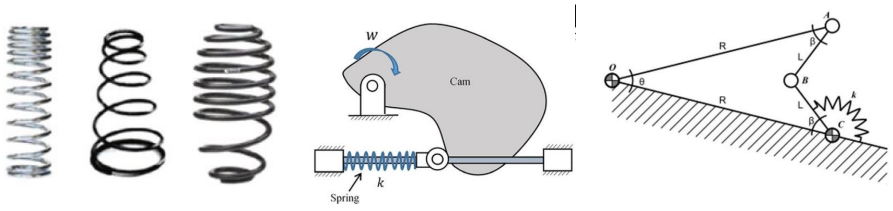

Figure. 2.15. Springs or mechanisms achieving nonlinear stiffness include (a) progressive springs, (b) cam-spring mechanism, and (c) spring-loaded four-bar mechanism.

2.3 Actuation and control of compliant joints

The actuation unit is the power source for the compliant joint. The electric motor shown in Fig. 2.16 (a) is used in the majority of compliant joints because it can generate desired force/torque with high speed and good controllability. As introduced in Section 2.1, RSEA [28], AwAS [42], vsaUT-II [46] and MACCEPA [3] et al. are the noticeable examples of using electric motor as the power source.

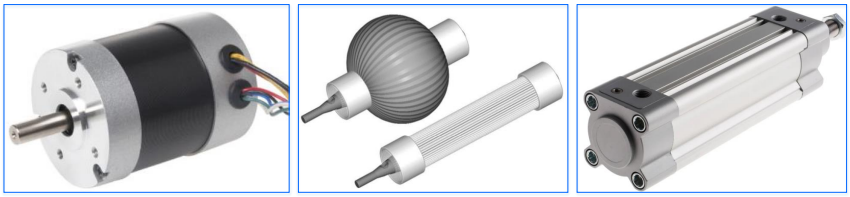

Figure. 2.16. (a) Electric motor, (b) pneumatic artificial muscle, and (c) hydraulic actuator.

Except for electric motor, pneumatic artificial muscle (PAM) shown in

Fig. 2.16 (b) is often used in compliant joints. PAM is operated by gas pressure to generate contractile motion, which makes PAM inherently compliant. McKibben muscle proposed by Chou et al. [80] is one of the most famous design. The compact shape of McKibben muscle makes it easy to be employed in robotic devices. The plated PAM (PPAM) proposed by Verrelst et al. [81] is also noticeable, which has been used in a biped robot. PAM usually has a high power-to-weight ratio and its inherent compliance brings benefit in improving safety of physical HRI in exoskeletons. However, a compliant joint should be actuated by two or more PAMs, which usually results in a complex actuation system. Moreover, compared with electric motor, PAM has a lower accuracy in motion control due to its high hysteresis.

Few compliant joints are powered by hydraulic actuators as shown in Fig. 2.16 (c). NEUROExos [15] is the most well-known example. In NEUROExos, a hydraulic system which is mounted on a fixed support actuates the elbow joint of exoskeleton through Bowden cables. The hydraulic actuator can provide higher force/torque with good precision. However, a hydraulic system is usually bulky, which brings limitation in the application of wearable exoskeleton.

In applications of compliant joints such as exoskeletons, their motion control is essentially a problem of force/torque control. Considering that the high controllability of electric motor in generating desired torque, we use electric motor as the power source in the compliant joint in this Ph.D. project. Many control methods have been presented to control such compliant joints to generate desired force/torque, in which PID, PD and PI controllers were commonly used. Pratt and Williamson proposed a SEA [1] which was used for Cog humanoid robot project [2]. In this SEA, an electric motor was used and treated as a desired torque source. PI current control was performed to let the SEA produce desired force. In [82], Robinson et al. developed a SEA with linear motion for a biomimetic walking robot. In this SEA, a DC motor is connected to a ball-screw to drive the linear motion. A linear spring was used to isolate the ball-screw nut from external load. With such configuration, the load applied on the SEA can be acquired through measuring the spring compression with a potentiometer. PD force controller was performed to realize feedback force control of the SEA. The control scheme of the above two mentioned cases is shown in Fig. 2.17 (a). In the control scheme, the motor is treated as desired torque source. Backlash and friction effects from the motor and drivetrain should be good quantified to improve the torque/force control performance [82, 83].

Robinson suggested to treat the motor in compliant joint as a velocity source rather than as a force/torque source [83]. The improved control scheme is shown in Fig. 2.17 (b). In [86], Wyeth proved that treating the electric motor as velocity source could be helpful in dealing with undesirable effects from the motor and drivetrain, and the performance of SEA can be

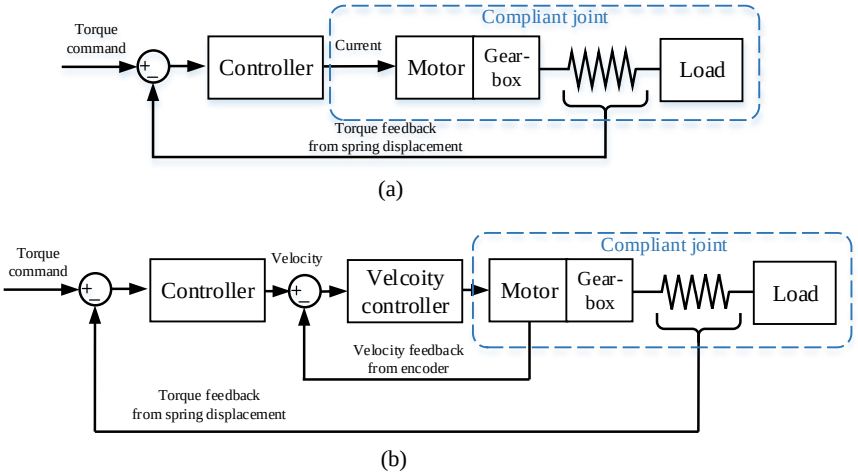

Figure. 2.17. Control methods of compliant joints with the motors treated as (a) torque source and (b) velocity source.

greatly improved. In [85], Vallery et al. presented a control scheme for SEA, in which the output torque of the SEA was tracked through a PID controller which outputs the desired motor velocity, and cascaded PI controllers were performed to control the motor to track the desired velocity. Both simulation and experiment have been made to verify the effectiveness of this control scheme. Based on PID, PD or PI torque control of compliant joints, some methods including H_∞ and gain-scheduled methods have been used to further improve the controller stability [30, 87]. In [28, 88], disturbance observers were used to compensate the modeling errors.

Above all mentioned compliant joints have fixed compliance. In other words, these compliant joints themselves are unable to control the system impedance. Therefore, the fixed compliance type joints need to be combined with compliant control, e.g. impedance control to realize impedance variation. In [84], Sergi et al. presented a cascaded control scheme, in which a PI torque controller was used in the inner loop, while a PD impedance controller was performed in the outer loop to facilitate the impedance adjustment. In [30], impedance control was also used to regulate the impedance of an active knee orthosis for human walking assistance. However, due to the fixed compliance of the above joints, they have a very limited control bandwidth, which is determined by the mechanical impedance. Joint with adjustable compliance can overcome this limitation through regulate the joint stiffness online or offline. The control methods for fixed compliance type joints are also applicable for adjustable compliance type joints, but an additional position control for the motor regulating the stiffness online is needed.

2.4 Summary

Among of the stiffness adjustment methods, changing the spring preload is considered as the simplest way to achieve stiffness variation [55], because only few simple mechanical components are used in the construction of compliant joint. Based on this method, a large number of compliant joints have been developed, and their applications are commonly found in lower-limb exoskeletons. To achieve a compact compliant joint for upper-body exoskeleton applications, spring preload method is adopted in this work. However, for a compliant joint based on spring preload, the stiffness range is usually very small. Therefore, for such compliant joint, a new design to extend the stiffness range is needed to increase its adaptability.

Regarding nonlinear stiffness systems, the performance of the compliant joint for exoskeletons may benefit from adjustable compliance and multiple stiffness behaviors. However, only few existing devices [20, 59, 79] are able to adjust stiffness in multiple behaviors. Most of them are based on redesigning cam shape, which is not convenient for adjusting stiffness performance. Therefore, it is needed to propose a new compliant joint which is able to adjust stiffness performance conveniently and to achieve desired stiffness behaviors. Noting that the nonlinear behavior also brings difficulty to analyse the stiffness performance. Thus, an essential work in this thesis is to develop a generalized or unified stiffness model which facilitates the stiffness analysis.

Chapter 3

Objectives and work scopes

The main objective of this thesis is to investigate new principles of compliant joint design and implementation. The new concept of compliant joint design is derived from a basic mechanism, as shown in Fig. 3.1.

This mechanism can be considered as a special case of four-bar linkage which has a zero-length ground link and a compliant coupler [73]. For a four-bar rigid-body linkage shown in Fig. 3.1 (a), the speed ratio between the crank and the follower, a.k.a. mechanical advantage, is the function of link lengths and rotation angle, so is the torque ratio. In a special case (see Fig. 3.1 (b)) when the length of the ground link is zero, the torque ratio, or the reciprocal of the speed ratio, becomes a constant of 1. The linkage becomes singular when the three links are collinear. If we replace the coupler with elastic element, a new mechanism can be obtained, and its stiffness at this singularity is determined by the spring preload and the geometry of the mechanism. According to [73], the joint stiffness is formulated as

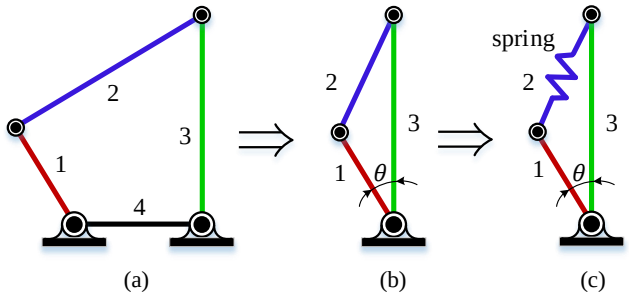

Figure. 3.1. Concept of designing a compliant joint by using a zero-length base link four-bar linkage.

$$k_{eq} = k\left(J^2 + \frac{\partial J}{\partial \theta}\delta l_2\right) + F_0\frac{\partial J}{\partial \theta} \tag{3.1}$$

with

$$J = \frac{l_1 l_3 \sin\theta}{\sqrt{l_1^2 + l_3^2 - 2l_1 l_3 \cos\theta}} \tag{3.2}$$

$$\frac{\partial J}{\partial \theta} = \frac{l_1 l_3 \cos\theta}{l_2} - \frac{l_1^2 l_3^2 \sin^2\theta}{l_2^3} \tag{3.3}$$

where l_1, l_2 and l_3 are the lengths of bar-1, 2 and 3, and θ is joint deflection, k is spring stiffness, and F_0 is spring preload. As can be seen from Eq. (3.1) that the joint stiffness k_{eq} is associated with joint mechanism dimensions, rotation angle, and also pretension as well. Thus, a joint mechanism of variable stiffness can be achieved.

Compliant joint mechanism shown in Fig. 3.1 will be the focus of this thesis. The following objectives will be achieved:

- Design a new compliant joint which is able to adjust stiffness in multiple modes.
- Establish stiffness and dynamic model to investigate the performance of the compliant joint.
- Develop a control method for the compliant joint to achieve safe pHRI.
- Experimentally study the feasibility of the compliant joint for upper-body exoskeleton.

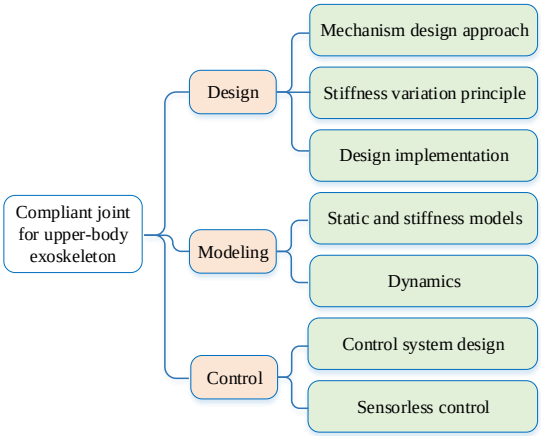

Figure. 3.2. Work scope in this Ph.D. project.

To achieve the above objectives, the research works in this thesis are defined, as shown in Fig. 3.2. The scope covers the design, modeling and control of a novel compliant joint, which is closely in connection with the forthcoming four chapters. The design approach, stiffness variation principle and implementation of the compliant joint are studied in **Chapter 4**. Static and stiffness models are built and analyzed in both **Chapters 4** and **5**. The dynamics are investigated in **Chapters 6**, and the control of the compliant joint is implemented in **Chapters 7**.

Chapter 4

Paper I

A novel revolute joint of variable stiffness with reconfigurability

Zhongyi Li, and Shaoping Bai

The paper has been published in the
Mechanism and Machine Theory Vol. 133(2019), pp. 720–736, 2019.

Mechanism and Machine Theory 133 (2019) 720–736

Contents lists available at ScienceDirect

Mechanism and Machine Theory

journal homepage: www.elsevier.com/locate/mechmachtheory

Research paper

A novel revolute joint of variable stiffness with reconfigurability

Zhongyi Li, Shaoping Bai*

Department of Materials and Production, Aalborg University, Aalborg 9220, Denmark

ARTICLE INFO

Article history:
Received 17 September 2018
Revised 25 November 2018
Accepted 10 December 2018
Available online 21 December 2018

Keywords:
Variable stiffness mechanism
Reconfigurable mechanism
Multi-mode stiffness variation
Exoskeletons

ABSTRACT

In this paper, a novel revolute joint of variable stiffness with reconfigurability (JVSR) is presented. The JVSR is designed with a compliant joint mechanism, and is able to vary widely its stiffness in multiple modes, namely, linear, hardening and softening modes. This brings the joint for many potential applications in novel transmission and robotics. In the paper, mathematical models of joint stiffness are developed for the JVSR, with which influences of design parameters are analyzed. A prototype of JVSR is constructed and preliminary test results validate the model. A design case is included to illustrate the application of the JVSR in exoskeletons.

1. Introduction

Robotic joints with inherent compliance can find applications in rehabilitation robots [1–5], wearable exoskeletons [6–9], legged robots [10–12] and service robots [13–15]. In general, the compliant joints are used for increasing safe physical human-robot interaction (pHRI) or improving the dynamical adaptability with environment, as well as enhancing the energy efficiency. Up to date, many compliant joints exhibiting different stiffness performance have been proposed. They can be classified into two types: the joints of fixed compliance and the adjustable compliance joints [1].

The fixed compliance type joints usually utilize linear springs in series with stiff actuators. The series elastic actuator (SEA) is the most famous example in this type. A rotary SEA presented in [7] was designed to actuate an orthosis. A helical torsion spring with constant stiffness is installed between a DC motor and a human joint to enhance pHRI safety. The device was used as a torque generator as well as a torque sensor in robotic systems, thus a desired control performance was achieved. Another fixed compliance joint with a customized torsion spring is presented in [6]. Safe human-robot interaction and torque estimation were achieved by integrating the joint into a knee orthosis. In [11,16,17], energy efficiency with fixed compliance joint was investigated. The study shows that, due to the constant stiffness, the energy efficiency of the robotic device is generally low and can only be improved when the trajectory behavior of robotic joint matches the natural frequency of the system. Moreover, SEA using linear spring experiences another limitation that the design needs to tradeoff between system bandwidth and torque resolution [18,19]. As an alternative, fixed compliance joints with nonlinear behaviors have been developed in recent years, considering that nonlinear behavior offers more design parameters than a linear one and more flexible in shaping stiffness/torque-deflection profiles. In [19], a nonlinear SEA with hardening stiffness behavior

* Corresponding author.
E-mail addresses: shb@mp.aau.dk, shb@m-tech.aau.dk (S. Bai).

https://doi.org/10.1016/j.mechmachtheory.2018.12.011
0094-114X/

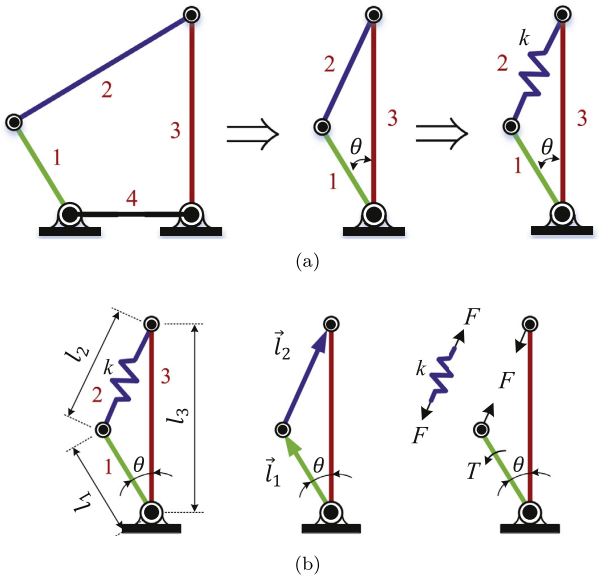

Fig. 1. (a) The concept of constructing a compliant joint by utilizing a special case of four-bar linkage. (b) Kinematic and static diagram of the mechanism.

was proposed to overcome the limitation of the design tradeoff, which can maintain a higher torque resolution at low deflection and a larger response bandwidth for high deflection. In [20], Park et al. designed a joint mechanism with softening stiffness behavior which can maintain high stiffness for a low external force, but reduce stiffness for a large external load, hence guaranteeing both position accuracy and collision safety.

Contrary to the fixed compliance type joint, the adjustable compliance joints are able to change their stiffness dynamically. They can be designed with different principles, such as spring preload based principle [3,12,21–23], transmission ratio based principle [24–29], and special springs [30,31]. Ham et al. [12] proposed the MACCEPA where stiffness variation is achieved by adjusting the preload of a spring. The VS-joint [23] is another design based on spring preload principle where a cam disk of a specific shape is used to change the preload. Other adjustable compliance devices, such as AwAS [26,27], MeRIA [28], MESTRAN [29], VSJ [30], VSA-CubeBot [32] and CompactAct-VSA [33] are noticeable too. However, in most cases of adjustable compliant joints a secondary motor is usually used to actively tune an elastic element to achieve stiffness variation. As a consequence, the adaptable compliance joint is heavy and complex.

It is noticed that the existing designs, both fixed compliance and adjustable compliance joints, show limitations in achieving nonlinear stiffness behavior. Only a few devices [19,23,34–36] are able to adjust stiffness performance achieving multiple behaviors. In the design in [34], a hypocycloid mechanism was used to stretch a spring with linear stiffness in a nonlinear way. The mechanism can achieve approximate linear and hardening behaviors, excluding softening behavior. In [19,23,35,36], different behaviors were achieved by redesigning cam shape, with which design parameters of the mechanism need to be adjusted. Some studies show that nonlinear stiffness behavior is helpful in improving energy efficiency [18], collision safety [20] and stability [37]. Thus new designs that are able to adjust stiffness behavior are desirable for improving compliant joint performance.

In this paper, a novel revolute joint of variable stiffness with reconfigurability is proposed. The new design attempts to achieve a variable stiffness with multiple modes and to ease the adjustment of stiffness. The idea of the compliant joint mechanism design is shown in Fig. 1. Through the adjustment of the design preload, the variable stiffness can be achieved, and three working modes showing hardening, softening and linear behaviors can be realized. Moreover, a reconfigurable design based on the mechanism is proposed to effectively facilitate the adjustment of its stiffness and output-torque ranges. The proposed mechanism is novel in its capacities of reconfiguration and variable stiffness adjustment together with a compact architecture.

The paper is organized as follows: Section 2 describes basic concept of stiffness variation based on a compliant joint mechanism and conducts the associated stiffness analysis. The design of JVSR is presented in Section 3, followed by the stiffness modeling. In Section 4, a prototype of JVSR and its test-rig are constructed, with which experiments are carried out to validate the ability of stiffness adjustment of JVSR. In Section 5, a case study is described in which the proposed mechanism is scaled for joints of an upper-body exoskeleton. Section 6 concludes this work.

2. Basic concept of stiffness variation

2.1. Kinematic principle

The JVSR can be treated as a special case of the four bar linkage. For a four-bar rigid-body linkage, the speed ratio between the crank and the follower, a.k.a. mechanical advantage, is the function of link lengths and rotation angle, so is the torque ratio. In a special case when the length of the ground link is zero, the torque ratio, or the reciprocal of the speed ratio, becomes a constant of 1. The linkage becomes singular when the three links are collinear. If we replace one rigid link with elastic element, the stiffness at the singular configuration is zero.

Fig. 1 shows the kinematic principle of the new design of joint with variable stiffness. By replacing the coupler, bar-2, with compliant material (e.g. spring, rubber, or thin metal strips) of stiffness k, a compliant joint mechanism is obtained.

2.2. Stiffness model

To facilitate the modeling, we assume that the bar-1 is the input link, while bar-3 is the output link. The angle between the output and the input links is denoted by θ. Furthermore, the input and the output links (bar-1 and 3) are considered as rigid and articulated with the base by pin joints. Let the lengths of bar-1, 2 and 3 be l_1, l_2 and l_3 respectively, which satisfy the constraint

$$l_2^2 = l_1^2 + l_3^2 - 2l_1 l_3 \cos\theta. \tag{1}$$

Moreover, let F and T be the tension along bar-2 and the external equilibrium torque applied on the joint, respectively, then

$$T = F \cdot \left| \hat{l}_2 \times \vec{l}_1 \right| = J \cdot F, \tag{2}$$

where $\hat{l}_2$ is the unit vector of $\vec{l}_2$, and $J = \left| \hat{l}_2 \times \vec{l}_1 \right| = \frac{\partial l_2}{\partial \theta} \in \Re^1$ is the linkage Jacobian, which is a scalar for the mechanism.

The equivalent rotational stiffness of output link, $K_{eq} \in \Re^1$, represents a linear relationship between the infinitesimal torque δT and the infinitesimal deflection $\delta\theta$, which is described by:

$$\delta T = K_{eq} \cdot \delta\theta. \tag{3}$$

Combining Eq. (3) together with Eq. (2), and given that $\delta F = k \cdot \delta l_2$, K_{eq} can be obtained as:

$$K_{eq} = \frac{\delta T}{\delta\theta} = J \cdot \frac{\delta F}{\delta\theta} + \frac{\delta J}{\delta\theta} \cdot F. \tag{4}$$

That is,

$$K_{eq} = J \cdot k \cdot J + \frac{\delta J}{\delta\theta} \cdot F = J^2 k + \frac{\delta J}{\delta\theta} \cdot F. \tag{5}$$

The stiffness K_{eq} in Eq. (5) is composed of two terms, $J^2 k$ and $\frac{\delta J}{\delta\theta} \cdot F$, which are contributed by the stiffness of compliant coupler k and the internal tension F respectively. According to Hooke's law, the internal tension F is given by

$$F = k \cdot (l_2 - l_{2,0}) + k \cdot (l_{2,0} - l_{2,r}) = k \cdot \delta l_2 + F_0, \tag{6}$$

where $l_{2,0}$ represents the length of bar-2 when $\theta = 0$, and $l_{2,r}$ is the free length of elastic element, and F_0 is the pretension of elastic element for $\theta = 0$.

Substituting Eq. (6) into Eq. (5) and rearranging it, we get the equivalent stiffness K_{eq} associated with the initial tension F_0

$$K_{eq} = \underbrace{J^2 k + \frac{\delta J}{\delta\theta} \cdot k \cdot \delta l_2}_{K_{eq,1}} + \underbrace{\frac{\delta J}{\delta\theta} \cdot F_0}_{K_{eq,2}}, \tag{7}$$

where $K_{eq,1}$ and $K_{eq,2}$ are the stiffness induced by the stiffness of compliant coupler k and the pretension F_0 respectively.

We introduce a length ratio $\lambda = l_1/l_3$, $(\lambda \in (0, 1))$ and substituting it into Eq. (7) gives

$$K_{eq} = k l_3^2 \hat{K}_{eq,1}(\lambda, \theta) + F_0 l_3 \hat{K}_{eq,2}(\lambda, \theta), \tag{8}$$

where

$$\hat{K}_{eq,1}(\lambda, \theta) = \frac{K_{eq,1}}{k \cdot l_3^2} = \hat{J}^2 + \frac{\delta \hat{J}}{\delta\theta} \cdot \delta \hat{l}_2, \tag{9}$$

$$\hat{K}_{eq,2}(\lambda, \theta) = \frac{K_{eq,2}}{F_0 \cdot l_3} = \frac{\delta \hat{J}}{\delta\theta}, \tag{10}$$

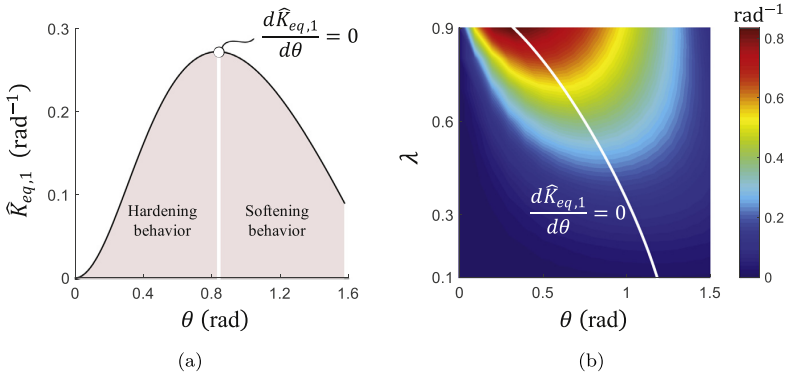

Fig. 2. Stiffness performance of $\hat{K}_{eq,1}$. (a) Stiffness $\hat{K}_{eq,1}$ as a function of the deflection angle θ with $\lambda = 0.5$. (b) Influence of $\lambda = l_1/l_3$ on $\hat{K}_{eq,1}$.

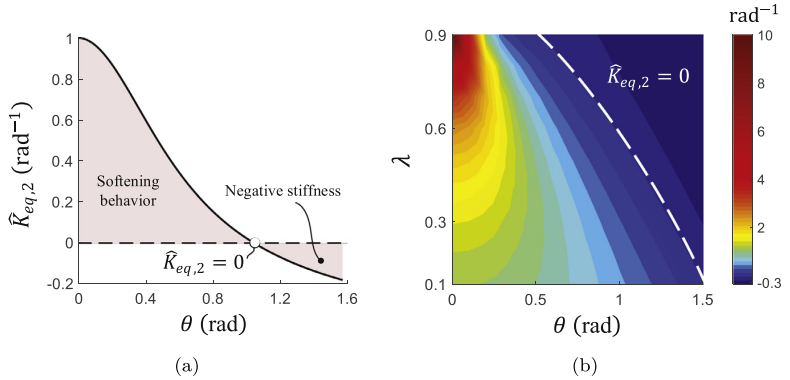

Fig. 3. Stiffness performance of $\hat{K}_{eq,2}$. (a) Stiffness $\hat{K}_{eq,2}$ as a function of the deflection angle θ with $\lambda = 0.5$. (b) Influence of $\lambda = l_1/l_3$ on $\hat{K}_{eq,2}$.

with $\hat{J} = \lambda \sin\theta/\hat{l}_2$ and $\hat{l}_2 = \sqrt{\lambda^2 - 2\lambda\cos\theta + 1}$. Note that $\hat{K}_{eq,1}$ and $\hat{K}_{eq,2}$ in Eqs. (9) and (10) are related only to the parameters of λ and θ. In other words, they are factors that are influenced only by mechanism geometry. We herein investigate the properties of $\hat{K}_{eq,1}$ and $\hat{K}_{eq,2}$, and look at the influences on the stiffness performance.

As $\hat{K}_{eq,1}$ and $\hat{K}_{eq,2}$ change with respect to the joint deflection θ and the design parameter λ, we look into the influence of each parameter. Fig. 2 shows the change of $\hat{K}_{eq,1}$ with respect to θ, and the influence of λ. As can be seen from Fig. 2(a), the stiffness curve in the range $[0, \pi/2]$rad can be divided into two intervals, separated at the deflection angle $\theta\,|_{d\hat{K}_{eq,1}/d\theta=0}$. The separation line divides the entire curve into two intervals of different behaviors, namely, hardening behavior and softening behavior. Joint stiffness hardening means an increase in the equivalent stiffness, while softening is the opposite, i.e., a reduction in the equivalent stiffness.

Two special points in Fig. 2(a) should be noted. One is $\theta = 0$ where the configuration stands for a singular point, thus the joint shows zero stiffness. The other is $\theta = \theta\,|_{d\hat{K}_{eq,1}/d\theta=0}$ which is described as the position where the rate of the torque increase of $Jk\cdot\delta l_2$ is maximum as θ increases within $[0, \pi/2]$rad. Through adjusting the ratio $\lambda = l_1/l_3$, different stiffness performances can be achieved as shown in Fig. 2(b). In this figure, the white line of $d\hat{K}_{eq,1}/d\theta = 0$ represents all maximum $\hat{K}_{eq,1}$ for any given ratio λ. We can also see that a larger λ will yield a smaller range of intervals for hardening behavior but a larger maximum value of $\hat{K}_{eq,1}$.

Fig. 3 shows the change of stiffness $\hat{K}_{eq,2}$ in the range $[0, \pi/2]$rad. As can be seen in Fig. 3(a), the $\hat{K}_{eq,2}$ monotonically decreases as θ increases. Moreover, it shows a softening behavior first. After $\hat{K}_{eq,2}$ reaches zero at $\theta = \theta\,|_{\delta\hat{J}/\delta\theta=0}$, it shows a negative stiffness. Referring to Eq. (2), the special point, $\theta\,|_{\delta\hat{J}/\delta\theta=0}$, stands for the position where $\vec{l}_1$ and $\vec{l}_2$ are vertical. Fig. 3(b) shows the influence of the ratio $\lambda = l_1/l_3$ on $\hat{K}_{eq,2}$. We can see that a larger λ will yield a smaller range of intervals for softening behavior but a larger value of $\hat{K}_{eq,2}$ at $\theta = 0$.

Eq. (8) indicates that F_0 affects the overall stiffness by scaling $\hat{K}_{eq,2}$ which can be observed from Fig. 4 showing the changes of K_{eq}. In Fig. 4, the solid line $\frac{dK_{eq}}{d\theta} = 0$ and dash line $K_{eq} = 0$ separate the whole region into three parts. They

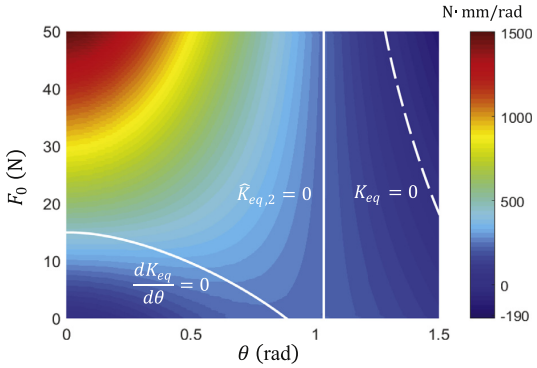

Fig. 4. The distribution of the equivalent stiffness K_{eq} for varying deflection angle θ and the initial tension F_0 with $\lambda = 0.5$, $k = 1$ N/mm and $l_3 = 30$ mm.

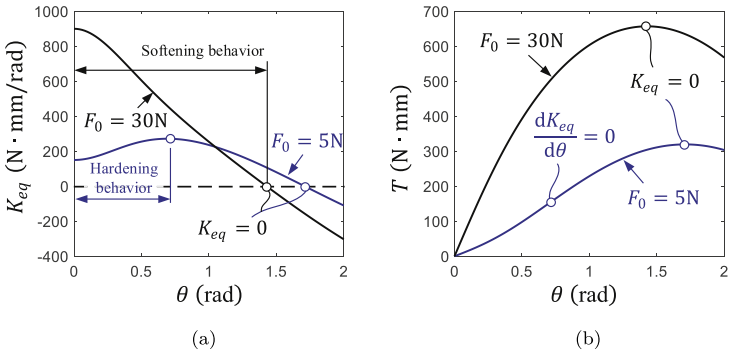

Fig. 5. (a) Stiffness curves and (b) the corresponding torque curves for different pretensions, in which other parameters are assigned as $\lambda = 0.5$, $k = 1$ N/mm and $l_3 = 30$ mm.

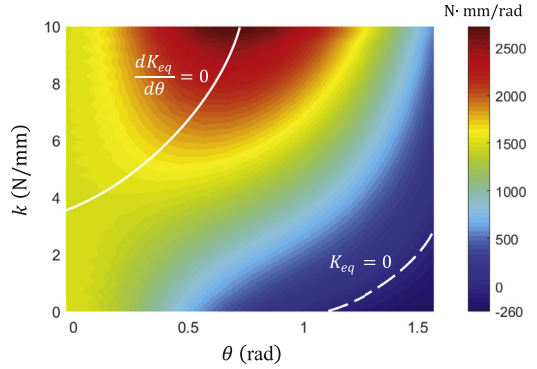

Fig. 6. The variation of the equivalent stiffness K_{eq} for varying deflection angle θ and the stiffness k with $F_0 = 50$ N, $\lambda = 0.5$ and $l_3 = 30$ mm.

correspond to the hardening behavior area (in the lower-left corner), the softening behavior area and the negative stiffness area (in the higher-right corner). Moreover, recalling that $\hat{K}_{eq,1}$ at singular point ($\theta = 0$) is zero, the joint stiffness is therefore solely determined by $K_{eq,2}$. In Fig. 4, the stiffness variation at point of $\theta = 0$ for changing F_0 can be observed clearly.

Fig. 5 shows two cases with $F_0 = 5$N and $F_0 = 30$ N to illustrate further the influence of F_0. The stiffness and torque curves are displayed in Fig. 5(a) and 5(b). In Fig. 5(a), both hardening and softening behaviors can be observed from the curves, showing the influence of pretension F_0 on stiffness performance of the mechanism.

Eq. (8) also indicates that the stiffness k influences the stiffness performance by scaling $\hat{K}_{eq,2}$. Fig. 6 shows the change of stiffness with respect to θ and k.

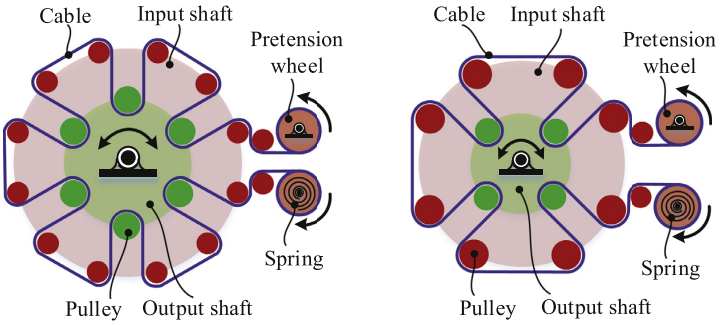

(a) $n = 6$ (b) $n = 4$

Fig. 7. Schematic design of JVSR, (a) an example design with $n = 6$, (b) another example design with $n = 4$.

It is noted that the negative stiffness mentioned represents a decreasing equilibrium torque when deflection is increased. Taking the case for $F_0 = 30\,\text{N}$ in Fig. 5 as an example, the compliant joint mechanism shows negative stiffness when the deflection angle exceeds $\theta = 1.45\,\text{rad}$. At this point, the torque due to the spring force reaches the maximum and then starts to reduce when the deflection angle increases. The calculated equivalent stiffness thus becomes negative.

3. Development of JVSR

3.1. Design of JVSR

Based on the aforementioned variation stiffness principle, a reconfigurable compliant revolute joint mechanism is proposed as shown in Fig. 7. In this mechanism, the compliant joint mechanism is implemented as a cable wrapped on three pins (pulleys), one in the output link and the other two in the input link. The mechanism design is reconfigurable by wrapping the cable around different number of pins. In the design, the number of pins on the input shaft are two times of the number of pins in the output shaft. Herein, we use the number of pins on the output link, n, to describe the reconfigured design. Fig. 7(a) and 7(b) show two reconfigurations, $n = 6$ and $n = 4$. In the mechanism, two coaxial shafts, input shaft and output shaft, are coupled through the cable. One end of the cable is reeled, while the other end of the cable is connected to a linear spring of stiffness k with pretension F_0.

With the new design, reconfiguration is feasible not only by changing the number of pins, but also by pattern of wrapping. Fig. 8 illustrates the reconfiguration of JVSR with $n = 6$. It can be seen that six configurations can be implemented by different cable wrapping. In this light, we use one more number N ($N \leq n$) to indicate the number of branches, namely, the number of pins on the output shaft that are wrapped by cables.

3.2. Stiffness modeling of JVSR

For the sake of simplicity, the following assumptions are made for the modeling:

- The spring is the only compliant element in the system, cable and structure elements being considered rigid.
- The system is frictionless.

It should be noted that although the cable is considered as rigid, due to the stretch of the cable, the actual linear spring is replaced by an equivalent stiffness to compensate for it, as in Eq. (21).

The schematic of a single branch of JVSR is shown in Fig. 9, which is slightly different to the compliant joint mechanism in Fig. 1 due to the real construction. All major geometrical parameters, except λ, l_3 and θ illustrated in the four-bar linkage model, have been labeled in Fig. 9 and defined as follows:

- R_1, R_2 and R_3 are the radii of pulley-1, 2 and 3 respectively, and are identical ($R_1 = R_2 = R_3 = R$).
- b is the diameter of cable.
- a is the distance between the axes of the pulley-2 and 3, which is given by

$$a = 2R_1 + R_2 + R_3 + 2b \approx 4R. \tag{11}$$

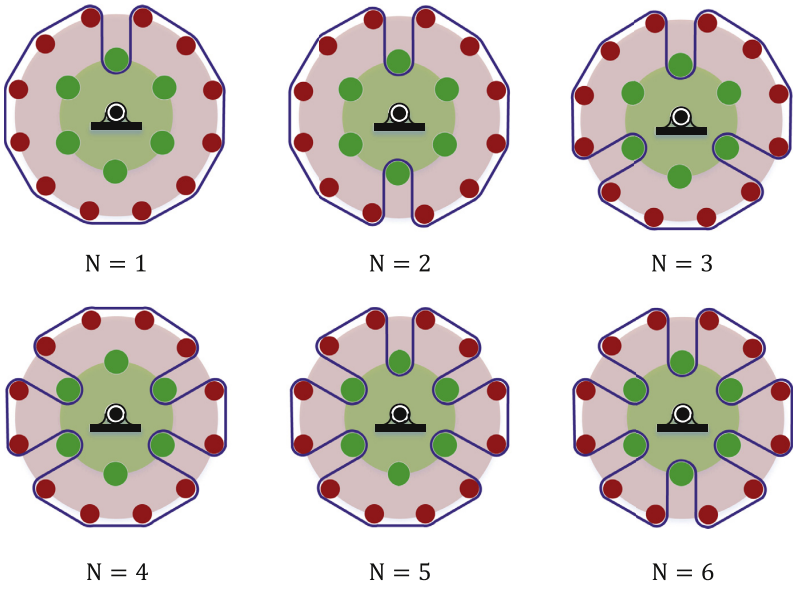

Fig. 8. Reconfiguration of JVSR ($n = 6$) indicated by the number of pins wrapped.

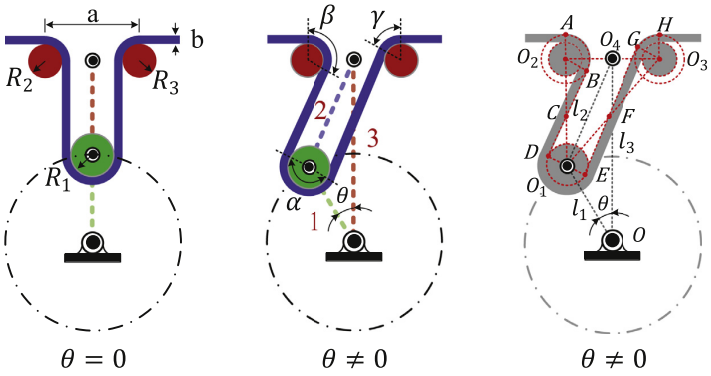

Fig. 9. The schematic of a single branch of JVSR.

- α, β and γ are the contact angles between cable and pulley-1, 2, 3 respectively, which can also be expressed as

$$\begin{cases} \alpha = \beta + \gamma \\ \beta = \arccos\left(\frac{a-2l_1\sin\theta}{\sqrt{4l_2^2-4al_1\sin\theta+a^2}}\right) - \arccos\left(\frac{a}{\sqrt{4l_2^2-4al_1\sin\theta+a^2}}\right) + \frac{\pi}{2} \\ \gamma = \arccos\left(\frac{a+2l_1\sin\theta}{\sqrt{4l_2^2+4al_1\sin\theta+a^2}}\right) - \arccos\left(\frac{a}{\sqrt{4l_2^2+4al_1\sin\theta+a^2}}\right) + \frac{\pi}{2}. \end{cases} \tag{12}$$

In Fig. 9, the cable length is calculated as

$$l = \frac{a\cdot\alpha}{2} + \left|\overrightarrow{DB}\right| + \left|\overrightarrow{EG}\right|, \tag{13}$$

where $\left|\overrightarrow{DB}\right| = \sqrt{l_2^2 - al_1\sin\theta}$, $\left|\overrightarrow{EG}\right| = \sqrt{l_2^2 + al_1\sin\theta}$.

In order to distinguish from the symbols used in Section 2, we use J_1, K, K_1 and K_2 to represent the Jacobian, the equivalent stiffness of the joint, the induced stiffness $K_{eq,1}$ and $K_{eq,2}$ respectively.

Based on the derivation of Eq. (2), the Jacobian is obtained by differentiating Eq. (13), which is given by

$$J_1 = \frac{\partial l}{\partial\theta}. \tag{14}$$

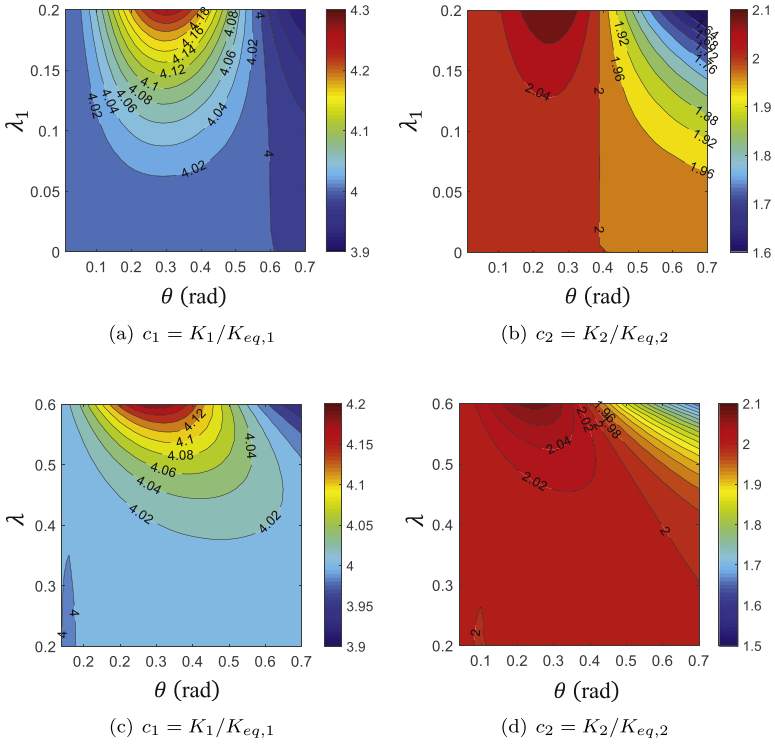

Fig. 10. Contour plots of c_1 and c_2 as a function of λ (λ_1) and θ, (a) c_1 with $\lambda = 0.6$, (b) c_2 with $\lambda = 0.6$, (c) c_1 with $\lambda_1 = 0.18$, (d) c_2 with $\lambda_1 = 0.18$.

The torque model of Eq. (2) and the stiffness model of Eq. (7) are rewritten as

$$T = J_1 \cdot F, \tag{15}$$

$$K = \underbrace{J_1 \cdot k \cdot J_1 + \frac{\delta J_1}{\delta \theta} \cdot k \cdot \delta l}_{K_1} + \underbrace{\frac{\delta J_1}{\delta \theta} \cdot F_0}_{K_2}. \tag{16}$$

The detailed expression of K is not included for clarity. So far, we have obtained the equivalent stiffness model of mechanism in Fig. 9. We define a ratio of $\lambda_1 = R/l_3$, which satisfies

$$0 < \lambda_1 < \lambda < \sqrt{1 + 4\lambda_1^2} - 2\lambda_1. \tag{17}$$

Furthermore, we define $c_1 = K_1/K_{eq,1}$ and $c_2 = K_2/K_{eq,2}$ which describe the changes due to the geometry of mechanical parts, compared to the simplified model, and Eq. (16) can be rewritten as

$$K = c_1 l_3^2 k \hat{K}_{eq,1}(\lambda, \theta) + c_2 l_3 F_0 \hat{K}_{eq,2}(\lambda, \theta). \tag{18}$$

Fig. 10 shows the variations of c_1 and c_2 with respect to the changes of θ, λ and λ_1. The figure shows that when λ and λ_1 are small, the two coefficients, c_1 and c_2, are nearly unchanged even though the deflection angle θ increases.

If N branches are utilized in JVSR, the total stiffness of the joint becomes

$$K = N^2 c_1 l_3^2 k \cdot \hat{K}_{eq,1} + N c_2 l_3 F_0 \cdot \hat{K}_{eq,2}, \tag{19}$$

and the torque model of the JVSR becomes

$$T = N^2 k \delta l J_1 + N F_0 J_1. \tag{20}$$

This is the complete model of the JVSR, which can achieve multi-mode stiffness variation by reconfiguration and parameter adjustment. The overall working principle of stiffness variation is shown in Fig. 11.

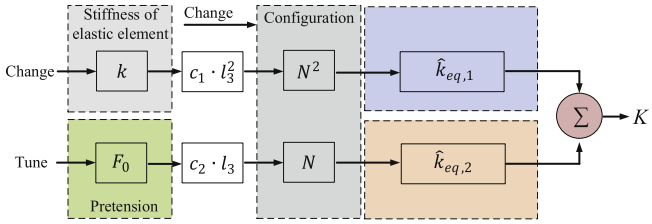

Fig. 11. The overall working principle of stiffness variation.

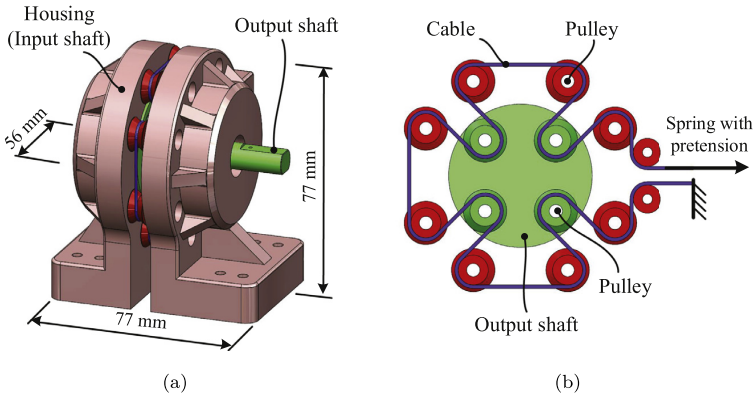

Fig. 12. JVSR design for experimental test. (a) CAD Model of the JVSR prototype. (b) Design of cable arrangement.

Table 1
Parameters for the JVSR prototype.

Parameters	Values
Dimensions (length × width × height)	77 × 56 × 77 mm
Weight	0.268 kg
n	4
Ratio λ	0.6
Ratio λ_1	0.18
Length of bar-3, l_3	25 mm

4. Prototyping and testing

In this section, a prototype of JVSR along with its test rig setup is described. Experimental results with the prototype are presented, analyzed and compared with the results from analytical simulation.

4.1. Prototype of JVSR

The prototype model of JVSR is shown in Fig. 12. The design is in accordance with the model described in Fig. 7(b). A total of four configurations can be obtained. In the testing, the input shaft is fixed to the housing of JVSR (see Fig. 12(a)) and cannot rotate in the experiments. Thus, there is only one equilibrium position, $\theta = 0$, in this prototype. In the future design, the input shaft can be connected to a position motor, thereby, the equilibrium position and stiffness can be independently controlled. Fig. 12(b) shows the details of cable arrangement in the prototype. A nylon cable of 1 mm diameter is used in our JVSR prototype, which is able to sustain for a maximum tension of about 50N. Linear spring is connected to one end of the nylon cable. The other end of the nylon cable is fixed on the housing.

The JVSR prototype is able to work in both softening and hardening modes for the controllable tension limit of cable. Table 1 summarizes the main design parameters of JVSR prototype. To evaluate the influence of k on the stiffness performance of JVSR, two springs, spring 1 of $k_{s,1} = 0.6613$N/mm and spring 2 of $k_{s,2} = 0.214$ N/mm, were used. Simulation of stiffness variation for different pretensions and configurations of spring 1 is shown in Fig. 13. From this figure, all three modes of spring stiffness varying, namely, hardening, softening and linear modes can be observed. The solid lines in Fig. 13(a) and 13(b) differentiate hardening and softening modes. Within areas bounded by the dash lines the JVSR prototype approximately exhibits constant stiffness, which can be considered as a linear spring. From Fig. 13, we also see that the

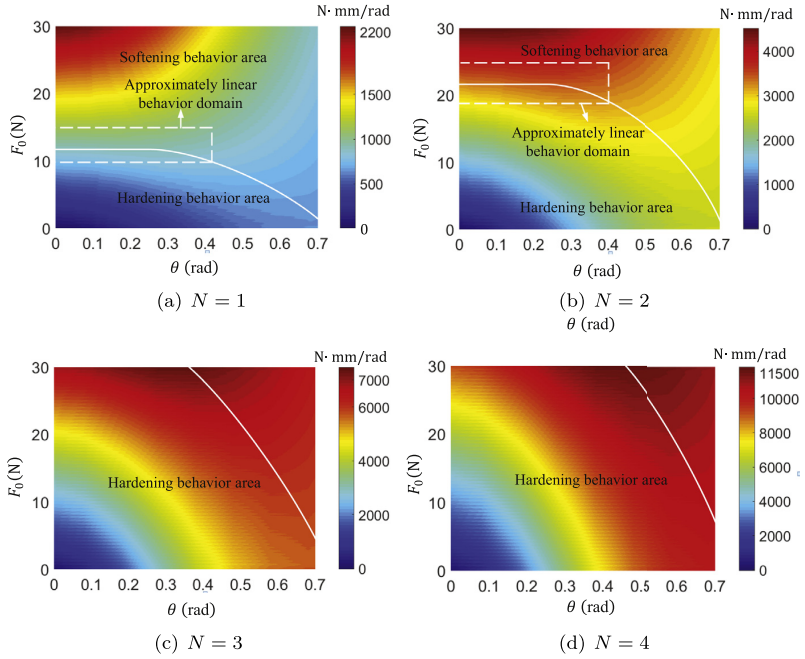

Fig. 13. Simulation of JVSR prototype stiffness v.s. cable pretension F_0 and rotation deflection of output shaft θ for different configurations, (a) $N = 1$, (b) $N = 2$, (c) $N = 3$, (d) $N = 4$.

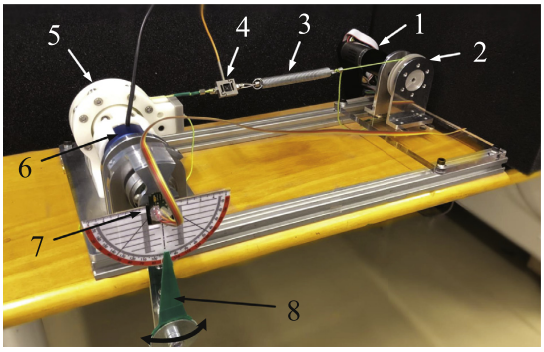

Fig. 14. JVSR test rig constructed with (1) motor-gearbox, (2) winch, (3) linear spring, (4) load cell, (5) JVSR, (6) torque sensor, (7) encoder, (8) pendulum.

area of hardening mode becomes larger with the increase of N, which is also in accordance with the expression of Eq. (19). Moreover, a larger stiffness adjustment range under the same angle deflection θ can be obtained with the increase of N.

4.2. Test rig and experiment setup

The testing setup is depicted in Fig. 14. A nylon cable is routed around a winch, which is used to adjust the cable tension in the experiments. A motor with gearbox which is installed along the winch provides an alternative to control the cable pretension automatically in this test rig. Standard linear spring is connected along the nylon cable. A load cell (model: Forsentek FS01−10 kg) is mounted between the winch and spring, and this instrument ensures a measure of force with an accuracy of 0.1N. A torque sensor (model: Forsentek FTE−20 NM) is installed along the output shaft of JVSR to measure the applied torque on the shaft with an accuracy of 0.04N·m. For the convenience of applying torque on the shaft, a pendulum is designed, and is connected to the torque sensor through the shaft. An absolute encoder (model: RLS RMB20) is used to measure the rotation angle θ of the pendulum with an accuracy of 0.5°. The sensory data is acquired with an Arduino DUE board, which is also used for motor control by working together with the ESCON motor driver.

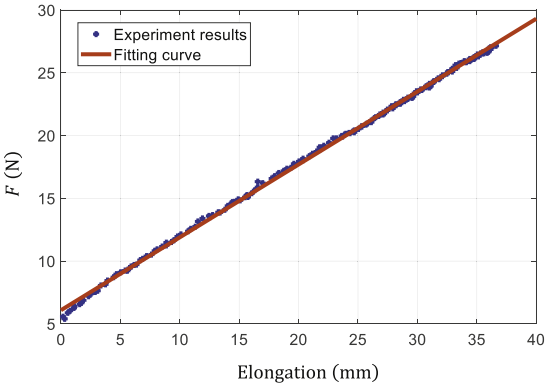

Fig. 15. The force-vs-elongation curves of the nylon cable, wherein the dots denote experiment results, and the solid line denotes the fitting curve.

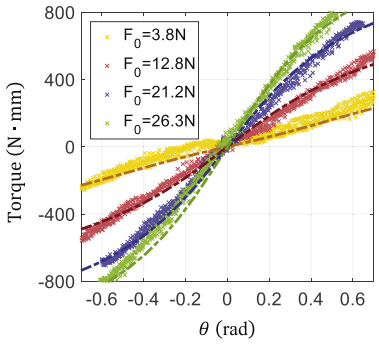

Fig. 16. Plot of torque versus deflection θ for varying pretension F_0 with $N = 1$. All dots denote experiment results, and the dash-dot lines denote simulation results.

Considering the stiffness of nylon cable k_c, and the stiffness of the linear spring k_s, the total stiffness of the cable can be found by

$$k = \frac{k_s \cdot k_c}{k_s + k_c}. \tag{21}$$

Fig. 15 shows the cable tension F that were measured and the elongation of cable calculated using Eq. (13) with deflection angle of pendulum θ. Linear curve fitting yields

$$F = 0.5804x + 6.089, \tag{22}$$

where x denotes the elongation of nylon cable. This curve fitting can achieve R-squared value of 0.9991, showing that it closely matches the experiment results. Therefore, the nylon cable stiffness k_c is 0.5804N/mm, and the total stiffness $k_1 = 0.309$N/mm for the use of spring 1 and the total stiffness $k_2 = 0.156$ N/mm for the use of spring 2 are then obtained based on Eq. (21).

4.3. Experiments

Experiments were performed to assess the influences of pretension F_0, configuration number N and spring stiffness k on the performance of stiffness. In the testing, external torque is applied on the pendulum to rotate the joint following the sequence, $0 \rightarrow 0.7 \rightarrow 0 \rightarrow$ -0.7 $\rightarrow$ 0rad, and at least four periods of this sequence are recorded for every measurement.

4.3.1. Effect of pretension F_0

During the test, four different pretensions $F_0 = 3.8$N, 12.8N, 21.2N, 26.3N were set in the test rig for $N = 1$ and $k_1 =$ 0.309N/mm. The torque-deflection relationships based on different pretensions are shown in Fig. 16. As can be seen, the simulation results indicated by the solid lines closely match the measurements of the dotted lines with maximum error ±46N·mm. Different stiffness varying behaviors can also be observed clearly. The joint shows first hardening behavior at beginning with $F_0 = 3.8$N, and then transits to softening behavior with the increase of pretension, which is consistent with

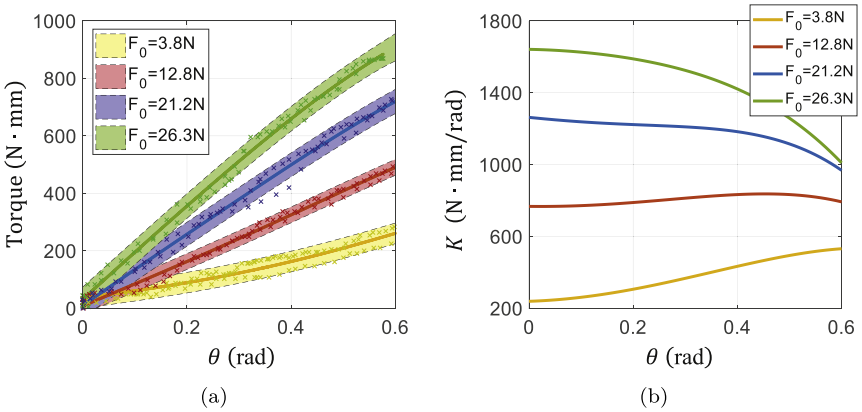

Fig. 17. (a) Plot of torque versus joint deflection θ for varying pretension F_0, wherein the dots denote experiment results, and the solid lines denote the fitting results, and the shadow areas denote the confidence intervals. (b) Plot of joint stiffness versus deflection θ for varying pretension F_0. $N = 1$, $k_1 = 0.309$N/mm.

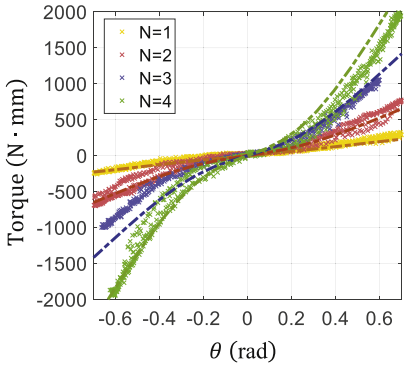

Fig. 18. Plot of torque versus deflection θ based on different configurations for $F_0 = 3.5$N, wherein the dots denote experiment results, and the dash-dot lines denote simulation results.

the analysis in Sections 2 and 3. Fig. 17(a) shows the fitted curves for the measurements, obtained with fifth-order polynomials. Fig. 17(b) shows the stiffness variation with respect to deflection obtained by derivation of the fitting curves. In both figures, we show only the results in the range of $\theta \in [0, 0.6]$rad for clarity. The variations of stiffness behaviors with different pretension can be observed clearly.

4.3.2. Effect of configuration N

Different configurations of $N = 1, 2, 3, 4$ were set in the JVSR for $F_0 = 3.5$N and $k_1 = 0.309$N/mm. As depicted in Fig. 18, the measured results are generally in accordance with the simulated ones with maximum error ± 110N·mm. In Fig. 19, the experimental results show that increasing N leads to a higher stiffness value as expressed in Eq. (19). We also see that the hardening behavior is more evident with the increase of N. That is because the weight of $\hat{K}_{eq,1}$ in Eq. (19) increases as N increases, and $\hat{K}_{eq,1}$ shows hardening behavior around the position of $\theta = 0$ as discussed in Section 2.

4.3.3. Effect of spring stiffness k

Finally, a test was performed to evaluate the influence of spring stiffness k on the performance of JVSR for the condition of $N = 4$ and $F_0 = 3$ N. The test results in Fig. 20 are generally in accordance with the simulated ones, although the mechanism shows hysteresis behaviors in the experimental results, in which the maximum error is ± 122N·mm. Fig. 21 shows stiffness variation, wherein the influence of k on the stiffness performance can be observed clearly. As can be seen, the hardening behavior is more evident with a more stiff spring, which is in accordance with Eq. (19), where the value of the hardening behavior related term, $N^2 c_1 l_3^2 k \hat{K}_{eq,1}$, is large for a high stiffness k. Moreover, the two curves meet nearly at the same point for $\theta = 0$, which demonstrates the zero-stiffness property of $\hat{K}_{eq,1}$ at singularity of the compliant joint mechanism.

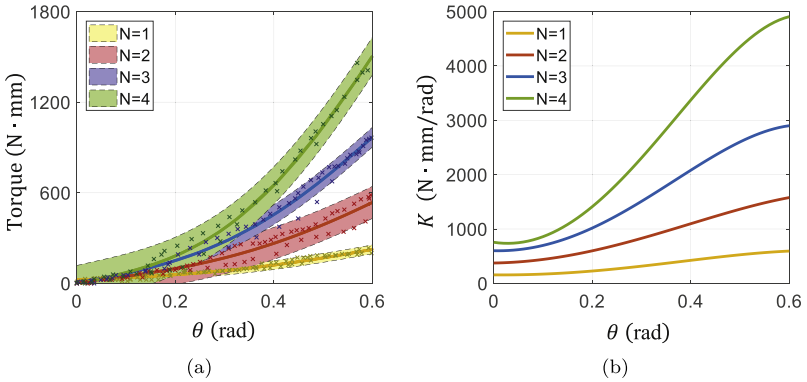

Fig. 19. (a) Plot of torque versus joint deflection θ of different configurations, wherein the dots denote experiment results, and the solid lines denote the fitting results, and the shadow areas denote the confidence intervals. (b) Plot of joint stiffness versus deflection θ for different configurations.

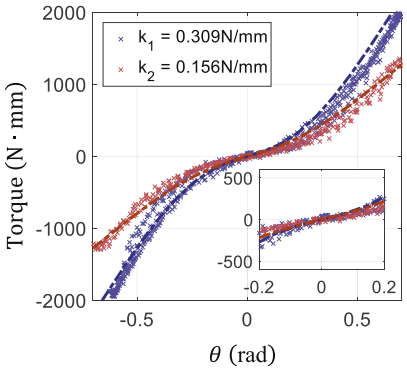

Fig. 20. Plot of torque versus deflection θ for different springs with $N = 4$ and $F_0 = 3$N, wherein the dots denote experiment results, and the dash-dot lines denote simulation results.

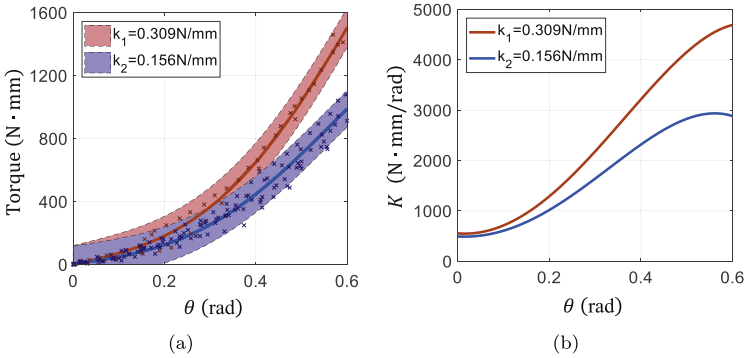

Fig. 21. (a) Plot of torque versus joint deflection θ for different springs, wherein the dots denote experiment results, and the solid lines denote the fitting results, and the shadow areas denote the confidence intervals. (b) Plot of joint stiffness versus deflection θ for springs of different stiffness.

5. A case of design

We herein include a case to illustrate how the new joint mechanism is scalable to a specific application. In the case, the application considered is the joints of an upper-body exoskeleton [38,39] as shown in Fig. 22.

In the exoskeleton, three active joints (two for shoulder joint, and one for elbow joint) are used. The torque requirements of joints are shown in Table 2. The geometric parameters of JVSR are summarized in Table 3, where N_s and N_e

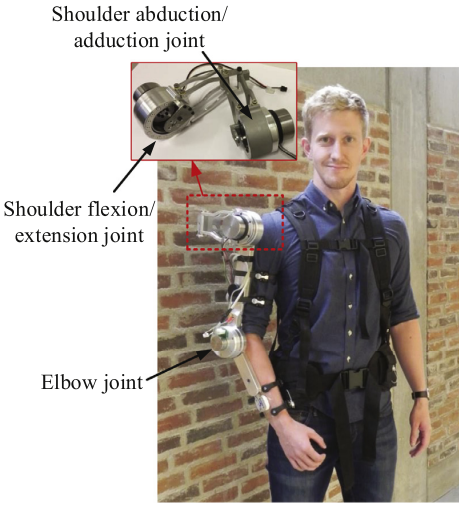

Fig. 22. An upper-body exoskeleton [38,39].

Table 2
Output torques and dimensions of the upper-body exoskeleton joints [38,39].

Joint	Related torque	Diameter
Shoulder flexion/extension	11.2 N·m	95 mm
Shoulder abduction/adduction	18 N·m	85 mm
Elbow	10 N·m	95 mm

Table 3
Parameters of the compliant actuator.

n	λ	λ_1	l_3	k	N_e	N_s
5	0.6	0.15	30 mm	2.3 N/mm	4	5

stand for the reconfiguration numbers for the shoulder abduction/adduction joint, and elbow and shoulder flexion/extension joints, respectively. Considering the maximum deflection angle in a general compliance joint [8], we define θ in the range of $[-0.45, 0.45]$rad. According to the torque model Eq. (20) and the above defined values, and given that $F_0 = 40$N and $T = 20$N·m, the equivalent stiffness of elastic element can be calculated as $k \approx 2.3$N/mm. Fig. 23 shows the functions of maximum output torque and the maximum stiffness with respect to the changes of deflection angles when different configurations are applied. We can see that in this case the JVSR with $N_s = 5$ is applicable to the shoulder abduction/adduction joint, and the JVSR with $N_e = 4$ is applicable to the shoulder flexion/extension and elbow joints.

It should be noted that the spring in the designed JVSR is selected to withstand the maximum tension,

$$F_{\max} = Nk\delta l\,|_{\theta=\theta_{\max}} + F_0 = 131\,\mathrm{N}, \tag{23}$$

and the corresponding maximum tension length,

$$\Delta L_{max} = N\delta l\,|_{\theta=\theta_{\max}} + \frac{F_0}{k} = 56\,\mathrm{mm}. \tag{24}$$

The cable is selected considering its strength limitation to withstand the maximum tension. We choose a steel wire, and its cross-sectional area A satisfies [40]

$$A \geq \frac{F_{\max}}{\sigma_f} = 0.187\,\mathrm{mm}^2, \tag{25}$$

where σ_f is the tensile strength for the steel material. A steel cable with a diameter of 0.9mm is selected, which can withstand the maximum tension without failure. To avoid the long extension of a linear spring, a torsional spring as shown in Fig. 25 is used. The stiffness k_t of torsional spring satisfies

$$k_t = l_m^2 \cdot k_s = 230\,\mathrm{N}\cdot\mathrm{mm/rad}, \tag{26}$$

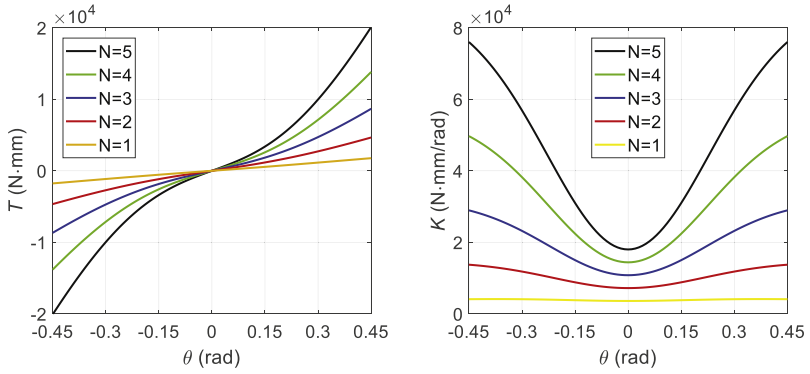

Fig. 23. Functions of (a) the maximum output-torque and (b) the maximum stiffness with respect to the changes of deflection angles for different configurations for $F_0 = 30$N.

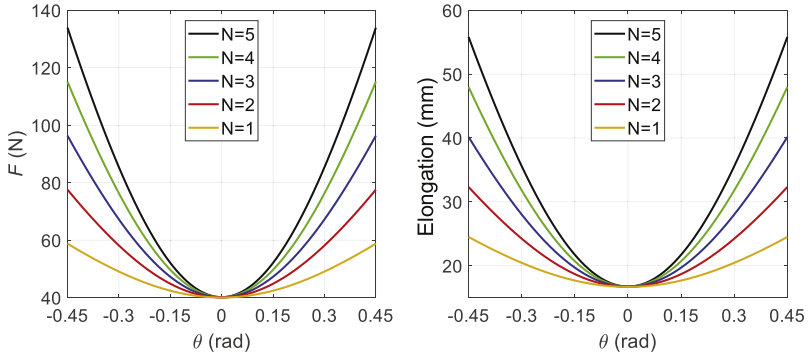

Fig. 24. The functions of (a) the spring tension and (b) the corresponding elongation length with respect to the changes of deflection angles of the JVSR with different configuration.

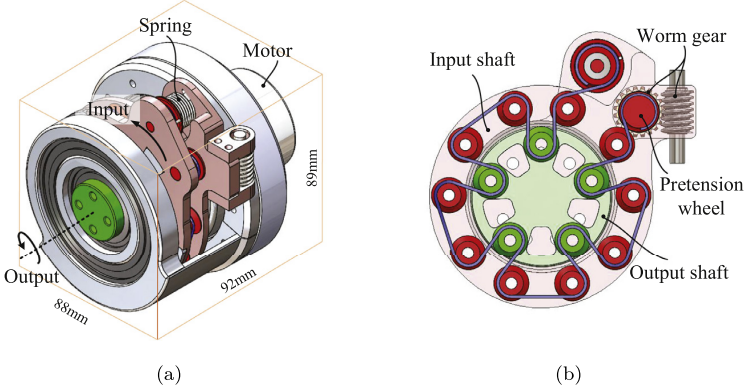

Fig. 25. An embodiment of JVSR. (a) 3D model. (b) Design of cable arrangement.

Table 4
Specifications of the steel wire and torsional spring.

Specification	Values
Material of the steel wire	304 stainless steel
Tensile strength of the cable material σ_f	700 MPa
Diameter of the wire ϕ	0.9 mm
Material of the spring	SWP-B steel
Desired maximum deflection of the spring	± 5.6 rad
Mean diameter of the spring D	20 mm
Wire diameter of the spring d	1.8 mm
Number of turns of the spring	7

where l_m is the length of moment arm, which is set to 10mm.

An embodiment of the design is shown in Fig. 25. A worm gear is used to adjust manually pretension of the cable. The specifications of the selected steel cable and torsional spring are listed in Table 4. The total mass of the designed joint is 0.987kg, including the motor.

6. Conclusions

This paper presents an innovative design of revolute joint of variable stiffness with reconfigurability (JVSR). The design of JVSR features the capabilities of adjusting initial stiffness and changing stiffness behavior within a compact architecture. In this work, a mathematical model of JVSR is developed and validated experimentally. A design case is included to illustrate its implementation in robotic joints.

The main contribution of this work is the novel reconfigurable design of the compliant joint mechanism. The new compliant joint is able to change its stiffness from zero to a specified range, which is determined through design parameters and configurations. Moreover, the new joint can vary its stiffness in different modes including linear, hardening and softening modes. The three modes can be observed in all configurations by adjusting spring pretension. The joint shows hardening mode first with small spring pretension, then transits to linear mode and finally softening mode with the increase of spring pretension.

The novel revolute joint is able to achieve various stiffness performance and large range of stiffness variation. A potential application of JVSR is to be used as a passive compliant joint or to integrate into electric motors to build compliant actuators. The new compliant joint can find their applications in exoskeletons, rehabilitation robots and servicing robots. Moreover, it can be used in walking, hopping, and running robots where the energy storage capability is required to improve the efficiency. JVSR can also be applicable to new coupling device, which is very common in motion transmissions. For future work, implementation case of modular robot joint based on the proposed design will be exploited.

Acknowledgment

The research is in part supported by Innovation Fund Denmark through Grand Solutions project Exo-aider. The first author acknowledges the CSC scholarship for his study at Aalborg University, Denmark.

Supplementary material

Supplementary material associated with this article can be found, in the online version, at doi:10.1016/j.mechmachtheory.2018.12.011.

References

[1] B. Vanderborght, A. Albu-Schaeffer, et al., Variable impedance actuators: a review, Rob. Auton. Syst. 61 (12) (2013) 1601–1614.
[2] H. Vallery, J. Veneman, E. van Asseldonk, R. Ekkelenkamp, M. Buss, H. van Der Kooij, Compliant actuation of rehabilitation robots, IEEE Rob. Autom. Mag. 15 (3) (2008) 60–69.
[3] N. Vitiello, T. Lenzi, S. Roccella, S.M.M.D. Rossi, E. Cattin, F. Giovacchini, F. Vecchi, M.C. Carrozza, NEUROExos: a powered elbow exoskeleton for physical rehabilitation, IEEE Trans. Rob. 29 (1) (2013) 220–235.
[4] J.A. Blaya, H. Herr, Adaptive control of a variable-impedance ankle-foot orthosis to assist drop-foot gait, IEEE Trans. Neural Syst. Rehabil. Eng. 12 (1) (2004) 24–31.
[5] J.F. Veneman, R. Ekkelenkamp, R. Kruidhof, F.C. van der Helm, H. van der Kooij, A series elastic- and Bowden-cable-based actuation system for use as torque actuator in exoskeleton-type robots, Int. J. Rob. Res. 25 (3) (2006) 261–281.
[6] W.M. dos Santos, G.A. Caurin, A.A. Siqueira, Design and control of an active knee orthosis driven by a rotary series elastic actuator, Control Eng. Pract. 58 (2017) 307–318.
[7] K. Kong, J. Bae, M. Tomizuka, Control of rotary series elastic actuator for ideal force-mode actuation in human–robot interaction applications, IEEE/ASME Trans. Mechatron. 14 (1) (2009) 105–118.
[8] K. Kong, J. Bae, M. Tomizuka, A compact rotary series elastic actuator for human assistive systems, IEEE/ASME Trans. Mechatron. 17 (2) (2012) 288–297.
[9] G. Chen, P. Qi, Z. Guo, H. Yu, Mechanical design and evaluation of a compact portable kneeanklefoot robot for gait rehabilitation, Mech. Mach. Theory 103 (2016) 51–64.

[10] H.Q. Vu, X. Yu, F. Iida, R. Pfeifer, Improving energy efficiency of hopping locomotion by using a variable stiffness actuator, IEEE/ASME Trans. Mechatron. 21 (1) (2016) 472–486.
[11] J.W. Hurst, A.A. Rizzi, Series compliance for an efficient running gait, IEEE Rob. Autom. Mag. 15 (3) (2008) 42–51.
[12] R.V. Ham, B. Vanderborght, M.V. Damme, B. Verrelst, D. Lefeber, MACCEPA, the mechanically adjustable compliance and controllable equilibrium position actuator: design and implementation in a biped robot, Rob. Auton. Syst. 55 (10) (2007) 761–768.
[13] A. Albu-Schäffer, S. Haddadin, C. Ott, A. Stemmer, T. Wimbck, G. Hirzinger, The DLR lightweight robot: design and control concepts for robots in human environments, Ind. Robot Int. J. 34 (5) (2007) 376–385.
[14] L. Zhou, S. Bai, M.R. Hansen, Integrated dimensional and drive-train design optimization of a light-weight anthropomorphic arm, Rob. Auton. Syst. 60 (1) (2012) 113–122.
[15] L. Zhou, S. Bai, A new approach to design of a lightweight anthropomorphic arm for service applications, J. Mech. Robot 7 (3) (2015) 031001.
[16] T. Verstraten, J. Geeroms, G. Mathijssen, B. Convens, B. Vanderborght, D. Lefeber, Optimizing the power and energy consumption of powered prosthetic ankles with series and parallel elasticity, Mech. Mach. Theory 116 (2017) 419–432.
[17] T. Verstraten, P. Beckerle, R. Furnémont, G. Mathijssen, B. Vanderborght, D. Lefeber, Series and parallel elastic actuation: impact of natural dynamics on power and energy consumption, Mech. Mach. Theory 102 (2016) 232–246.
[18] S. Wolf, G. Grioli, et al., Variable stiffness actuators: review on design and components, IEEE/ASME Trans. Mechatron. 21 (5) (2016) 2418–2430.
[19] J. Austin, A. Schepelmann, H. Geyer, Control and evaluation of series elastic actuators with nonlinear rubber springs, in: Proceedings of the IEEE/RSJ International Conference on Intelligent Robots and Systems, 2015, pp. 6563–6568.
[20] J.J. Park, Y.J. Lee, J.B. Song, H.S. Kim, Safe joint mechanism based on nonlinear stiffness for safe human-robot collision, in: Proceedings of the IEEE International Conference on Robotics and Automation, 2008, pp. 2177–2182.
[21] S.A. Migliore, E.A. Brown, S.P. DeWeerth, Novel nonlinear elastic actuators for passively controlling robotic joint compliance, J. Mech. Des. 129 (4) (2007) 406–412.
[22] T. Bacek, M. Moltedo, C. Rodriguez-Guerrero, J. Geeroms, B. Vanderborght, D. Lefeber, Design and evaluation of a torque-controllable knee joint actuator with adjustable series compliance and parallel elasticity, Mech. Mach. Theory 130 (2018) 71–85.
[23] S. Wolf, G. Hirzinger, A new variable stiffness design: matching requirements of the next robot generation, in: Proceedings of the IEEE International Conference on Robotics and Automation, 2008, pp. 1741–1746.
[24] S. Groothuis, R. Carloni, S. Stramigioli, A novel variable stiffness mechanism capable of an infinite stiffness range and unlimited decoupled output motion, Actuators 3 (2) (2014) 107–123.
[25] D. Hyun, H.S. Yang, J. Park, Y. Shim, Variable stiffness mechanism for human-friendly robots, Mech. Mach. Theory 45 (6) (2010) 880–897.
[26] A. Jafari, N.G. Tsagarakis, D.G. Caldwell, AwAS-II: a new actuator with adjustable stiffness based on the novel principle of adaptable pivot point and variable lever ratio, Proceedings of the IEEE International Conference on Robotics and Automation, pp. 4638–4643.
[27] A. Jafari, N.G. Tsagarakis, D.G. Caldwell, A novel intrinsically energy efficient actuator with adjustable stiffness (AwAS), IEEE/ASME Trans. Mechatron. 18 (1) (2013) 355–365.
[28] L. Liu, S. Leonhardt, B.J. Misgeld, Design and control of a mechanical rotary variable impedance actuator, Mechatronics 39 (2016) 226–236.
[29] H.V. Quy, L. Aryananda, F.I. Sheikh, F. Casanova, R. Pfeifer, A novel mechanism for varying stiffness via changing transmission angle, in: Proceedings of the IEEE International Conference on Robotics and Automation, 2011, pp. 5076–5081.
[30] J. Choi, S. Hong, W. Lee, S. Kang, M. Kim, A robot joint with variable stiffness using leaf springs, IEEE Trans. Rob. 27 (2) (2011) 229–238.
[31] X. Li, W. Chen, W. Lin, K.H. Low, A variable stiffness robotic gripper based on structure-controlled principle, IEEE Trans. Autom. Sci. Eng. 99 (2017) 1–10.
[32] M.G. Catalano, G. Grioli, M. Garabini, F. Bonomo, M. Mancini, N. Tsagarakis, A. Bicchi, VSA-CubeBot: a modular variable stiffness platform for multiple degrees of freedom robots, in: Proceedings of the IEEE International Conference on Robotics and Automation, 2011, pp. 5090–5095.
[33] N.G. Tsagarakis, I. Sardellitti, D.G. Caldwell, A new variable stiffness actuator (CompAct-VSA): design and modelling, in: Proceedings of the IEEE/RSJ International Conference on Intelligent Robots and Systems, 2011, pp. 378–383.
[34] I. Thorson, D. Caldwell, A nonlinear series elastic actuator for highly dynamic motions, in: Proceedings of the IEEE/RSJ International Conference on Intelligent Robots and Systems, 2011, pp. 390–394.
[35] M. Kilic, Y. Yazicioglu, D.F. Kurtulus, Synthesis of a torsional spring mechanism with mechanically adjustable stiffness using wrapping cams, Mech. Mach. Theory 57 (2012) 27–39.
[36] B. Vanderborght, N.G. Tsagarakis, C. Semini, R.V. Ham, D.G. Caldwell, MACCEPA 2.0: adjustable compliant actuator with stiffening characteristic for energy efficient hopping, in: Proceedings of the IEEE International Conference on Robotics and Automation, 2009, pp. 544–549.
[37] D. Owaki, A. Ishiguro, Enhancing stability of a passive dynamic running biped by exploiting a nonlinear spring, in: Proceedings of the IEEE/RSJ International Conference on Intelligent Robots and Systems, 2006, pp. 4923–4928.
[38] S. Bai, S. Christensen, M.R.U. Islam, An upper-body exoskeleton with a novel shoulder mechanism for assistive applications, in: Proceedings of the IEEE International Conference on Advanced Intelligent Mechatronics, 2017, pp. 1041–1046.
[39] S. Christensen, S. Bai, Kinematic analysis and design of a novel shoulder exoskeleton using a double parallelogram linkage, J. Mech. Robot. 10 (4) (2018) 041008.
[40] J. Gere, Mechanics of Materials, Thomson Learning, United States of America, 2004.

Chapter 5

Paper II

Nonlinear stiffness analysis of spring-loaded inverted slider crank mechanisms with a unified model

Zhongyi Li, Shaoping Bai, Weihai Chen, and Jianbin Zhang

The paper has been published in the
Journal of Mechanisms and Robotics Vol. 12(3): 031011, 2020.

Zhongyi Li
Department of Materials and Production,
Aalborg University,
Aalborg 9220, Denmark
e-mail: li@m-tech.aau.dk

Shaoping Bai[1]
Department of Materials and Production,
Aalborg University,
Aalborg 9220, Denmark
e-mail: shb@mp.aau.dk

Weihai Chen
School of Automation Science and Electrical Engineering,
Beihang University,
Beijing 100191, China
e-mail: whchenbuaa@126.com

Jianbin Zhang
School of Mechanical Engineering and Automation,
Beihang University,
Beijing 100191, China
e-mail: jbzhangbuaa@163.com

Nonlinear Stiffness Analysis of Spring-Loaded Inverted Slider Crank Mechanisms With a Unified Model

A mechanism with lumped-compliance can be constructed by mounting springs at joints of an inverted slider crank mechanism. Different mounting schemes bring change in the stiffness performance. In this paper, a unified stiffness model is developed for a comprehensive analysis of the stiffness performance for mechanisms constructed with different spring mounting schemes. With the model, stiffness behaviors of spring-loaded inverted slider crank mechanisms are analyzed. Influences of each individual spring on the overall performance are characterized. The unified stiffness model allows designing mechanisms for a desired stiffness performance, such as constant-torque mechanism and variable stiffness mechanism, both being illustrated with a design example and experiments.
[DOI: 10.1115/1.4045649]

Keywords: stiffness analysis, inverted slider crank mechanism, constant torque mechanism, variable stiffness mechanism, actuators and transmissions, compliant mechanisms, multi-body dynamics and exoskeletons

1 Introduction

Mechanisms with inherent compliance, such as constant-force/torque mechanisms [1–3], variable stiffness mechanisms [4,5], and bistable mechanisms [6,7], can be used for applications of service robots [8], exoskeletons [9], and vibration isolators [10,11]. Conventionally, these inherent compliance mechanisms can be obtained by adding springs to the joints of rigid-body mechanisms which exhibit nonlinear behaviors. A serial elastic actuator with hardening behavior, which can maintain large response bandwidth at large deflection and large torque resolution at low deflection, was reported in Ref. [12]. A new joint which can guarantee both position accuracy and collision safety with a softening behavior is described in Ref. [13]. Mechanisms of zero-stiffness with constant-force/torque used to balance gravitational force or external constant torque were reported in Refs. [14–16]. Passive vibration isolators constructed with elastic elements of negative stiffness were introduced in Refs. [10,11]. Mechanisms showing bistable behavior were presented in Ref. [17].

Mechanisms with inherent compliance can also be achieved by designing mechanisms with monolithic smart structures known as compliant mechanisms. They are applicable in vibration isolation systems [18], precision positioning systems [19], vibration energy harvesters [20], elastic actuators [21], mechanisms with constant torque/force outputs [2,22], and gravity-balancing mechanisms [23]. Designing of compliant mechanisms can adopt the pseudo-rigid-body approach [24,25], with which rigid-body mechanisms are first designed, then converted into compliant mechanisms.

The interest of this work is compliant mechanisms constructed by adding constant-stiffness springs at the joints of a mechanism, in particular, an inverted slider crank mechanism, as shown in Fig. 1. The mechanism can produce multiple behaviors including hardening, softening, negative stiffness, zero-stiffness, bistable behaviors, and irrational nonlinearity which can be found in Refs. [2,4,16,23,26–28]. Of these, the zero-stiffness property was utilized to construct the gravity-balancing mechanism or constant-torque mechanism. Hardening, softening, and linear behaviors of the mechanism were used in designing a variable stiffness joint with multiple modes [4]. It is noted that most of these works analyze the stiffness for each spring separately, while stiffness modeling and performance analysis accounting for the influences of all springs are yet not described in the literature.

In this paper, a unified stiffness model is developed for nonlinear behavior analysis of the spring-loaded inverted slider crank mechanism. With the model, the influences of each individual spring on the overall stiffness performance of the mechanism can be investigated readily. Moreover, the model allows us to construct a mechanism to achieve a desired stiffness performance. Two designs, one constant torque mechanism and the other variable stiffness mechanism, are developed and tested experimentally.

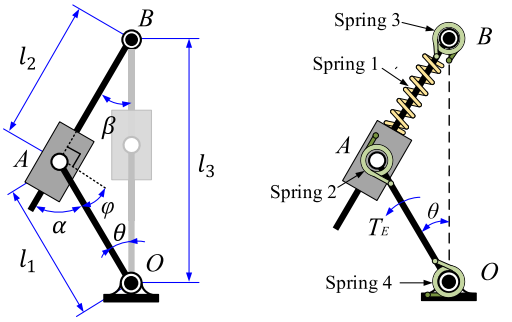

Fig. 1 Schematic diagrams of (*a*) a general type of inverted slider crank mechanism and (*b*) a spring-loaded inverted slider crank mechanism

[1]Corresponding author.

Contributed by the Mechanisms and Robotics Committee of ASME for publication in the Journal of Mechanisms and Robotics. Manuscript received June 25, 2019; final manuscript received November 7, 2019; published online December 9, 2019. Assoc. Editor: Leila Notash.

2 Modeling of a Compliant Inverted Slider Crank Mechanism

2.1 Kinematics of Inverted Slider Crank Mechanism. Figure 1(*a*) shows the schematic of an inverted slider crank mechanism, where θ, α, and β define the angle between the crank and base link, the angle between the crank and output link, and the angle between the output and base link, respectively. The lengths of the crank and the base link are l_1 and l_3, whereas l_2 defines the displacement of the slider along the output link. The kinematics of the mechanism satisfies

$$l_2 = \sqrt{l_1^2 + l_3^2 - 2l_1 l_3 \cos\theta} \tag{1a}$$

$$\alpha = \arcsin\frac{l_1 \sin\theta}{l_2} + \theta \tag{1b}$$

$$\beta = \arcsin\frac{l_1 \sin\theta}{l_2} \tag{1c}$$

Differentiating all equations with respect to θ, we obtain

$$\frac{dl_2}{d\theta} = \frac{l_1 l_3 \sin\theta}{l_2} = J_1 \tag{2a}$$

$$\frac{d\alpha}{d\theta} = \frac{l_1 l_2^2 \cos\theta - l_1^2 l_3 \sin^2\theta}{l_2^2\sqrt{l_2^2 - l_1^2\sin^2\theta}} + 1 = J_2 \tag{2b}$$

$$\frac{d\beta}{d\theta} = \frac{l_1 l_2^2 \cos\theta - l_1^2 l_3 \sin^2\theta}{l_2^2\sqrt{l_2^2 - l_1^2\sin^2\theta}} = J_3 \tag{2c}$$

where J_1, J_2, and J_3 are the Jacobians mapping the velocity from the input to the outputs.

Some special configurations of the mechanism should be noted. The first one is the singular configuration where the Jacobian is equal to zero or infinity. Table 1 summarizes all singular positions of the mechanism for $\theta \in (-\pi, \pi]$ rad. Singular configurations of the mechanism with $l_1 < l_3$ are shown in Fig. 2. Another special configuration is found at $\theta = 0$ rad for the mechanism of $l_1 = l_3$. In this configuration, the mechanism produces highly irrational nonlinearity [28] due to $\lim_{\theta\to 0^+} J_1 = 1$ and $\lim_{\theta\to 0^-} J_1 = -1$.

Table 1 Kinematic singularities of the inverted slider crank mechanism

$J_i = 0$ or ∞	Positions ($\theta \in (-\pi, \pi]$rad)
$J_1 = 0$	$\theta = 0$ rad ($l_1 \neq l_3$) and $\theta = \pi$ rad
$J_2 = 0$	$\theta = \pm\arccos\frac{l_3}{l_1}$ ($l_1 > l_3$)
$J_3 = 0$	$\theta = \pm\arccos\frac{l_1}{l_3}$ ($l_1 < l_3$)

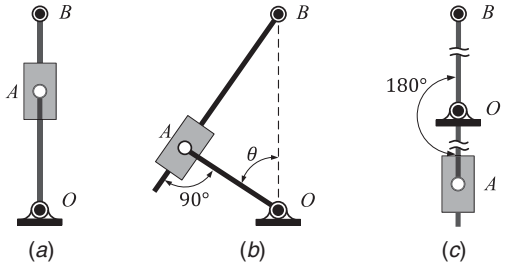

Fig. 2 Different types of singularities of the inverted slider crank mechanism for $l_1 < l_3$: (*a*) $J_1 = 0$ ($\theta = 0$ rad), (*b*) $J_2 = 0$ ($\theta = \arccos\lambda$ rad), and (c) $J_3 = 0$ ($\theta = \pi$ rad)

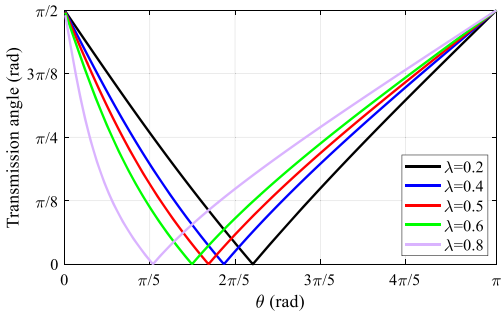

Fig. 3 Plot of φ versus θ for different λ

We introduce here a length ratio $\lambda = l_1/l_3$. It is noted that an angle $\theta = \arccos\lambda$ stands for a position where the transmission angle between crank and slider is zero. This transmission angle in the mechanism, referring to Fig. 1(*a*) is found as

$$\varphi = \begin{cases} \frac{\pi}{2} - \alpha & \text{if } 0 \le \theta \le \arccos\lambda \\ \alpha - \frac{\pi}{2} & \text{if } \arccos\lambda < \theta \le \pi \end{cases} \tag{3}$$

The relationships between φ and θ for different λ are shown in Fig. 3. As can be seen that, transmission angle φ decreases from π/2 rad at $\theta = 0$ rad and becomes zero when the mechanism reaches singular position $\theta = \arccos\lambda$. Afterwards, φ increases and reaches maximum π/2 rad at $\theta = \pi$ rad.

With the attachment of springs, the mobility of the linkage will be affected. Normally, the crank has a full rotatability in an inverted crank slider mechanism. For the mechanism in this study, the rotatability of its crank is subject to the limitation of torsional spring.

2.2 Stiffness Modeling. By adding springs to the inverted slider crank linkage as shown in Fig. 1(*b*), a mechanism with lumped-compliance is constructed. In this work, all links are considered as rigid. Without loss of generality, springs are mounted on three joints, namely, one tensile spring at the prismatic joint and two torsional springs at revolute joints. The stiffnesses of Springs 1, 2, 3, and 4 are noted by k_{AB}, k_A, k_B, and k_O, respectively. An equilibrium torque T_E applied on the crank is used to balance the force/torques deduced by the springs'elongation/deflections. According to the virtual work principle, we can obtain

$$T_E\delta\theta = F_{AB}\delta l_2 + T_A\delta\alpha + T_B\delta\beta + T_O\delta\theta \tag{4}$$

where δl_2, δα, δβ, and δθ are virtual elongation/deflections of the springs, and F_{AB}, T_A, T_B, and T_O are the spring force/torques. Combining Eq. (4) with Eq. (2), the static model of the mechanism is derived as

$$T_E = F_{AB}J_1 + T_AJ_2 + T_BJ_3 + T_O \tag{5}$$

According to Hooke's law, all spring forces/torques are expressed as

$$F_{AB} = k_{AB}(l_2 - l_{2,0}) + k_{AB}(l_{2,0} - l_f) = k_{AB}\delta l_2 + F_{AB0} \tag{6a}$$

$$T_A = k_A(\alpha - \alpha_0) + k_A(\alpha_0 - \alpha_f) = k_A\delta\alpha + T_{A0} \tag{6b}$$

$$T_B = k_B(\beta - \beta_0) + k_B(\beta_0 - \beta_f) = k_B\delta\beta + T_{B0} \tag{6c}$$

$$T_O = k_O(\theta - \theta_0) + k_O(\theta_0 - \theta_f) = k_O\delta\theta + T_{O0} \tag{6d}$$

where F_{AB0}, T_{A0}, T_{B0}, and T_{O0} define the spring pretensions which are related to the initial position θ_0 of the mechanism and the free length/angles of springs, l_f, α_f, β_f, and θ_f. Moreover, $l_{2,0}$ and α_0 denote the initial length/angles when $\theta = \theta_0$.

The overall stiffness of the mechanism K is defined by

$$\delta T_E = K \cdot \delta\theta \tag{7}$$

The overall stiffness can be deduced from Eqs. (5) and (7) as

$$K = K_{AB} + K_A + K_B + k_O \tag{8}$$

where

$$K_{AB} \equiv k_{AB}\left(J_1^2 + \frac{\delta J_1}{\delta\theta}\delta l_2\right) + F_{AB0}\frac{\delta J_1}{\delta\theta} = K_{AB,1} + K_{AB,2} \tag{9a}$$

$$K_A \equiv k_A\left(J_2^2 + \frac{\delta J_2}{\delta\theta}\delta\alpha\right) + T_{A0}\frac{\delta J_2}{\delta\theta} = K_{A,1} + K_{A,2} \tag{9b}$$

$$K_B \equiv k_B\left(J_3^2 + \frac{\delta J_3}{\delta\theta}\delta\beta\right) + T_{B0}\frac{\delta J_3}{\delta\theta} = K_{B,1} + K_{B,2} \tag{9c}$$

As we can see from Eq. (8), Spring 4 has a linear influence on the overall stiffness. We thus exclude k_O from the model and focus on the analysis of other springs. To this end, Eq. (8) becomes

$$K = K_{AB} + K_A + K_B \tag{10}$$

With length ratio λ introduced before, Eq. (9) is rewritten as

$$K_{AB} = k_{AB}l_3^2\hat{K}_{AB,1} + F_{AB0}l_3\hat{K}_{AB,2} \tag{11a}$$

$$K_A = k_A\hat{K}_{A,1} + T_{A0}\hat{K}_{A,2} \tag{11b}$$

$$K_B = k_B\hat{K}_{B,1} + T_{B0}\hat{K}_{B,2} \tag{11c}$$

Note that $\hat{K}_{AB,1}$, $\hat{K}_{AB,2}$, $\hat{K}_{A,1}$, $\hat{K}_{A,2}$, $\hat{K}_{B,1}$, and $\hat{K}_{B,2}$ in the equations are functions of λ and θ. In other words, they are factors influenced only by linkage geometry. The analysis on these factors can reveal the influences of the mechanism kinematics on the stiffness performance. Moreover, based on Eq. (11), the influences of geometric parameters, spring stiffness, and preload on the stiffness behavior can be studied separately.

The potential energy of the mechanism can be obtained by

$$U = \int T_E\, d\theta + U_0 \tag{12}$$

where U_0 is the initial potential energy which is contributed by pretensions of springs.

3 Stiffness Behaviors Analysis

The stiffness model shown in Eq. (10) indicates that the influences of Springs 1, 2, and 3 on the overall stiffness are the sum of their contributions. In this section, we study separately the stiffness properties of the mechanism for each spring, and look at the influences of design parameters on the stiffness performance.

3.1 Stiffness Behaviors of the Mechanism With Spring 1 Mounted. According to Eq. (10), the stiffness model of the mechanism is solely determined by K_{AB}. Based on Eq. (11), the influences of geometric parameters on the stiffness performance can be investigated by looking into the properties of $\hat{K}_{AB,1}$ and $\hat{K}_{AB,2}$ which change with respect to the parameters of λ and θ.

Figure 4 shows the distribution of $\hat{K}_{AB,1}$ and $\hat{K}_{AB,2}$ for a specified range of θ and λ. Different stiffness behaviors can be observed. For clarity, in this work, the stiffness behaviors are labelled as follows: ① zero-stiffness behavior, ② hardening behavior, ③ softening behavior, and ④ negative stiffness behavior.

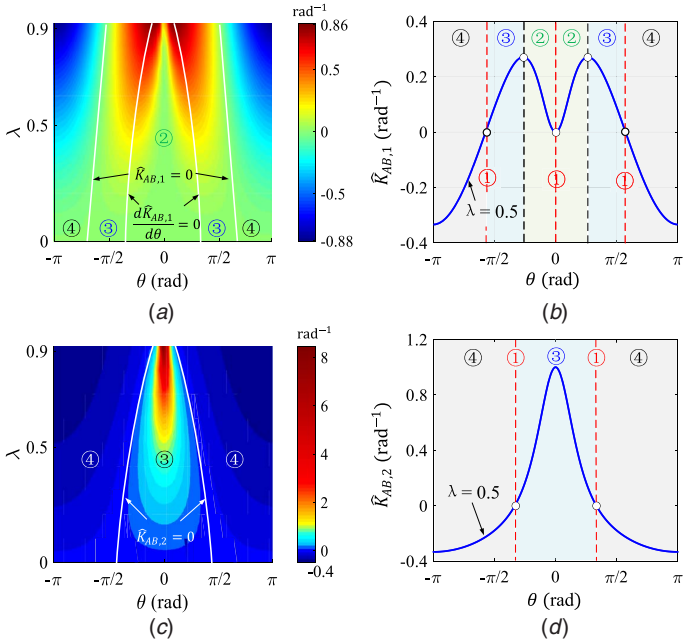

Fig. 4 Influence of θ and λ on $\hat{K}_{AB,1}$ and $\hat{K}_{AB,2}$: (*a*) overall variation of $\hat{K}_{AB,1}$, (*b*) variation of $\hat{K}_{AB,1}$ for $\lambda = 0.5$, (*c*) overall variation of $\hat{K}_{AB,2}$, and (*d*) variation of $\hat{K}_{AB,2}$ for $\lambda = 0.5$

Figure 4(*b*) shows a curve of $\hat{K}_{AB,1}$ generated for $\lambda = 0.5$. Its performance shows significant differences in five intervals and the curve is thus divided into five pieces, separated at the deflection angle $\theta|_{\hat{K}_{AB,1}=0}$ and $\theta|_{d\hat{K}_{AB,1}/d\theta=0}$. Four types of behaviors, namely zero-stiffness, hardening, softening, and negative stiffness behaviors, can be identified. The influence of λ is shown in Fig. 4(*a*). A larger λ will yield a smaller range of interval for hardening behavior but a larger maximum value of $\hat{K}_{AB,1}$, whereas a larger range of interval for negative stiffness behavior is achieved with the increase of λ.

Figure 4(*c*) shows changes of $\hat{K}_{AB,2}$ with the variations of λ and θ. Three types of behaviors including zero-stiffness, softening, and negative stiffness behaviors can be observed. Figure 4(*d*) shows the stiffness curve for $\lambda = 0.5$. We can clearly see that $\hat{K}_{AB,2}$ monotonically decreases as θ increases in the range of $\theta \in [0, \pi]$rad. Moreover, $\hat{K}_{AB,2}$ shows a softening behavior first. After reaching zero at $\theta = \theta|_{\delta J_1/\delta\theta=0}$, $\hat{K}_{AB,2}$ becomes negative.

Equation (11) implies that k_{AB} influences the mechanism's stiffness performance by scaling $\hat{K}_{AB,1}$, while the spring preload F_{AB0} influences the overall stiffness by scaling $\hat{K}_{AB,2}$. In other words, k_{AB} and F_{AB0} can be considered as the weight factors for $\hat{K}_{AB,1}$ and $\hat{K}_{AB,2}$ in the overall stiffness model. Figure 5(*a*) shows the curves of the overall stiffness in which three different preload values are separately applied on the spring. As shown in the figure, the stiffness behaviors change with F_{AB0}. A partial constant stiffness curve shown in Fig. 5(*b*) can be obtained by incorporating $\hat{K}_{AB,1}$ and $\hat{K}_{AB,2}$ with appropriate values of weight factors.

It should be noted that a mechanism with $\lambda = 1$ produces irrational nonlinearity at $\theta = 0$ rad as discussed in Sec. 2. Figure 6 shows the curves of $\hat{K}_{AB,1}$ and $\hat{K}_{AB,2}$ for $\lambda = 1$. As can be seen from Fig. 6(*b*), $\hat{K}_{AB,2}$ curve for $\lambda = 1$ has a cusp point at $\theta = 0$ rad.

The equilibrium position plays an important role in the stability of mechanism. The variations of equilibrium positions can be investigated by looking into the potential energy of the mechanism. According to Refs. [29,30], a local minimum of the potential energy stands for a stable equilibrium position, while the unstable equilibrium position refers to the local maximum of the potential energy. Based on Eq. (12), the potential energy reaches a local minimum point when T_E is zero and K is positive. On the other hand, the potential energy reaches a local maximum when T_E is zero and K is negative.

The potential energy of the mechanism is

$$U = \int F_{AB} J_1 \mathrm{d}\theta + \frac{1}{2k_{AB}} F_{AB0}^2 \tag{13}$$

The stable equilibrium positions are found as

$$\theta_{E,AB} = \begin{cases} 0 & \text{if } F_{AB0} \geq 0 \\ \pm \arccos\left(-\dfrac{F_{AB0}^2}{2\lambda k_{AB}^2} + \dfrac{F_{AB0}}{\lambda k_{AB}} - \dfrac{F_{AB0}}{k_{AB}} + 1\right) & \text{if } -2\lambda k_{AB} < F_{AB0} < 0 \\ \pm\pi & \text{if } F_{AB0} \leq -2\lambda k_{AB} \end{cases} \tag{14}$$

Two special values of pretension F_{AB0} should be noted. One is $F_{AB0} = 0$ N. The mechanism has only a single stable position for $F_{AB0} \geq 0$ N, but has double stable positions if $-2\lambda k_{AB} < F_{AB0} < 0$ N. Moreover, if $F_{AB0} = -2\lambda k_{AB}$, the spring has a free length of $(\lambda + 1) \cdot l_3$. The mechanism has stable equilibrium positions at $\theta = \pi$ or $-\pi$ rad for $F_{AB0} \leq -2\lambda k_{AB}$. The stable positions

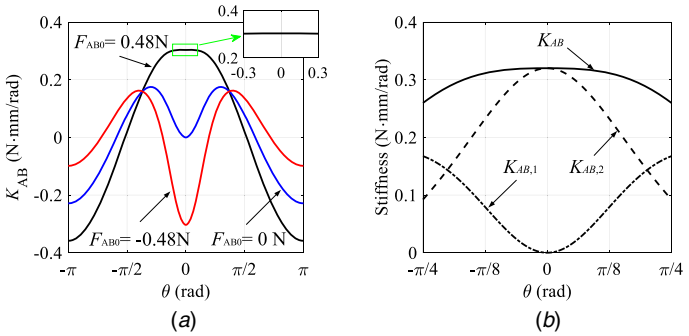

Fig. 5 (*a*) Changes of the overall stiffness, K_{AB}, with the variation of F_{AB0} and (*b*) constant stiffness behavior

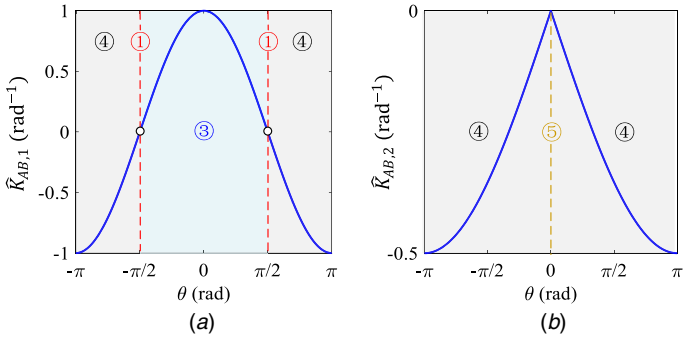

Fig. 6 Curves of (*a*) $\hat{K}_{AB,1}$ and (*b*) $\hat{K}_{AB,2}$ for $\lambda = 1$

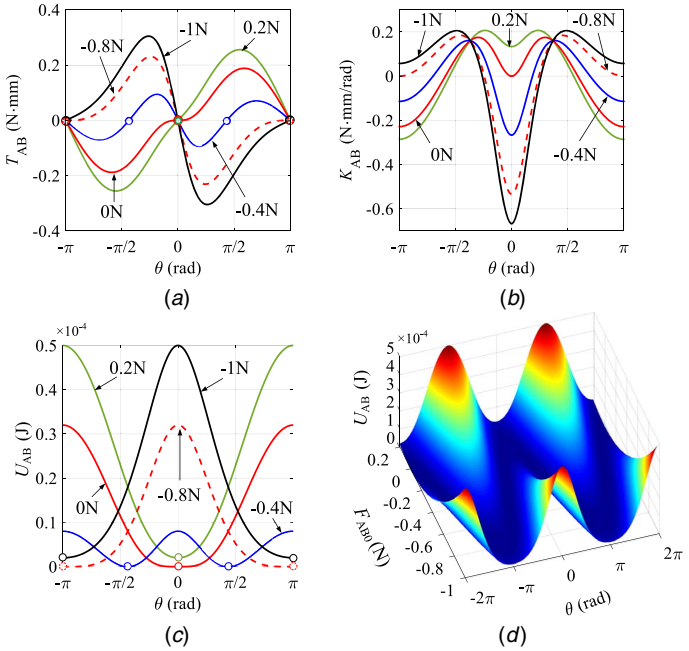

Fig. 7 Variations of stable equilibrium positions for $F_{AB0} = 0.2$, 0, −0.4, −0.8, and −1 N, when $k_{AB} = 1$ N/mm and $\lambda = 0.4$: (*a*) torque-angle curves, (*b*) stiffness-angle curves, (*c*) potential energy U_{AB} as a function of the deflection angle θ, and (*d*) influence of spring preload F_{AB0} on U_{AB}. In the figures, circles represent the stable equilibrium positions

on different curves are demonstrated in Fig. 7 where the influences of the spring preload can be observed clearly.

3.2 Stiffness Behaviors of the Mechanism With Spring 2 Mounted. For this mechanism, the stiffness of the mechanism is solely determined by K_A. According to Eq. (11), stiffness k_A and pretension T_{A0} affect the overall stiffness by scaling $\hat{K}_{A,1}$ and $\hat{K}_{A,2}$, respectively. The influences of λ and θ can be investigated by looking into the properties of $\hat{K}_{A,1}$ and $\hat{K}_{A,2}$.

Figures 8(*a*) and 8(*b*) show changes of $\hat{K}_{A,1}$ with respect to θ and λ. As can be seen from Fig. 8(*a*), $\hat{K}_{A,1}$ varies in five regions, separated at the deflection angle $\theta|_{\hat{K}_{A,1}=0}$. Each region stands for a specific stiffness behavior. Four types of behaviors, namely zero-stiffness, hardening, softening, and negative stiffness behaviors, can be identified. Note that among these behaviors, the negative stiffness behavior can be observed only when the length ratio λ is larger than 0.53. From Fig. 8(*b*), we can see that a λ larger than 0.53 causes two zero-stiffness points in the range of $\theta \in [0, \pi]$ rad. Within the two points, $\hat{K}_{A,1}$ becomes negative.

Figures 8(*c*) and 8(*d*) show changes of $\hat{K}_{A,2}$. As shown in Fig. 8(*c*), the white line of $\hat{K}_{A,2} = 0$, which refers to zero stiffness, separates the whole region into two zones, one for positive stiffness behavior and the other for negative stiffness behavior. In the positive stiffness zone, two types of behaviors, hardening and softening behaviors, can be identified. The change of the range of each behavior with the influence of λ can be observed clearly in Fig. 8(*c*). Figure 8(*d*) plots a specific curve of $\hat{K}_{A,2}$ for $\lambda = 0.6$.

It is noted that, when $\lambda = 1$, J_2 is constant which is equal to 0.5, and the stiffness of the mechanism is equal to $\frac{1}{4}k_A$ which indicates a constant stiffness behavior.

As the potential energy increases monotonically with θ, only one stable equilibrium position can be found in the mechanism. The stable equilibrium position $\theta_{E,A}$ satisfies the following equation:

$$\theta_{E,A} + \arcsin\frac{l_1 \sin\theta_{E,A}}{l_2} - \frac{T_{A0}}{k_A} = 0, \quad 0 < \lambda < 1 \tag{15}$$

3.3 Stiffness Behaviors of the Mechanism With Spring 3 Mounted. For a mechanism constructed in this way, its stiffness is solely determined by K_B.

Figure 9(*a*) shows changes of $\hat{K}_{B,1}$ as a function of θ and λ. As can be seen in the figure, four types of behaviors, namely zero-stiffness, hardening, softening stiffness, and negative stiffness behaviors, can be observed. The regions of these behaviors change with the variation of θ and λ, which can be seen clearly in Fig. 9(*a*). Figure 9(*b*) shows a specific curve of $\hat{K}_{B,1}$ for $\lambda = 0.5$.

Figures 9(*c*) and 9(*d*) show changes of $\hat{K}_{B,2}$. In Fig. 9(*c*), the line of $\hat{K}_{B,2} = 0$ separates the whole region into a positive stiffness behavior zone and negative stiffness zone. In the positive stiffness zone, two types of behaviors, hardening and softening behaviors, can be identified. The range of each behavior varying with λ is clearly shown in Fig. 9(*c*). Figure 9(*d*) shows a curve of $\hat{K}_{B,2}$ for $\lambda = 0.5$. From the figure, each type of behavior can be observed clearly.

According to Eq. (11), both stiffness k_B and pretension T_{B0} affect the overall stiffness by scaling $\hat{K}_{B,1}$ and $\hat{K}_{B,2}$ respectively. In addition, we can see from the equation that the parameter of l_3 has no effect on the stiffness K_B.

It is noted that, when $\lambda = 1$, J_3 is a constant which is equal to −0.5. The stiffness of the mechanism is $\frac{1}{4}k_B$ showing constant stiffness behavior.

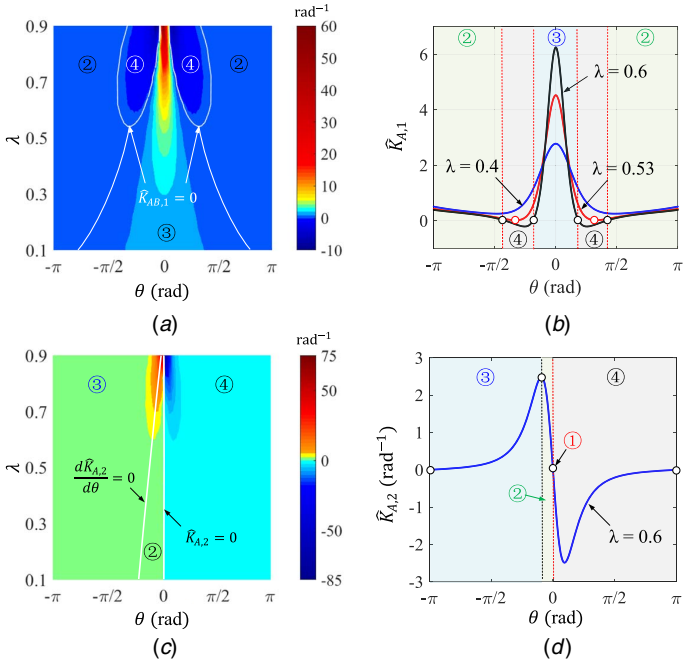

Fig. 8 Influences of θ and λ: (*a*) overall variation of $\hat{K}_{A,1}$, (*b*) variations of $\hat{K}_{A,1}$ for λ = 0.4, 0.53 and 0.6, (*c*) overall variation of $\hat{K}_{A,2}$, and (*d*) variation of $\hat{K}_{A,2}$ for λ = 0.6

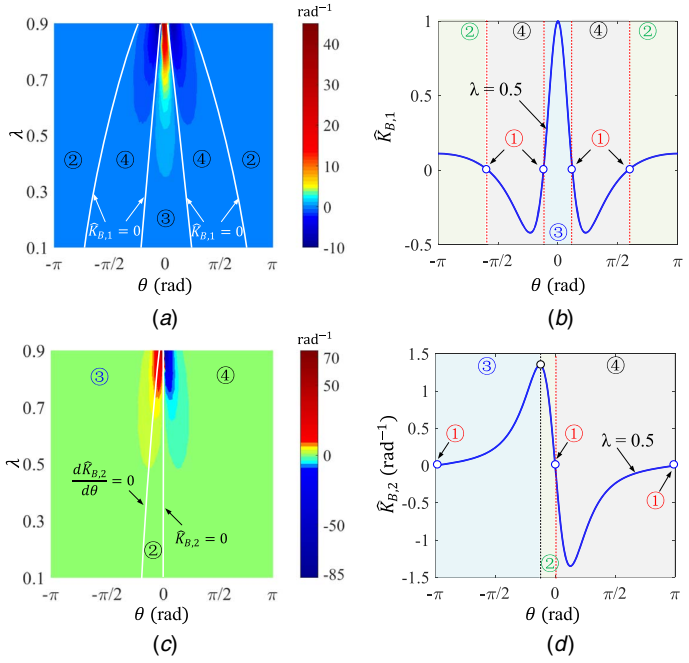

Fig. 9 Stiffness performances of $\hat{K}_{B,1}$ and $\hat{K}_{B,2}$: (*a*) $\hat{K}_{B,1}$ as a function of θ and λ, (*b*) variation of $\hat{K}_{B,1}$ for λ = 0.5, (*c*) $\hat{K}_{B,2}$ as a function of θ and λ, and (*d*) variation of $\hat{K}_{B,2}$ for λ = 0.5

For the mechanism, the potential energy becomes

$$U = \int T_B J_3 \mathrm{d}\theta + \frac{1}{2k_B} T_{B0}^2 \tag{16}$$

The stable equilibrium positions of the mechanism are found as

$$\theta_{E,B} = \begin{cases} -\arccos\lambda & \text{if } \tau_{B0} \geq \tau_{B,s} \\ \arccos\lambda & \text{if } \tau_{B0} \leq -\tau_{B,s} \\ \arccos\left(\frac{1}{\lambda}\left(\sin^2\frac{\tau_{B0}}{k_B} \pm \sqrt{\sin^4\frac{\tau_{B0}}{k_B} - \sin^2\frac{\tau_{B0}}{k_B}\left(\lambda^2+1\right)+\lambda^2}\right)\right) & \text{if } -\tau_{B,s} < \tau_{B0} \leq 0 \\ -\arccos\left(\frac{1}{\lambda}\left(\sin^2\frac{\tau_{B0}}{k_B} \pm \sqrt{\sin^4\frac{\tau_{B0}}{k_B} - \sin^2\frac{\tau_{B0}}{k_B}\left(\lambda^2+1\right)+\lambda^2}\right)\right) & \text{if } \tau_{B0} < \tau_{B,s} \end{cases} \tag{17}$$

where $\tau_{B,s} = k_B\left(\pi/2 - \arccos\lambda\right)$ represents a critical preload of the mechanism which determines whether the system at a singular position of $J_3 = 0$ is stable or not. The system is stable at the singular position if $\tau_{B0} \geq \tau_{B,s}$ or $\tau_{B0} \leq -\tau_{B,s}$. Figure 10 shows stable positions on different curves for demonstration, in which the influences of pretension τ_{B0} can be observed clearly.

4 Construction of a Constant-Torque Mechanism

The unified stiffness model allows us to design mechanisms for desired stiffness behaviors. This can be obtained by mounting appropriate springs on the joints and assigning appropriate values of springs' stiffnesses and preloads. In Sec. 3, the basic stiffness characteristics, $\hat{K}_{AB,1}$, $\hat{K}_{AB,2}$, $\hat{K}_{A,1}$, $\hat{K}_{A,2}$, $\hat{K}_{B,1}$, and $\hat{K}_{B,2}$ are analyzed. Based on these basic stiffness characteristics, it is possible to construct a desired stiffness behavior by proper compliance design.

We herein show an example to construct a constant-torque mechanism. Similar mechanisms can found their applications in dynamic-torque balancing systems and robots [14–16].

4.1 Method. A constant-torque mechanism shows zero-stiffness behavior in its working range. Zero-stiffness behavior can be achieved by incorporating a mechanism of positive stiffness interval and a mechanism of negative stiffness interval. The method is described as follows:

(1) Specifying a position of θ to achieve zero-stiffness and a constant torque T_C, and identifying a negative stiffness behavior and a positive stiffness behavior from the mechanisms studied in Sec. 3 for a given length ratio of λ.
(2) Assigning θ, λ, and the stiffness and the pretension of the spring generating negative stiffness behavior to Eqs. (5)

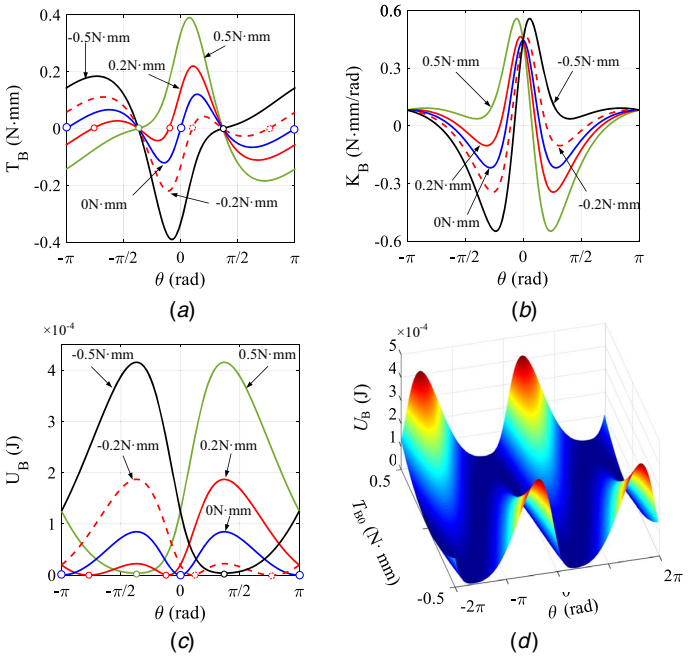

Fig. 10 Variations of stable equilibrium positions for $T_{B0} = \pm 0.2, \pm 0.5$ and 0 N/mm, when $k_B = 1$ N/mm/rad and $\lambda = 0.4$: (*a*) torque-angle curves, (*b*) stiffness-angle curves, (c) potential energy U_B as a function of the deflection angle θ, and (*d*) influence of spring preload T_{B0} on U_B. In the figures, circles represent the stable equilibrium positions.

and (10), and letting $K=0$ and $T_E=T_C$ to find the stiffness and the pretension of the spring generating positive stiffness behavior.

(3) Identifying the range of the zero stiffness interval. Herein, we consider that the mechanism works in the zero stiffness mode, if the torque satisfies

$$\xi_C = \left|\frac{T_{E,\max} - T_{E,\min}}{T_C}\right| \times 100\% \le 5\% \tag{18}$$

4.2 Design of a Constant-Torque Mechanism. A constant-torque mechanism was designed to justify the proposed method for achieving zero stiffness. The mechanism is designed with zero-stiffness behavior at $\theta=\pi/3$ rad and has constant torque $T_C=380$ N/mm within $\theta=\pi/3\pm0.5$ rad.

Following the proposed method, mechanisms which have positive stiffness behavior and negative stiffness behavior should be found at first. This can be achieved readily by using the results of stiffness analysis in Sec. 3. From the results, a positive stiffness behavior and a negative stiffness behavior can be generated at $\theta=\pi/3$ rad by including Spring 1 and Spring 3 in the mechanism.

The mechanism utilizing Spring 1 is constructed with a cable wrapped on three pulleys, one on joint A and the other two on the ground, as shown in Fig. 11. The ends of the cable each are connected to a linear spring (Spring 1) and the ground with preload F_{AB0}. With such a design, the linear spring is stretched as the crank OA rotates. The elongation l_2' of the spring is thus a function of θ. The Jacobian of the mechanism is given by

$$J_1' = \frac{dl_2'}{d\theta} \tag{19}$$

From the kinematics of the mechanism shown in Fig. 11, the following equation is found:

$$l_2' = c\cdot(l_1 + l_2 - l_3) \tag{20}$$

where $c\approx 2$ is a factor describing the influences of real construction on the mechanical advantage J_1. The detailed expression of c can be found in the Appendix.

Figure 12 shows the design of the mechanism with Spring 3 mounted. In the design, a torsion spring is mounted as such that one leg is fixed to the ground, and the other leg is rotated around joint B as the crank OA rotates. A pulley embedded bearing is used between the crank and the leg of spring to reduce friction. Noting that, as shown in Fig. 12, the deflection angle β′ of torsion spring is a function of geometric parameters r_1, r_2, and θ, which is found as

$$\beta' = \arccos\frac{r_2 - r_1}{l_2} - \arccos\frac{r_2 - r_1}{l_3 - l_1} + \beta \tag{21}$$

where r_1 and r_2 are the radii of the pulley and torsion spring.

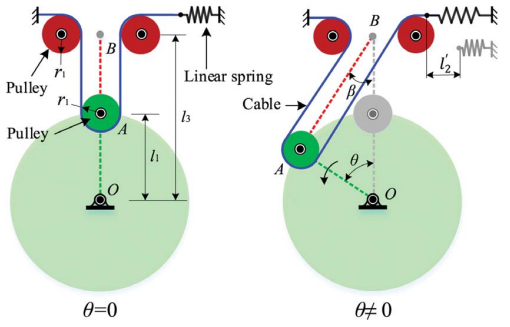

Fig. 11 Schematic design of a mechanism with Spring 1 mounted for generating positive stiffness behavior

The Jacobian of the mechanism is rewritten as

$$J_3' = \frac{d\beta'}{d\theta} \tag{22}$$

In the design, the mechanisms shown in both Figs. 11 and 12 were combined to generate zero stiffness behavior as shown in Fig. 13(*a*). In the mechanism, the cable is routed around a winch to facilitate adjustment of preload F_{AB0} of the linear spring. The geometric parameters of the mechanism are given in Table 2.

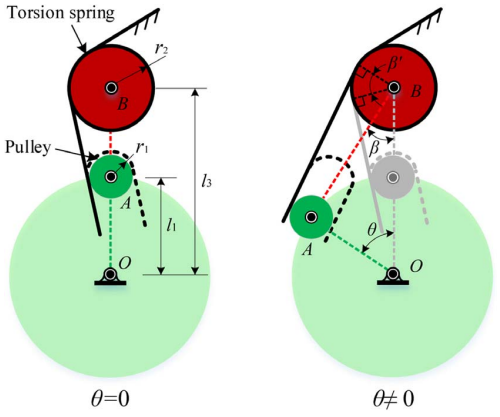

Fig. 12 Schematic design of a mechanism with Spring 3 mounted for generating negative stiffness behavior at $\theta=\pi/3$ rad. Dashed line connected to the leg of torsion spring shows the kinematic constraint of prismatic joint.

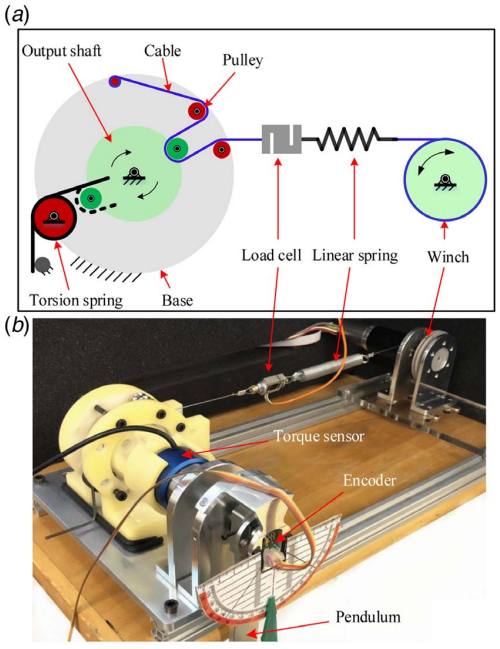

Fig. 13 (*a*) Schematic design of a constant torque mechanism and (*b*) test rig used for the constant torque mechanism

Table 2 Geometric parameters of the constant torque mechanism

Parameter	Description	Value (mm)
r_1	Radius of pulley	5
r_2	Radius of torsion spring	9.7
l_1	Length of crank OA	15
l_3	Length of base link OB	30

Table 3 Spring parameters

		Design parameters		Spring selected	
Spring	Type	Stiffness	Preload	Stiffness	Model
Spring 1	Linear spring	0.275 N/mm	5.35 N	0.28 N/mm	T081-120-500
Spring 3	Torsion spring	506 N/mm/rad	0	506.4 N/mm/rad	E02400312750S

Following the proposed method, a set of desired springs' parameters are found, which is summarized in Table 3, in which the specifications of commercial springs selected for testing are also listed.

The constant-torque design was validated experimentally. A prototype of the mechanism has been built and used for testing. Figure 13 shows the test rig setup. In the test rig, a Forsentek FSSM-200N force sensor is used to measure the tension of linear spring. A Forsentek FTE-20NM torque sensor is placed along the output shaft of the prototype to acquire the applied torque on the shaft. A pendulum is designed, and is connected to the torque sensor through the shaft. The rotations of the pendulum are measured using a RLS RMB20 encoder. An Arduino DUE board is used for acquiring the sensor data.

Quasi-static experiments were performed to acquire the torque–deflection characteristics of the mechanism prototype. Three cases for the experiments were considered. In Case-1 and Case-2, the linear spring (Spring 1) and the torsion spring (Spring 3) were used separately in the tests to acquire T_{AB} and T_B. In Case-3, both the linear and torsion springs were used to acquire T_E. For each testing, we applied torque on the output shaft of the prototype through offsetting the pendulum. The data of applied torque and deflection were acquired by sensors.

Figure 14 shows torque–deflection curves of the measurements for CCW rotation, along with simulation results. As can be seen in the plot, the simulations are in accordance with experimental results. Stiffness behaviors of the mechanism for different sets of condition can be observed clearly. An approximate constant torque interval with $T_E = 380 \pm 19$ N/mm can be found in the range of [0.54, 1.6] rad, which validates the mechanism design.

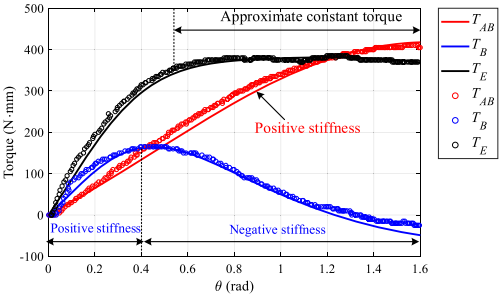

Fig. 14 Plot of torque versus deflection angle θ. The solid curves denote simulation results and the circles denote experiment results.

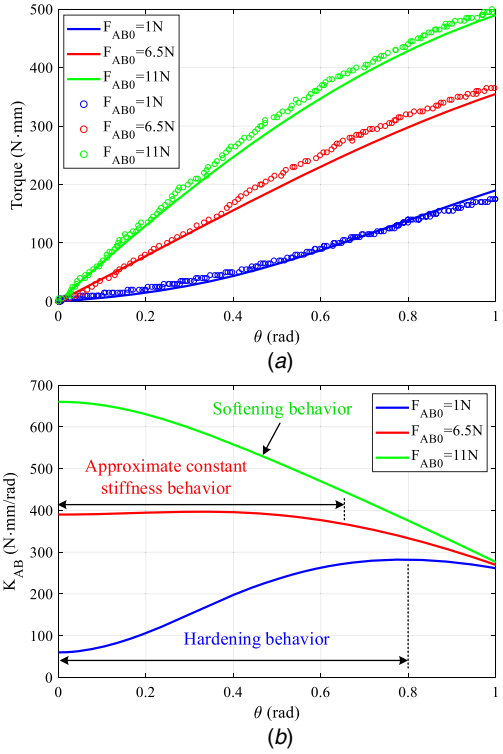

Fig. 15 (*a*) Plot of torque versus deflection angle θ for different pretensions F_{AB0}, wherein the solid curves denote simulation results and the circles denote experiment results. (*b*) Plot of stiffness K_{AB0} versus deflection angle θ for different pretensions F_{AB0}.

5 Construction of Variable Stiffness Mechanism With Multiple Modes

We include one more example of the constructing mechanism with desired stiffness behavior. Herein, the construction of a variable stiffness mechanism (VSM), which can achieve multiple stiffness behaviors including hardening behavior, softening behavior, and constant stiffness behavior, is described. VSMs can find their applications in constructing variable stiffness actuators and serial elastic actuators. Such a design that is able to adjust stiffness behavior is desirable for improving actuator performance in terms of collision safety, stability, and energy efficiency [13,31,32].

From Fig. 4, we can see that $\hat{K}_{AB,1}$ is equal to zero when $\theta = 0$ rad for any given λ with in the range of (0, 1). In other words, the mechanism stiffness at $\theta = 0$ rad is solely determined by $\hat{K}_{AB,2}$. Thus, variable stiffness can be achieved through changing spring preload F_{AB0}. We can also see from the figure that, in the range of $\theta \in \left[-\theta\,|_{d\hat{K}_{eq,1}/d\theta=0}, \theta\,|_{d\hat{K}_{eq,1}/d\theta=0}\right]$, $\hat{K}_{AB,1}$ and $\hat{K}_{AB,2}$ exhibit hardening behavior and softening behavior, respectively. Also, a constant stiffness behavior can be obtained by assigning appropriate values of k_{AB} and F_{AB0}, as shown in Fig. 5. Therefore, three stiffness behaviors including hardening behavior, softening behavior, and constant stiffness behavior can be achieved by using the mechanism with Spring 1. Such a mechanism is constructed as shown in Fig. 13(*a*).

The mechanism was tested for its variable stiffness performance. Case-1 where only the linear spring (Spring 1) is used in the mechanism was tested. Moreover, different spring preloads (F_{AB0}=1, 6.5, and 11 N) were set to assess the influences of F_{AB0} on stiffness performance. In the testing, external torque is applied on the output shaft through offsetting the pendulum.

The torque–deflection curves for different preloads are shown in Fig. 15(*a*). The simulation results in the figure match the measurements with a maximum error of about 25 N/mm. As depicted in Fig. 15(*b*), different stiffness behaviors, namely hardening, softening, and approximate constant stiffness behaviors, can be observed clearly. The mechanism for the condition with $F_{AB0}=1$ N shows first hardening behavior in the range of [0, 0.8] rad, and then transits to softening behavior as θ increases. The softening behavior becomes evident with increasing of spring preload F_{AB0}. The mechanism for the condition with $F_{AB0}=11$ N shows only softening behavior. An approximate constant stiffness behavior interval in the range of [0, 0.66] rad can be observed from the curve of $F_{AB0}=6.5$ N. Moreover, the joint stiffness at $\theta=0$ rad increases when the spring preload F_{AB0} increases, which is consistent with the analysis in Sec. 3.

The VSM designed is able to vary its stiffness with different behaviors including hardening, softening, and constant stiffness behaviors. These characteristics can find some potential applications in exoskeletons, service robots, and walking robots. Herein, an application of the mechanism in the wearable elbow exoskeleton is included.

Figure 16(*a*) shows an embodiment of VSM, in which three branches are arranged in a circular pattern using a cable wrapped on a number of pulleys to extend the range of stiffness variation of VSM. Each branch is constructed with a cable wrapped on three pulleys, as shown in Fig. 11. In the VSM, the spring pretension is adjusted through the pretension wheel connected with a worm gear. A prototype of the VSM was built as shown in Fig. 16(*b*).

Figure 17(*a*) shows a compliant actuator designed with the proposed VSM. The VSM is connected to a motor through a worm gear, which is used as a compliant coupling between the motor shaft and the output shaft, leading to the ability to reduce the peaks of force from hard impact. The prototype of the compliant actuator is shown in Fig. 17(*b*). The prototype has a compact size and light weight structure, and can be further used in the wearable elbow exoskeleton as shown in Fig. 17(*c*). The adoption of the compliant actuator in the exoskeleton can help to protect human and motor from hard impact, thus increase safety of the physical human–robot interaction.

6 Discussion and Conclusions

In the paper, a unified stiffness model is developed for stiffness analysis of a spring-loaded inverted slider crank mechanism. With the model, stiffness performance with the influences of all design parameters can be readily analyzed, thanks to the basic stiffness characteristics, namely $\hat{K}_{AB,1}$, $\hat{K}_{AB,2}$, $\hat{K}_{A,1}$, $\hat{K}_{A,2}$, $\hat{K}_{B,1}$, and $\hat{K}_{B,2}$. Multiple stiffness behaviors including hardening behavior, softening behavior, negative behavior, zero-stiffness behavior, bistable behavior, and irrational nonlinearity can be found in the mechanism.

Based on the results of stiffness analysis, mechanisms with desired stiffness behaviors can be synthesized. In this paper, a new constant-torque mechanism was constructed in a simple design. Moreover, a variable stiffness mechanism which can achieve three stiffness behaviors including hardening behavior, softening behavior, and constant stiffness behavior was constructed. Prototypes of the mechanisms were built to validate the designed stiffness behaviors.

The main contribution of this work is the comprehensive analysis of the stiffness performance of the spring-loaded inverted slider crank mechanism with a unified stiffness model. Stiffness characteristics of each individual spring were analyzed. The results can be employed in designing new mechanisms for desired stiffness behaviors.

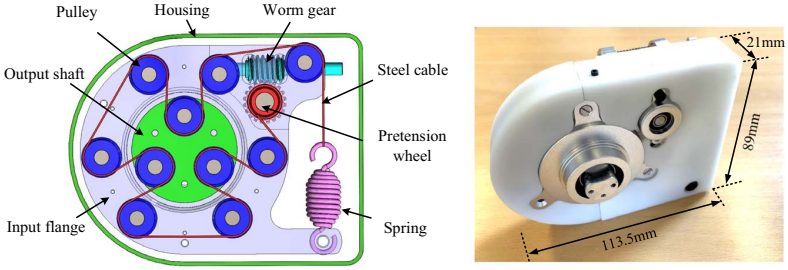

Fig. 16 An embodiment of VSM: (*a*) CAD model and (*b*) prototype

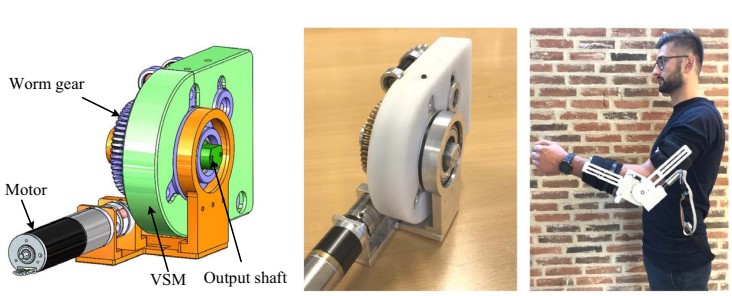

Fig. 17 (*a*) CAD model of the compliant actuator designed with the VSM, (*b*) the compliant actuator prototype, and (*c*) the wearable elbow exoskeleton mounted on the human arm

It is noted that some assumptions are applied for the force and stiffness analysis in this work. One is that the static equilibrium condition is assumed for the force analysis of the mechanism. This indicates that the analysis in the work is only valid for low speed and negligible link mass condition. Another assumption is that the joints of the mechanism are free of friction. Friction is indeed a factor that has to be considered in real constructions of mechanisms. In this work, pulleys embedded bearings are used for physical prototype constructions to reduce the influence of friction. With this effort, the mathematical model shows a good prediction to experimental results. However, a stiffness model with the factors of mass and friction will be helpful to improve the accuracy, which will be investigated in future work.

Compared with the mechanisms analyzed in this work, compliant mechanisms of monolithic structures can eliminate friction and backlash from relative motions between rigid links. However, as the monolithic compliant mechanisms highly rely on the material's elasticity to transfer movement, the stress and strain relationships of the material must be considered, which brings challenges to accurate stiffness modeling. The model and method proposed in this work provide flexibility in designing compliant mechanisms. Nonlinear stiffness analysis of such mechanisms with a unified stiffness model will be investigated in future work.

Acknowledgment

The research is partially supported by Innovation Fund Denmark through Grand Solutions project Exo-aider. The first author acknowledges the CSC scholarship for his study at Aalborg University, Denmark. The third and fourth authors acknowledge the support of National Natural Science Foundation of China (Grant nos. 51675018 and 61773042).

Appendix

$$c = \frac{1}{l_1 + l_2 - l_3} \cdot \left(2r_1 \arccos\left(\frac{2r_1 - 2l_1 \sin\theta}{\sqrt{16r_1^2 - 16l_1 l_1 \sin\theta + 4l_2^2}} \right) + 2r_1 \arccos\left(\frac{4r_1 + 2l_1 \sin\theta}{\sqrt{16r_1^2 + 16r_1 l_1 \sin\theta + 4l_2^2}} \right) - 2r_1 \arccos\left(\frac{2r_1}{\sqrt{4r_1^2 - 4r_1 l_1 \sin\theta + l_2^2}} \right) - 2r_1 \arccos\left(\frac{2r_1}{\sqrt{4r_1^2 + 4r_1 l_1 \sin\theta + 4l_2^2}} \right) + \sqrt{l_2^2 + 4r_1 l_1^2 \sin\theta} + \sqrt{l_2^2 - 4r_1 l_1^2 \sin\theta} + 2l_1 - 2l_3 \right) \tag{A1}$$

References

[1] Li, M., and Cheng, W., 2018, "Design and Experimental Validation of a Large-Displacement Constant-Force Mechanism," ASME J. Mech. Robot., **10**(5), p. 051007.
[2] Hou, C.-W., and Lan, C.-C., 2013, "Functional Joint Mechanisms With Constant-Torque Outputs," Mech. Mach. Theory, **62**, pp. 166–181.
[3] Prakashah, H. N., and Zhou, H., 2016, "Synthesis of Constant Torque Compliant Mechanisms," ASME J. Mech. Robot., **8**(6), p. 064503.
[4] Li, Z., and Bai, S., 2019, "A Novel Revolute Joint of Variable Stiffness With Reconfigurability," Mech. Mach. Theory, **133**, pp. 720–736.
[5] Awad, M. I., Hussain, I., Gan, D., Az-zu'bi, A., Stefanini, C., Khalaf, K., Zweiri, Y., Taha, T., Dias, J., and Seneviratne, L., 2018, "Passive Discrete Variable Stiffness Joint (pDVSJ-II): Modeling, Design, Characterization, and Testing Toward Passive Haptic Interface," ASME J. Mech. Robot., **11**(1), p. 011005.
[6] Xu, Q., 2016, "Design of a Large-Stroke Bistable Mechanism for the Application in Constant-Force Micropositioning Stage," ASME J. Mech. Robot., **9**(1), p. 011006.
[7] Hao, G., 2018, "A Framework of Designing Compliant Mechanisms With Nonlinear Stiffness Characteristics," Microsystem Technol., **24**(4), pp. 1795–1802.
[8] Zhou, L., and Bai, S., 2015, "A New Approach to Design of a Lightweight Anthropomorphic Arm for Service Applications," ASME J. Mech. Robot., **7**(3), p. 031001.
[9] Christensen, S., and Bai, S., 2018, "Kinematic Analysis and Design of a Novel Shoulder Exoskeleton Using a Double Parallelogram Linkage," ASME J. Mech. Robot., **10**(4), p. 041008.
[10] Shaw, A., Neild, S., and Wagg, D., 2013, "Dynamic Analysis of High Static Low Dynamic Stiffness Vibration Isolation Mounts," J. Sound Vib., **332**(6), pp. 1437–1455.
[11] Ibrahim, R., 2008, "Recent Advances in Nonlinear Passive Vibration Isolators," J. Sound Vib., **314**(3), pp. 371–452.
[12] Austin, J., Schepelmann, A., and Geyer, H., 2015, "Control and Evaluation of Series Elastic Actuators with Nonlinear Rubber Springs," IEEE/RSJ International Conference on Intelligent Robots and Systems, Hamburg, Germany, Sep. 28–Oct. 2, pp. 6563–6568.
[13] Park, J.-J., Lee, Y.-J., Song, J.-B., and Kim, H.-S., 2008, "Safe Joint Mechanism Based on Nonlinear Stiffness for Safe Human-Robot Collision," IEEE International Conference on Robotics and Automation, Pasadena, CA, May 19–23, pp. 2177–2182.
[14] Wu, T.-M., Wang, S.-Y., and Chen, D.-Z., 2011, "Design of An Exoskeleton for Strengthening the Upper Limb Muscle for Overextension Injury Prevention," Mech. Mach. Theory, **46**(12), pp. 1825–1839.
[15] Arakelian, V., and Ghazaryan, S., 2008, "Improvement of Balancing Accuracy of Robotic Systems: Application to Leg Orthosis for Rehabilitation Devices," Mech. Mach. Theory, **43**(5), pp. 565–575.
[16] Liu, Z., Niu, F., Gao, H., Yu, H., Ding, L., Li, N., and Deng, Z., 2018, "Design, Analysis, and Experimental Validation of An Active Constant-Force System Based on a Low-stiffness Mechanism," Mech. Mach. Theory, **130**, pp. 1–26.
[17] Jensen, B. D., and Howell, L. L., 2004, "Bistable Configurations of Compliant Mechanisms Modeled Using Four Links and Translational Joints," ASME J. Mech. Design, **126**(4), pp. 657–666.
[18] Sun, X., Xu, J., Wang, F., and Zhang, S., 2018, "A Novel Isolation Structure With Flexible Joints for Impact and Ultralow-frequency Excitations," Int. J. Mech. Sci., **146–147**, pp. 366–376.
[19] Pham, M. T., Yeo, S. H., Teo, T. J., Wang, P., and Nai, M. L. S., 2019, "Design and Optimization of a Three Degrees-of-Freedom Spatial Motion Compliant Parallel Mechanism With Fully Decoupled Motion Characteristics," ASME J. Mech. Robot., **11**(5), p. 051010.
[20] Pellegrini, S. P., Tolou, N., Schenk, M., and Herder, J. L., 2013, "Bistable Vibration Energy Harvesters: A Review," J. Intel. Mat. Syst. Str., **24**(11), pp. 1303–1312.
[21] dos Santos, W. M., Caurin, G. A., and Siqueira, A. A., 2017, "Design and Control of An Active Knee Orthosis Driven by a Rotary Series Elastic Actuator," Control Eng. Pract., **58**, pp. 307–318.
[22] Hao, G., Mullins, J., and Cronin, K., 2017, "Simplified Modelling and Development of a Bi-directionally Adjustable Constant-Force Compliant Gripper," Proc. IMechE. Part C: J. Mech. Eng. Sci., **231**(11), pp. 2110–2123.
[23] Yang, Z.-W., and Lan, C.-C., 2015, "An Adjustable Gravity-Balancing Mechanism Using Planar Extension and Compression Springs," Mech. Mach. Theory, **92**, pp. 314–329.
[24] Howell, L. L., and Midha, A., 1994, "A Method for the Design of Compliant Mechanisms With Small-Length Flexural Pivots," ASME. J. Mech. Design, **116**(1), pp. 280–290.
[25] Howell, L. L., and Midha, A., 1996, "Evaluation of Equivalent Spring Stiffness for Use in a Pseudo-Rigid-Body Model of Large-Deflection Compliant Mechanisms," ASME. J. Mech. Design, **118**(1), pp. 126–131.
[26] Li, Z., Chen, W., and Bai, S., 2019, "A Novel Reconfigurable Revolute Joint With Adjustable Stiffness," IEEE International Conference on Robotics and Automation, Montreal, QC, Canada, May 20–24, pp. 8388–8393.
[27] Bacek, T., Moltedo, M., Rodriguez-Guerrero, C., Geeroms, J., Vanderborght, B., and Lefeber, D., 2018, "Design and Evaluation of a Torque-Controllable Knee Joint Actuator With Adjustable Series Compliance and Parallel Elasticity," Mech. Mach. Theory, **130**, pp. 71–85.
[28] Han, N., and Cao, Q., 2016, "Global Bifurcations of a Rotating Pendulum With Irrational Nonlinearity," Commun. Nonlinear Sci. Numer. Simulat., **36**, pp. 431–445.
[29] Li, B., and Hao, G., 2018, "Nonlinear Behaviour Design Using the Kinematic Singularity of a General Type of Double-Slider Four-bar Linkage," Mech. Mach. Theory, **129**, pp. 106–130.
[30] Baker, M. S., and Howell, L. L., 2002, "On-Chip Actuation of An In-plane Compliant Bistable Micromechanism," J. Microelectromech. Syst., **11**(5), pp. 566–573.
[31] Wolf, S., Grioli, G., Eiberger, O., Friedl, W., Grebenstein, M., Höppner, H., Burdet, E., Caldwell, D. G., Carloni, R., Catalano, M. G., Lefeber, D., Stramigioli, S., Tsagarakis, N., Van Damme, M., Van Ham, R., Vanderborght, B., Visser, L. C., Bicchi, A., and Albu-Schaffer, A., 2016, "Variable Stiffness Actuators: Review on Design and Components," IEEE/ASME Trans. Mechatronics, **21**(5), pp. 2418–2430.
[32] Owaki, D., and Ishiguro, A., 2006, "Enhancing Stability of a Passive Dynamic Running Biped by Exploiting a Nonlinear Spring," IEEE/RSJ International Conference on Intelligent Robots and Systems, Beijing, China, Oct. 9–15, pp. 4923–4928.

Chapter 6

Paper III

Design, modeling and testing of a compact variable stiffness mechanism for exoskeletons

Zhongyi Li, Shaoping Bai, Ole Madsen, Weihai Chen, and Jianbin Zhang

The paper has been published in the
Mechanism and Machine Theory Vol. 151(2020), pp. 103905, 2020.

Mechanism and Machine Theory 151 (2020) 103905

Contents lists available at ScienceDirect

Mechanism and Machine Theory

journal homepage: www.elsevier.com/locate/mechmachtheory

Design, modeling and testing of a compact variable stiffness mechanism for exoskeletons

Zhongyi Li [a], Shaoping Bai [a,*], Ole Madsen [a], Weihai Chen [b], Jianbin Zhang [c]

[a] Department of Materials and Production, Aalborg University, Aalborg 9220, Denmark
[b] School of Automation Science and Electrical Engineering, Beihang University, Beijing 100191, China
[c] School of Mechanical Engineering and Automation, Beihang University, Beijing 100191, China

ARTICLE INFO

Article history:
Received 18 February 2020
Revised 27 March 2020
Accepted 7 April 2020

Keywords:
Variable stiffness mechanism
Reconfigurable design
VSM dynamics
Wearable exoskeleton

ABSTRACT

In this paper, the mechanical design of a novel variable stiffness mechanism (VSM) with reconfigurability is presented. The design of VSM is based on a zero-length base link four-bar linkage, integrated with a linear spring. The VSM is able to achieve variable stiffness in adjustable ranges, due to its reconfigurable design. Compared with other similar designs, the new VSM is compact and light weight, and can be used as a standalone module, or integrated with electric motor to build variable stiffness actuator which can be further applied in wearable exoskeletons. In the paper, mathematical models are developed for VSM to reveal the stiffness/torque performance limits. The mathematical models are validated experimentally with a prototype in both static and dynamic tests. The proposed VSM is finally integrated in a wearable elbow exoskeleton.

1. Introduction

Recent years have witnessed increasing interests in wearable exoskeletons. Compared with robots in industrial applications, exoskeletons are meant to work in synergy with humans, in which adaptability and safety are critical rather than motion precision and repeatability [1–6]. This led to the development of new actuation techniques represented by compliant actuators. A compliant actuator is able to absorb shocks and deal with unstructured environments for a safe and comfortable physical human-robot interaction (pHRI) [7–9]. Up to date, various compliant actuators have been proposed and exploited in robots. Among them, serial elastic actuator (SEA) and variable stiffness actuator are examples that were extensively studied.

The concept of SEA was first reported by Pratt and Williamson [10]. In their paper, an elastic element with constant stiffness was introduced in series between the motor gearbox and the actuator output, as shown in Fig. 1(a). This concept has been subsequently employed in different applications including hopping and walking robots [11–14], rehabilitation robots and assistive exoskeletons [15–19]. However, the SEA owns only constant stiffness, which limits its dynamic performance in the tradeoff between system bandwidth and torque resolution.

To overcome the limitations of SEA, efforts have been made to develop variable stiffness actuators, or VSA in short. Based on the motor setup for actuator positioning and stiffness variation, VSAs can be classified into two groups, namely, *actuator with antagonistic motors* and *actuator with independent motors* [20]. In the first group, two or more motors working in an antagonistic manner are connected in parallel to control joint position and stiffness simultaneously [21–23]. In [21,22],

* Corresponding author.
E-mail address: shb@mp.aau.dk (S. Bai).

https://doi.org/10.1016/j.mechmachtheory.2020.103905
0094-114X/

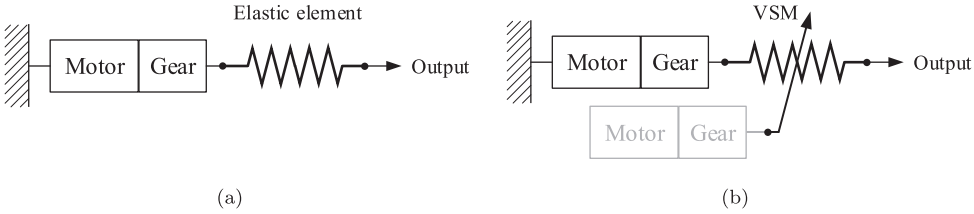

Fig. 1. Configurations of (a) SEA and (b) VSA.

VSAs in this group were used to actuate the joints of elbow exoskeletons through Bowden cables. In these exoskeletons, the actuation systems can be mounted away from the joints, which leads to low weight and compact design of exoskeleton joints. However, as two motors are required to actuate each single joint, the actuation system is heavy, which is still a concern in the application of wearable devices. Moreover, antagonistic systems also require a nonlinear spring to enable the simultaneous mechanical stiffness and position control. This greatly contributes to the mechanical complexity of such systems.

For the VSA in the second group, a typical configuration can be described in Fig. 1(b). The VSA in this group can achieve adjustable compliance through a variable stiffness mechanism (VSM) which connects to a position motor in series. The adjustment of stiffness can be done automatically or manually. In stiffness adjustment, three working principles can be adopted: (1) varying transmission ratio between output and spring, (2) adjusting the physical properties of the spring, and (3) changing the spring preload. Some noticeable VSAs include AwAS [24], vsaUT [25], SVSA-II [26], PLVL-VSA [27] which are based on the principle of (1), and MeRIA [28], VSJ [29] which are based on the principle of (2), and MACCEPA [31] based on the principle of (3). The adjustable stiffness of VSAs brings benefits to exoskeletons where a natural and safe pHRI is required. In [5], VSA was used in a lower limb wearable ankle robot, namely VS-AnkleExo, to reduce interaction forces and improve joint tracking performance. In [8], a MeRIA-based knee joint was tested for the rehabilitation training purpose, showing benefits of VSA in pursuing a good tradeoff between system bandwidth and stability. In [30], a VSA, namely ARES, was incorporated into the ATLAS exoskeleton joint to achieve a reduction of energy consumption in actuation and a better adaptability to disturbances. In the above-mentioned exoskeletons, VSAs were designed with two independent-setup motors, one for position and the other for stiffness. With such VSAs, the position and stiffness of the exoskeletons' joints can be controlled simultaneously. However, having two-motor setup increases the weight and complexity of VSAs, which brings limitations to achieve light-weight and portable exoskeletons.

Some other designs are noticeable. MACCEPA adjusts its stiffness by changing the preload of a spring [31]. The simple structure of MACCEPA allows the device to fit in the wearable exoskeletons where their size and weight are very limited [1,32–35]. Actuators or mechanisms based on spring preload principle can also be found in Liu et al. [36], Wu and Lan [37], Li et al. [38]. However, for a spring preload based VSA, its stiffness can only be adjusted in a fixed range, which highly depends on the spring properties. A method to adjust the stiffness variation range without changing mechanical components is desirable for wide applications.

In this paper, a novel design of variable stiffness mechanism with reconfigurability is proposed. The VSM is able to achieve variable stiffness in adjustable ranges, due to its reconfigurable design. The new VSM features a compact and light weight structure, and can be used as a standalone module, or integrated with electric motor to build VSA. Compared with our previous work done by Li and Bai [39], the work in paper has the following contributions: (1) a detailed mechanical design of the VSM, (2) mathematical modeling to reveal performance limits of VSM, (3) static and dynamic tests on the VSM prototype, and (4) a wearable elbow exoskeleton designed with the novel VSM.

The paper is organized as follows. In Section 2, variable stiffness principle and mechanical design of VSM are presented. Stiffness modeling of VSM is developed in Section 3, followed by the analysis of performance limits. The dynamics of the VSM is analyzed in Section 4. In Section 5, a prototype of VSM and its test rig are described, with which both static and dynamic experiments are conducted to evaluate the performances of VSM. Section 6 illustrates the application of the proposed VSM in a wearable elbow exoskeleton. Section 7 concludes this work.

2. Mechanical design of VSM

2.1. Basic concept of stiffness variation

The variable stiffness concept of the proposed VSM was introduced in Li and Bai [39]. Herein, the concept is reviewed briefly for completeness. The mechanism is essentially based on a special case of four-bar linkage, as shown in Fig. 2(a). In the linkage, bar-1 and 3 are mounted to the base via a pin joint at point A. A compliant coupler, bar-2, having a stiffness k, connects bar-1 and bar-3 with pin joints at points B and C respectively. The deflection between bar-1 and bar-3, due to elasticity of the compliant coupler, is noted by θ. The tension force within the compliant coupler is noted by F. External

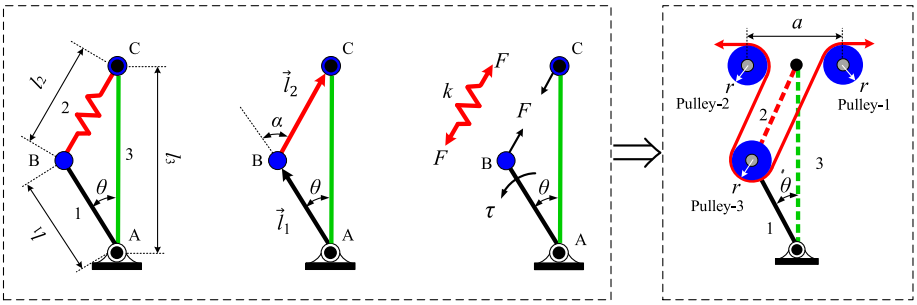

Fig. 2. Concept of constructing a variable stiffness mechanism. (a) A special case of four-bar linkage. (b) Implementation of mechanism with pulleys and cable.

joint torque to balance the torque induced by F is noted by τ. According to the virtual work principle, we can obtain

$$\tau = \left|\hat{l}_2 \times \vec{l}_1\right| \cdot F = J \cdot F \tag{1}$$

with

$$J = \left|\hat{l}_2 \times \vec{l}_1\right| = \frac{\left|\vec{l}_2 \times \vec{l}_1\right|}{l_2} = l_1 \sin\alpha = \frac{l_1 l_3 \sin\theta}{l_2} = \frac{l_1 l_3 \sin\theta}{\sqrt{l_1^2 + l_3^2 - 2 l_1 l_3 \cos\theta}} \tag{2}$$

where l_1, l_2 and l_3 represent the lengths of bar-1, 2 and 3, and $\hat{l}_2$ represents the unit vector parallel to $\vec{l}_2$. According to Hooke's law, the tension force F can be described as

$$F = k \cdot (l_2 - l_{2,0}) + F_0 = k \cdot \delta l_2 + F_0 \tag{3}$$

where $l_{2,0}$ represents the length of bar-2 when $\theta = 0$, and F_0 is the spring pretension.

The joint stiffness is obtained by differentiating Eq. (1) with relation to θ, which is given by

$$K = \underbrace{\left(J^2 + \frac{\partial J}{\partial \theta}\delta l_2\right)}_{K_1} \cdot k + \underbrace{\frac{\partial J}{\partial \theta} \cdot F_0}_{K_2} = c_1 \cdot k + c_2 \cdot F_0 \tag{4}$$

where two terms, K_1 and K_2, represent the influences induced by the stiffness k and the pretension F_0 respectively. In Eq. (4), c_1 and c_2 are related only to the geometry of the mechanism, and change nonlinearly with respect to joint deflection θ.

2.2. Mechanical design of VSM

The linkage shown in Fig. 2(a) can be practically implemented by using pulleys and cable, as shown in Fig. 2(b). Based on the concept, a new design of VSM was proposed as shown in Fig. 3. The VSM consists of two coaxial shafts, output shaft and input shaft. Two flanges, output flange and input flange, are separately designed on the output and input shafts. A number of pulleys are mounted on the two flanges. A steel cable wrapping around the pulleys is used to couple the motion from the input to the output. One end of the steel cable is connected to a tension spring of stiffness k. The other end is reeled by a pretension wheel which is connected to a worm gear to adjust manually pretension of the spring. Noting that, in the design, the housing of VSM is mounted on the input flange, which moves with the input shaft. Moreover, the tension spring is not the only choice of elastic element. Other elastic elements including compression springs and rubber springs [38,40] are also available in the design of VSM.

The designed VSM is reconfigurable by wrapping the steel cable with different patterns, as shown in Fig. 4. We can see from Fig. 4 that the number of branches in the VSM is changed with respect to patterns of cable wrapping. Herein, the number of branches is noted by N, representing the configuration parameter of VSM.

Compared with other VSMs, the new design introduces some new features as follows

1. The proposed VSM is reconfigurable, and three configurations can be achieved.
2. The VSM is designed as a standalone module, which allows the VSM to be easily integrated with existing systems for various applications.
3. The VSM allows to change spring of different stiffness, which makes the VSM flexible for fitting different application requirements by choosing appropriate spring.

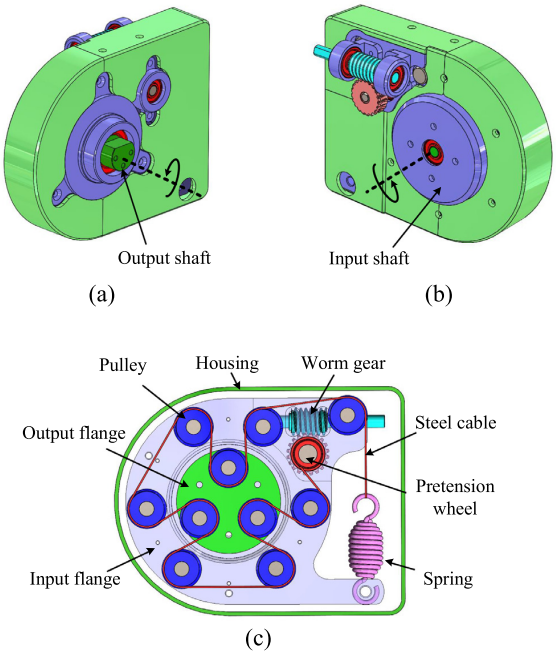

Fig. 3. CAD model of VSM. (a) Front view, (b) back view and (c) internal view of VSM.

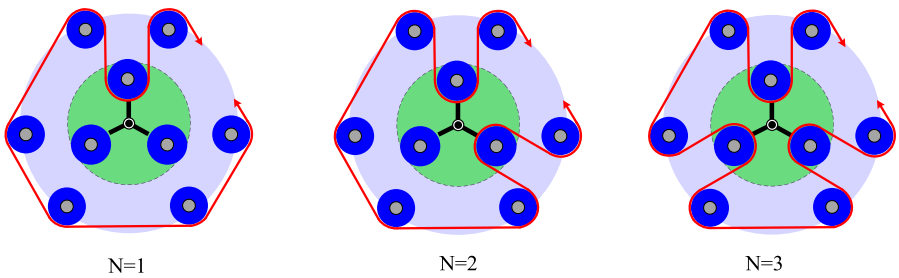

Fig. 4. Reconfigurations of VSM.

3. Analysis of VSM

3.1. Stiffness modeling

As shown in Fig. 3, the designed VSM takes a form of three branches, each being constructed with steel cable wrapped on three pulleys, two on input flange and the other one on output flange. The geometry of one branch is shown in Fig. 2(b). In the figure, the radius of pulley is noted by r, and the distance between the axes of pulley-1 and 2 is $a \approx 4r$. Referring to Eq. (1), the static model of VSM is given by

$$\tau = J_1 \cdot F = J_1 k \delta l + J_1 F_0 \tag{5}$$

where δl represents the elongation of spring, and J_1 is the Jacobian of the mechanism, which is a scalar in this case. From the geometry of VSM shown in Fig. 3, following equations are found

$$\delta l = cN\delta l_2 \tag{6}$$

and

$$J_1 = cNJ \tag{7}$$

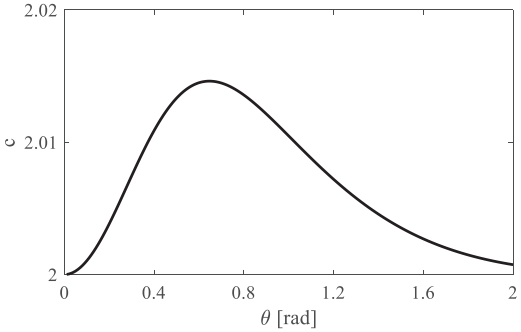

Fig. 5. Plot of c as a function of θ.

Table 1
Geometric parameters of VSM.

Parameter	Description	Value [mm]
r	Radius of pulley	6.6
d	Diameter of steel cable	0.8
a	Distance between pulley-1 and 2	26.5
l_1	Length of bar-1	13.5
l_3	Length of bar-3	30

where c is a factor describing the influences of geometry of mechanical parts on the cable elongation, and also the mechanical advantage J_1 as well. The detailed expression of c can be found in Appendix A. Fig. 5 shows changes of c with respect to θ, in which the geometric parameters are given in Table 1.

The tension force F of cable in the VSM is given by

$$F = cNk\delta l_2 + F_0 \tag{8}$$

According to Eq. (5), the stiffness model of VSM can be obtained as:

$$K = N^2 \cdot \underbrace{\left(c^2 J^2 + c^2 \frac{\partial J}{\partial \theta}\delta l_2 + c\frac{\partial c}{\partial \theta} J \delta l_2\right)}_{\hat{K}_1} \cdot k + N \cdot \underbrace{c\frac{\partial J}{\partial \theta}}_{\hat{K}_2} \cdot F_0 \tag{9}$$

where expressions of $\frac{\partial c}{\partial \theta}$ and $\frac{\partial J}{\partial \theta}$ are included in Appendix A.

From Eq. (9), we can see that the stiffness of VSM changes with respect to configuration parameter N, stiffness k and spring pretension F_0. Moreover, the stiffness changes nonlinearly due to joint-dependent Jacobian and its derivative, as well as the geometry of mechanical parts.

3.2. Stiffness simulations of VSM

Based on Eqs. (5) and (9), simulations were conducted in Matlab to reveal the performance limits of the designed VSM. In simulations, geometric parameters of VSM are given in Table 1. Such geometric parameters allow the VSM to be designed in a compact form. The steel cable can withstand the maximum tension of 460 N without failure.

The stiffness of spring plays a key role in determining the performance of the proposed VSM. Eq. (9) implies that the spring stiffness k influences the overall stiffness K by scaling $\hat{K}_1$, while the pretension F_0 influences K by scaling $\hat{K}_2$. Fig. 6 shows changes of $\hat{K}_1$ and $\hat{K}_2$ with respect to θ. We can see that $\hat{K}_1$ and $\hat{K}_2$ exhibit totally different stiffness behavior. Fig. 7(a) shows changes of K with variations of spring stiffness k, where the stiffness performance of $\hat{K}_1$ becomes evident with increasing of spring stiffness k. Moreover, for any given $\theta \neq 0$ in the range of [0, 1.2] rad, the joint stiffness K increases as k increases. Fig. 7(b) shows the corresponding torque curves for different spring stiffness k. We can see that for any given $\theta \neq 0$, a larger k will yield a larger τ. For all the curves shown in Figs. 6 and 7, the values of geometric parameters are given in Table 1.

To look into the influences of stiffness k, we take two linear extension springs (model: MiSUMi AWFM12-40 and SODEMANN 32450) for simulations and tests. The properties of the springs can be found in Table 2. Due to the physical limitations of the designed VSM, the selected springs need to satisfy

$$\begin{cases} l_{\max} \leq 66 \text{ mm} \\ D_e \leq 21 \text{ mm} \\ F_{\max} \leq 460 \text{ N} \end{cases} \tag{10}$$

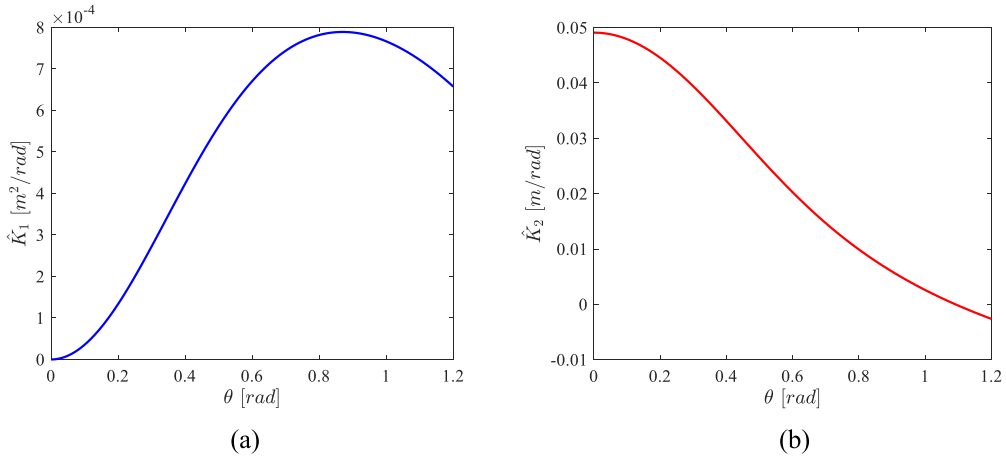

Fig. 6. Stiffness performances of (a) $\hat{K}_1$ and (b) $\hat{K}_2$.

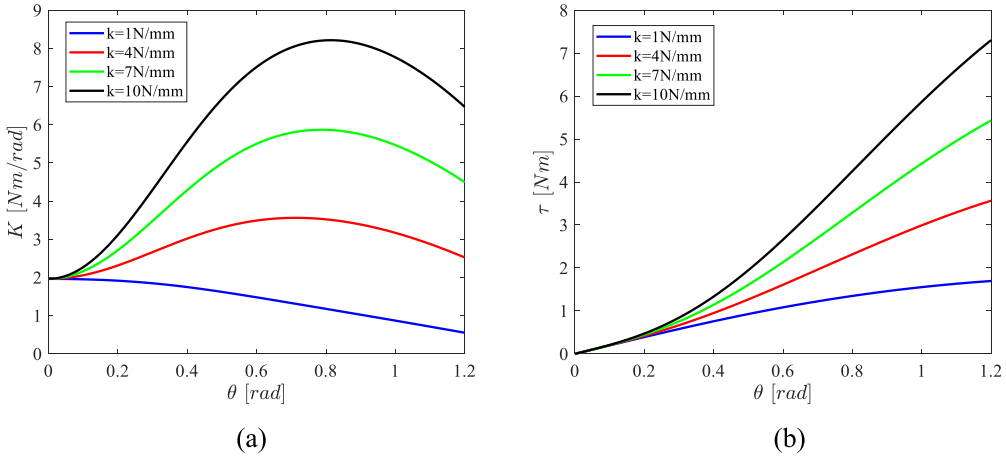

Fig. 7. (a) Stiffness curves and (b) torque curves for different spring stiffnesses k with $F_0 = 40$ N, $N = 1$.

Table 2
Specifications of the springs.

Parameter	Specification	Value		Unit
		Spring-1	Spring-2	
l_f	Free length	40	41.2	mm
$l_{\max}$	Maximum loaded length	59.2	56	mm
$F_{\max.spring}$	Maximum load	101.29	198	N
$F_{0.spring}$	Initial load*	14.71	29.28	N
D_e	Exterior diameter	12	15	mm
k_s	Stiffness	4.5	11.4	N/mm

*: preload applied to a tension spring when fabricated.

It is also noted that, as the proposed VSM is essentially a mechanism with cable transmission, the elasticity of cable used should be included in the mathematical models. Herein, the elasticity is approximately calculated as follows

$$k_c = \frac{EA}{l_c} \tag{11}$$

where $E = 1.9 \times 10^5$ N/mm^2 is elastic modulus of steel cable, and $A = 0.503$ mm^2 is cross-sectional area of cable, and l_c is cable length. l_c depends on the configuration of VSM. Based on data in Table 1, l_c is obtained as

$$l_c = \begin{cases} 224.4 \text{ mm}, & N = 1 \\ 298.8 \text{ mm}, & N = 2 \\ 373.2 \text{ mm}, & N = 3 \end{cases} \tag{12}$$

Considering the elasticity of steel cable k_c, and the stiffness of the linear spring k_s, the total stiffness k in Eqs. (5) and (9) can be found by

$$k = \frac{k_s \cdot k_c}{k_s + k_c} \tag{13}$$

Specifically, k is obtained as

$$\text{Spring-1}: k = \begin{cases} 4.45 \text{ N/mm}, & N = 1 \\ 4.44 \text{ N/mm}, & N = 2 \\ 4.42 \text{ N/mm}, & N = 3 \end{cases}, \quad \text{Spring-2}: k = \begin{cases} 11.1 \text{ N/mm}, & N = 1 \\ 11 \text{ N/mm}, & N = 2 \\ 10.91 \text{ N/mm}, & N = 3 \end{cases} \tag{14}$$

According to Eqs. (5) and (9), the output torque and stiffness of the designed VSM are nonlinear functions of deflection angle θ. The following specifications are considered when studying the performance limits of a nonlinear VSM,

- Initial stiffness K_0, i.e., the stiffness value when $\theta = 0$.
- Stiffness range $K \in [K_{\min}, K_{\max}]$.
- Maximum allowable torque $\tau_{\max}$.
- Maximum deflection $\theta_{\max}$.

Fig. 8 shows the torque-deflection characteristics of VSM for different configurations under the influence of spring pretension F_0. In the figure, the dash line indicates the minimum pretension that has to be applied to the VSM to overcome the initial tension $F_{0,\text{spring}}$ of the selected spring, which is given in Table 2. The white solid curves represent the maximum tension that the spring can withstand $F_{\max}$, which is given by

$$F_{max} = cNk\delta l_2 + F_0 = F_{max,spring} \tag{15}$$

In Fig. 8, we can see that, for any given configuration N, a larger F_0 will yield a smaller range of deflection θ, if the external torque is fixed. The maximum deflections $\theta_{\max}$ for both $N = 1$ and $N = 3$ are found at the points where $F = 101.29$ N and $F_0 = 14.71$ N, which are shown clearly in the figure. The maximum allowable torques $\tau_{\max}$ for both $N = 1$ and $N = 3$ are noted in Fig. 8(a) and (c), and they are found at the points where $F_0 = 14.71$ N and $\theta = \theta_{\max}$. Moreover, $\tau_{\max}$ changes significantly with respect to configuration N. $\tau_{\max}$ increases from 2.84 Nm for $N = 1$ to 6.59 Nm for $N = 3$. Fig. 8(b) and (d) show the curves of τ for $N = 1$ and $N = 3$ respectively, in which different pretensions are applied on the spring.

Fig. 9 shows the stiffness of VSM for varying spring pretensions, joint deflections and configurations. In Fig. 9(a) and (c), the lower and upper tension limits are represented by dash lines and white solid lines respectively. The black solid line $\frac{dK}{d\theta} = 0$ separates whole area into two, namely, the hardening behavior area and the softening behavior area. Joint stiffness hardening means an increase in the stiffness, while softening is the opposite. In Fig. 9(a) and (b), as θ increases, the stiffness K for any given spring pretension F_0 monotonically increases before $\frac{dK}{d\theta} = 0$ and then decreases after $\frac{dK}{d\theta} = 0$. The maximum stiffness $K_{\max}$ of the VSM for $N = 1$ is at the point where $F_0 = 101.29$ N and $\theta = 0$, and the minimum stiffness $K_{\min}$ is at the point where $F_0 = 14.71$ N and $\theta = 0$, which are given in Fig. 9(a). In Fig. 9(c) and (d), only hardening behaviors can be observed. Thus, for any given spring pretension, K increases as θ increases. The maximum stiffness of $K_{\max}$ for $N = 3$ is at the point where $F_0 = 14.71$ N and $\theta = \theta_{\max}$. From Fig. 9, it is seen that the VSM is able to achieve variable stiffness in a wide range changing from $K_{\min} = 0.72$ Nm/rad to $K_{\max} = 26.91$ Nm/rad thanks to its reconfigurable design.

Fig. 10 shows the torque-deflection characteristics of VSM for Spring-2. It is noted that both the maximum load $F_{\max}$ and stiffness k_s of Spring-2 are much larger than that of Spring-1, as shown in Table 2. As a consequence, the maximum allowable torque $\tau_{\max}$ of VSM with Spring-2 is larger than the one with Spring-1 for any given configuration N, which can be observed clearly in Fig. 10. The maximum allowable torque $\tau_{\max}$ for Spring-2 can reach to 11.69 Nm when $N = 3$, while the one shown in Fig. 8(c) is 6.59 Nm. Noting that, in the Fig. 10(a) and (c), $\tau_{\max}$ is determined through the lower and upper tension limits represented by the dash lines and the white solid lines respectively. For any given configuration N, $\tau_{\max}$ is found at the point where $F_0 = 29.28$ N and $\theta = \theta_{\max}$. $\theta_{\max}$ is the maximum deflection of VSM, which is found at the point where $F = 198$ N and $F_0 = 29.28$ N for any given N in Fig. 10(a) and (c). Fig. 10(b) and (d) show the changes of τ for $N = 1$ and $N = 3$ under the influences of F_0. In the figures, the actual torque-deflection curves are shown clearly.

Fig. 11 shows the stiffness-deflection characteristics of VSM for Spring-2. In Fig. 11(a) and (c), the dash lines and the white solid lines represent the lower and upper tension limits respectively. The black solid curve shown in Fig. 11(a) represents $\frac{dK}{d\theta} = 0$, which separates the entire plot into two sub-areas, one showing hardening behavior and the other showing softening behavior. As shown in Fig. 11(c), the mechanism for $N = 3$ only exhibits hardening behavior in the range of motion. The stiffness characteristics can be observed clearly from the curves in Fig. 11(b) and (d). The maximum stiffness $K_{\max}$ and the minimum stiffness $K_{\min}$ for any given configuration N are noted clearly in Fig. 11(a) and (c). We can see that the

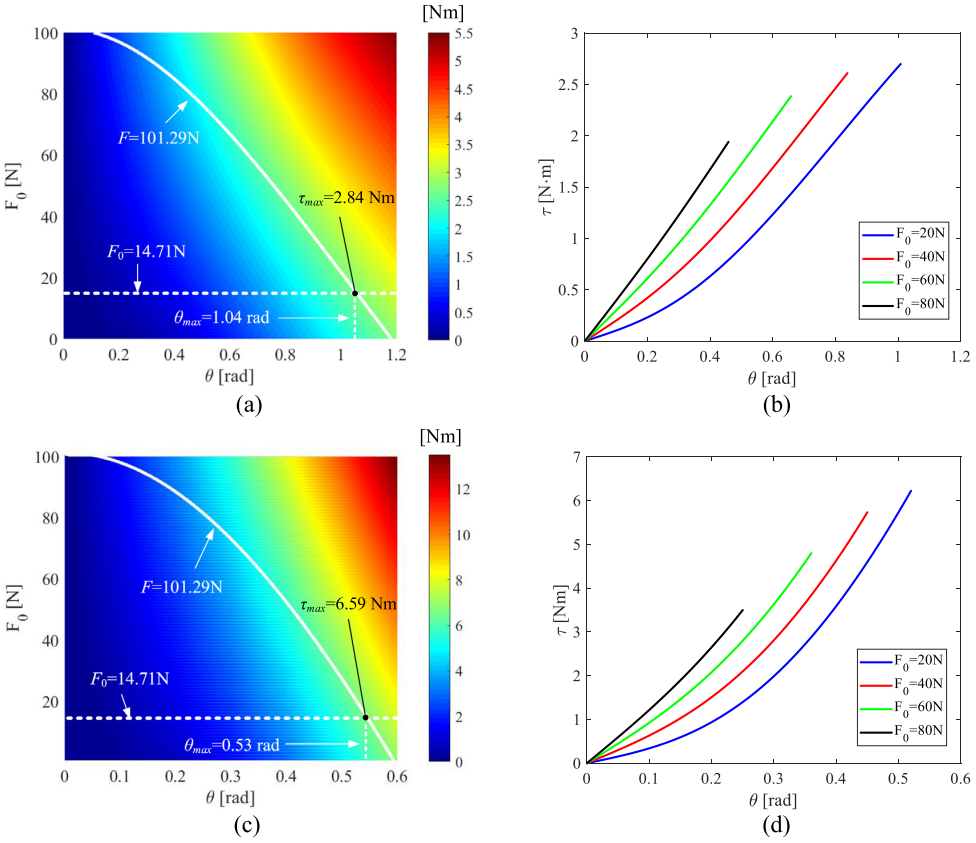

Fig. 8. VSM output-torque τ as a function of N, F_0 and θ with Spring-1, (a) overall variations of τ with $N = 1$ and $k = 4.45$ N/mm, (b) variations of τ with F_0 =20, 40, 60, 80N, $N = 1$ and $k = 4.45$ N/mm, (c) overall variations of τ with $N = 3$ and $k = 4.42$ N/mm, (d) variations of τ with $F_0 = 20$, 40, 60, 80N, $N = 3$ and $k = 4.42$ N/mm.

Table 3
Performance of the proposed VSM.

Spring.	N	$\tau_{\max}$ [Nm]	$K_{\min}$ [Nm/rad]	$K_{\max}$ [Nm/rad]	K_0 [Nm/rad]	$\theta_{\max}$ [rad]
Spring-1	1	2.84	0.72	4.97	[0.72, 4.97]	1.04
	2	5.01	1.44	14.41	[1.46, 9.92]	0.67
	3	6.59	2.17	26.91	[2.17, 14.87]	0.53
Spring-2	1	5.26	1.44	9.74	[1.44, 9.74]	0.89
	2	9.01	2.87	31.37	[2.87, 19.41]	0.59
	3	11.69	4.31	56.13	[4.31, 29.15]	0.47

VSM with Spring-2 is able to vary stiffness in a wider range of [1.44, 56.13] Nm/rad than the one of the VSM with Spring-1, which is in the range of [0.72, 26.91] Nm/rad.

According to Eq. (9), the initial stiffness K_0 of VSM is only determined by its second term K_2 due to $K_1 = 0$ when $\theta = 0$. Thus, K_0 is a function of F_0 and N. As F_0 and N increases, the initial stiffness K_0 increases linearly. In Figs. 9 and 11, the values of K_0 when $F_0 = F_{0,spring}$ and $F_0 = F_{\max}$ are shown clearly.

Based on the simulations, the torque/stiffness/deflection space of the proposed VSM for both Spring-1 and Spring-2 are summarized in Table 3, where the performance limits of VSMs for $N = 2$ are also included.

It is noted that the selected springs also bring limitation to the energy storage capability of VSM. For the VSM, the energy storage capability follows

$$U = \frac{1}{2}k\left(l_{\max} - \left(l_f + \frac{F_0 - F_{0,\text{spring}}}{k}\right)\right)^2 \tag{16}$$

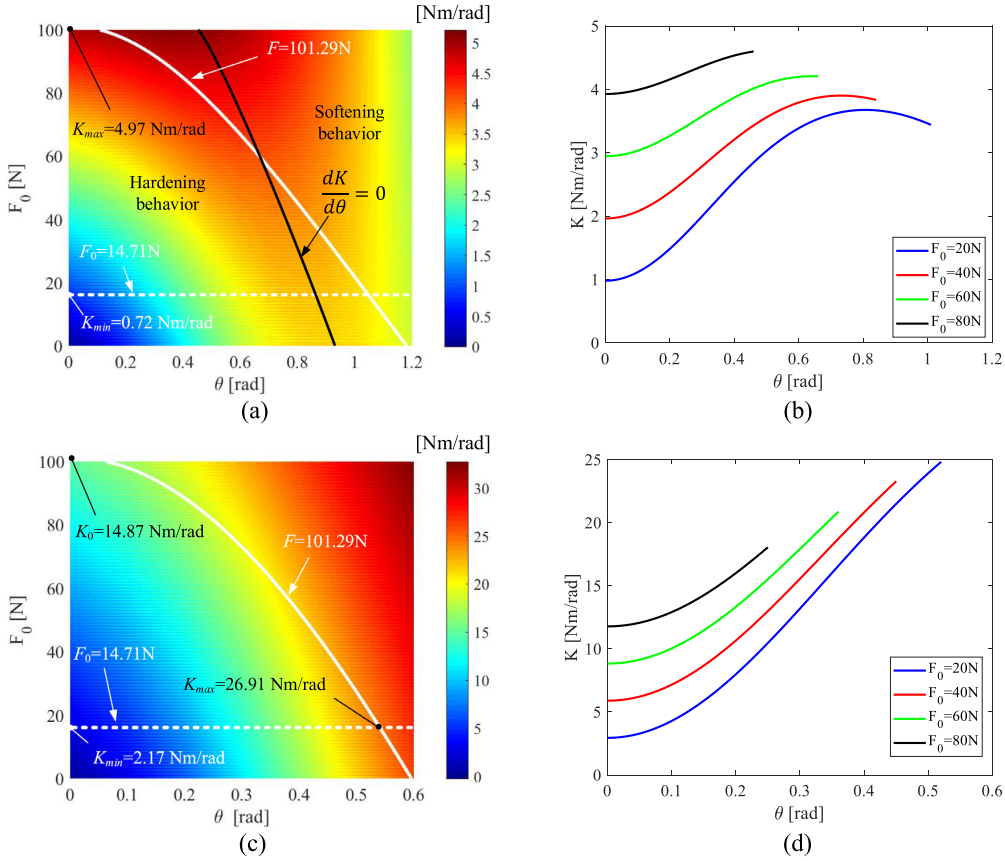

Fig. 9. Stiffness K as a function of N, F_0 and θ with Spring-1, (a) overall variations of K with $N = 1$ and $k = 4.45$ N/mm, (b) variations of K with $F_0 = 20$, 40, 60, 80 N, $N = 1$ and $k = 4.45$ N/mm, (c) overall variations of K with $N = 3$ and $k = 4.42$ N/mm, (d) variations of K with F_0 =20, 40, 60, 80N, $N = 3$ and $k = 4.45$ N/mm.

which is a function of pretension F_0 and spring stiffness k. Eq. (16) implies that the potential energy stored in the spring due to the spring pretension cannot be used to store energy from VSM output.

4. Dynamics analysis

4.1. Dynamic modeling

Fig. 12 shows the schematic of a VSA where the proposed VSM is used as a compliant coupling between motor drive and output link (pendulum). The dynamic equation of the system is expressed as

$$I_p\ddot{\theta}_p + (B_p + B_{vsm})\dot{\theta}_p + T_{c,p}\text{sign}(\dot{\theta}_p) + m_p g l_p \sin(\theta_p) = \tau(\theta) \tag{17}$$

$$(I_m + \beta I_g + \beta I_{vsm})\ddot{\theta}_m + (B_m + \beta B_{vsm})\dot{\theta}_m + n\beta T_{c,g}\text{sign}(\dot{\theta}_m) + \beta\tau(\theta) = T_m \tag{18}$$

with

$$\theta = \theta_g - \theta_p = \frac{\theta_m}{n} - \theta_p;\ \ \beta = \frac{1}{n^2\eta_g} \tag{19}$$

where all parameters in Eqs. (17)–(19) are described in Table 4 in combining with properties derived from a real construction of test rig shown in Fig. 15. In Eqs. (17) and (18), the Coulomb friction is modeled as a constant torque with speed dependent direction, which can be obtained experimentally [41].

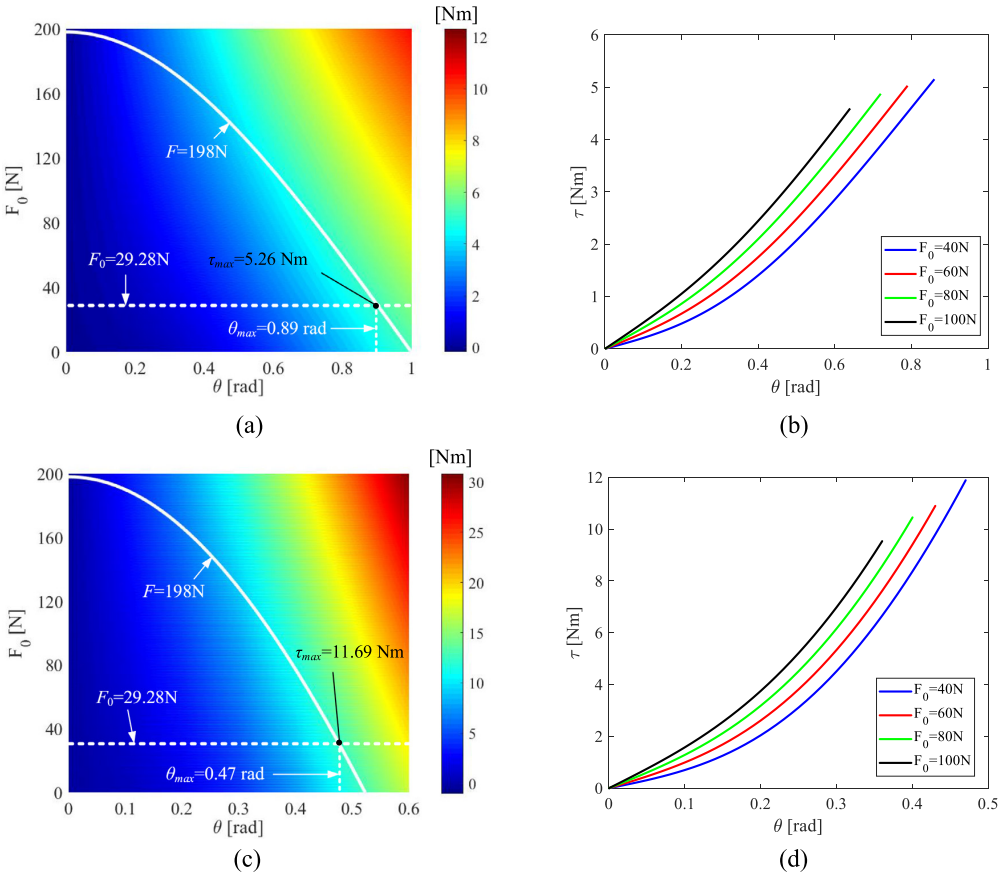

Fig. 10. VSM output-torque τ as a function of N, F_0 and θ with Spring-2, (a) overall variations of τ with $N = 1$ and $k = 11.1$ N/mm, (b) variations of τ with $F_0 = 40$, 60, 80, 100 N, $N = 1$ and $k = 11.1$ N/mm, (c) overall variations of τ with $N = 3$ and $k = 10.9$ N/mm, (d) variations of τ with $F_0 = 40$, 60, 80, 100 N, $N = 3$ and $k = 10.9$ N/mm.

Table 4
Descriptions of dynamic parameters.

Parameter	Description	Value
I_p	inertia of the pendulum	0.001784 kgm^2
I_m	inertia of the motor	1.1×10^{-7} kgm^2
I_g	inertia of the gearbox	6×10^{-8} kgm^2
I_{vsm}	inertia of the VSM	3×10^{-5} kgm^2
B_p	viscous damping coefficient of the pendulum	–
B_m	viscous damping coefficient of the motor	3.96×10^{-6} Nms/rad
B_{vsm}	viscous damping coefficient of the VSM	(refer to Table 5)
$T_{c,p}$	torque due to Coulomb friction at the pendulum shaft	0.005 Nm
$T_{c,g}$	torque due to Coulomb friction at the gearbox output shaft	–
m_p	mass of the pendulum	0.08043 kg
T_m	output torque of the motor	–
$\tau(\theta)$	load torque of the VSM	–
l_p	distance between the center of mass and the rotation axis of pendulum	0.06226 m
θ	joint deflection of the VSM	–
θ_p, θ_m, θ_g	rotations of the pendulum, motor and gearbox	–
n	gear ratio of the gearbox	1:63
η_g	gearbox efficiency	70 %

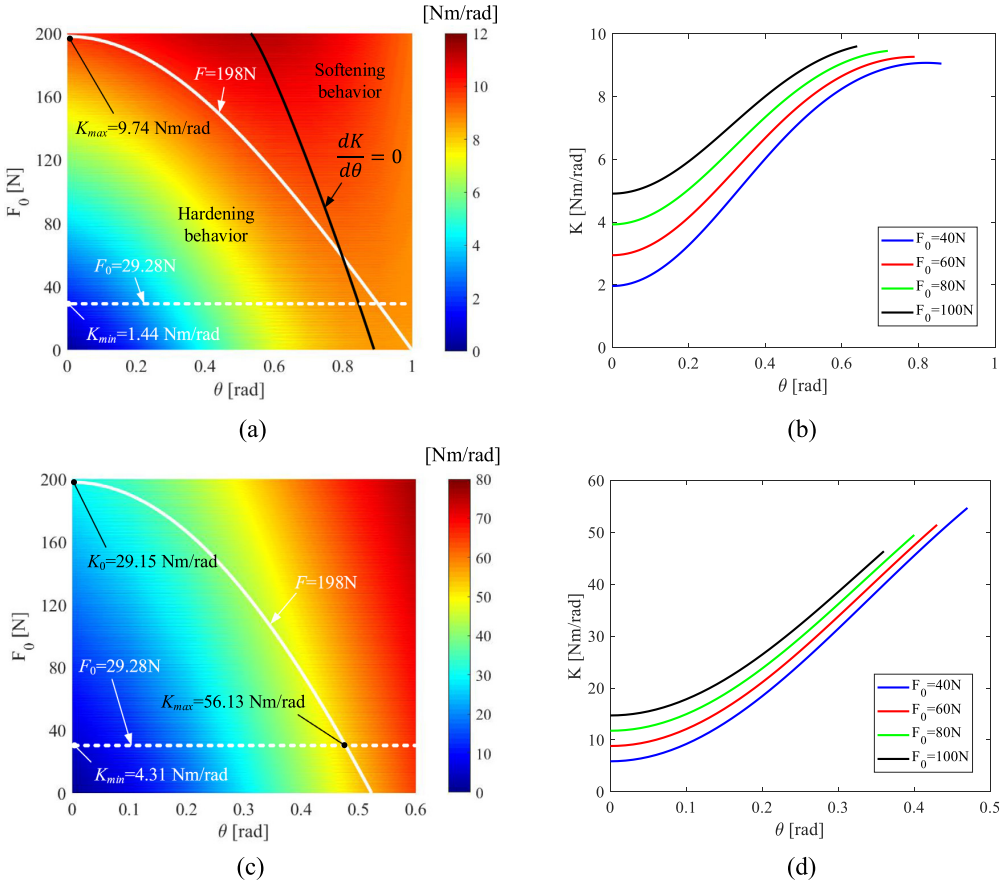

Fig. 11. VSM output-torque K as a function of N, F_0 and θ with Spring-2, (a) overall variations of K with $N = 1$ and $k = 11.1$ N/mm, (b) variations of K with $F_0 = 40$, 60, 80, 100N, $N = 1$ and $k = 11.1$ N/mm, (c) overall variations of K with $N = 3$ and $k = 10.9$ N/mm, (d) variations of K with $F_0 = 40$, 60, 80, 100N, $N = 3$ and $k = 10.9$ N/mm.

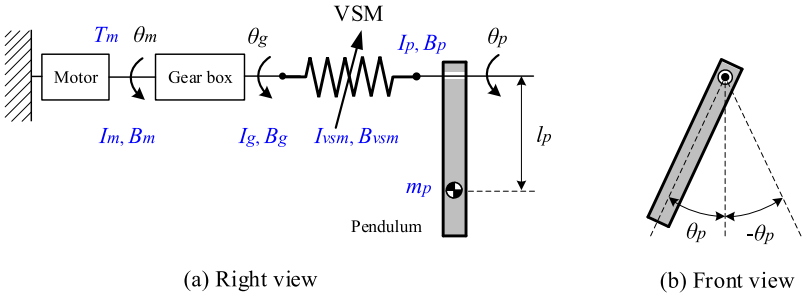

Fig. 12. Schematic diagram for simulation in which a motor is connected in series to the proposed VSM.

Eq. (17) denotes the dynamics of the subsystem of link side, while Eq. (18) represents the dynamics of the subsystem of motor side. Combining both equations, we can obtain the dynamics of the entire system as

$$T_m = (I_m + \beta I_g + \beta I_{vsm})\ddot{\theta}_m + (B_m + \beta B_{vsm})\dot{\theta}_m + n\beta T_{c,g}\text{sign}(\dot{\theta}_m) + \beta\left(I_p\ddot{\theta}_p + (B_p + B_{vsm})\dot{\theta}_p + T_{c,p}\text{sign}(\dot{\theta}_p) + m_p g l_p \sin(\theta_p)\right) \quad (20)$$

So far, we have derived the system dynamics, and we now further analyze the frequency response.

In Eq. (17), the load torque $\tau(\theta)$ is a nonlinear function of θ, as described in Eq. (5). For any angle of θ, $\tau(\theta)$ can be linearized as

$$\tau = k_l(\theta - \theta^*) + \tau^* \tag{21}$$

where θ^* is a working point that is close to θ, and τ^* is the corresponding spring torque. To investigate the frequency response, we simplify the problem by setting the working point at θ^*=0, for which

$$k_l = \frac{2Nl_1l_3F_0}{l_3 - l_1} \tag{22}$$

which is the VSM stiffness induced by the pretension F_0 at $\theta = 0$.

The dynamics of the entire system Eq. (20) is discontinuous due to the Coulomb frictions. For the sake of simplicity, the Coulomb friction terms were neglected in simulations [41]. By this way, the dynamics of the entire system can be rewritten as

$$(I_m + \beta I_g + \beta I_{vsm})\ddot{\theta}_m + (B_m + \beta B_{vsm})\dot{\theta}_m + \beta\left(I_p\ddot{\theta}_p + (B_p + B_{vsm})\dot{\theta}_p + m_pgl_p\theta_p\right) = T_m \tag{23}$$

With Eqs. (17) and (19), Eq. (23) can be rewritten as a function of θ_p, which is

$$A\theta_p^{(4)} + B\theta_p^{(3)} + C\ddot{\theta}_p + D\dot{\theta}_p + E\theta_p = T_m \tag{24}$$

with

$$\begin{cases} A = nk_l^{-1}I_p(I_m + \beta I_g + \beta I_{vsm}) \\ B = nk_l^{-1}(B_p + B_{vsm})(I_m + \beta I_g + \beta I_{vsm}) + nk_l^{-1}I_p(B_m + \beta B_{vsm}) \\ C = nk_l^{-1}(I_m + \beta I_g + \beta I_{vsm})(m_pgl_p + k_l) + \beta I_p \\ D = nk_l^{-1}m_pgl_p(B_m + \beta B_{vsm}) + n(B_m + \beta B_{vsm}) \\ E = \beta m_pgl_p \end{cases} \tag{25}$$

Similarly, the dynamics of the subsystem of link side, Eq. (17), can be simplified as

$$I_p\ddot{\theta}_p + (B_p + B_{vsm})\dot{\theta}_p + m_pgl_p\theta_p = k_l\theta \tag{26}$$

Replacing θ in Eq. (26) by Eq. (19), the equation of motion is rewritten as

$$k_l\theta_m = I_pn\ddot{\theta}_p + (B_p + B_{vsm})n\dot{\theta}_p + (m_pgl_p + k_l)n\theta_p \tag{27}$$

Transforming this equation to the frequency domain, a transfer function is found as

$$G(j\omega) = \frac{\Theta_p(j\omega)}{\Theta_m(j\omega)} = \frac{k_l}{nI_p(j\omega)^2 + n(B_p + B_{vsm})j\omega + nm_pgl_p + nk_l} \tag{28}$$

Considering the damping effect, the damped natural frequency of the link side subsystem is found as [42]

$$f_{n,p} = \frac{1}{2\pi}\omega_{n,p}\sqrt{1 - \zeta_p^2} \tag{29}$$

with

$$\omega_{n,p} = \sqrt{\frac{m_pgl_p + k_l}{I_p}};\ \ \zeta_p = \frac{B_p + B_{vsm}}{2\sqrt{I_p(m_pgl_p + k_l)}} \tag{30}$$

Due to the fact that $B_p + B_{vsm}$ is very small, we can calculate directly the natural frequency,

$$f_{n,p} = \frac{1}{2\pi}\sqrt{\frac{m_pgl_p + k_l}{I_p}} \tag{31}$$

The natural frequency of the system is a function of the linear component of the mechanism stiffness k_l, inertia I_p and mass m_p. According to Eq. (22), k_l can be adjusted through changing the pretension F_0 and configuration N of VSM. It is noted that, due to the nonlinear stiffness characteristics of the VSM, the natural frequency of the system varies also with θ. The influence of the nonlinear stiffness characteristics on the natural frequency will be analyzed in the simulation with MATLAB/SimMechanics.

4.2. Simulation analysis

The SolidWorks model of system shown in Fig. 15 was imported into SimMechanics. In the simulation model, Eq. (5) was used to generate the load torque caused by VSM. To evaluate the natural frequency of the system, the input shaft of VSM was fixed, and simulations on the dynamic response of VSM were conducted in the form of free vibration. In the simulation, the pendulum was released from different initial positions ($\theta_p = \theta = 0.1,\ 0.2,\ 0.3,\ 0.4$ rad). The dynamic responses of the system in the frequency domain are shown in Fig. 13. We can see from the figure, the natural frequency increases with the increase of joint deflection of VSM. This is caused by the hardening behavior of VSM, where the joint stiffness increases as deflection θ increases. The natural frequency calculated from Eq. (31) is 7.97 Hz, which closely matches the simulated one at $\theta = 0.1$ rad. Eq. (31) defines the lowest limit of resonant frequency of system for any given parameters of N and F_0.

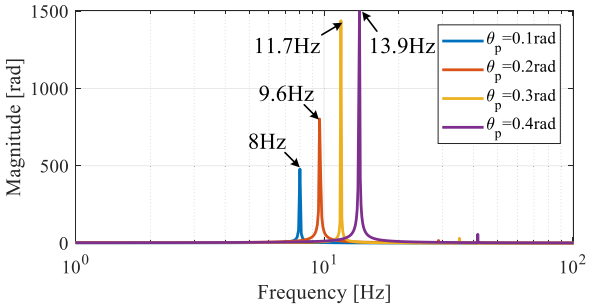

Fig. 13. Frequency responses of VSM for different pendulum positions with $k = 10.91$ N/mm, $N = 3$, and $F_0 = 30$ N.

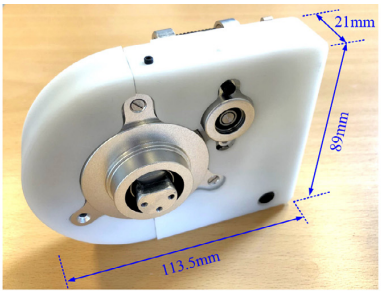

(a)

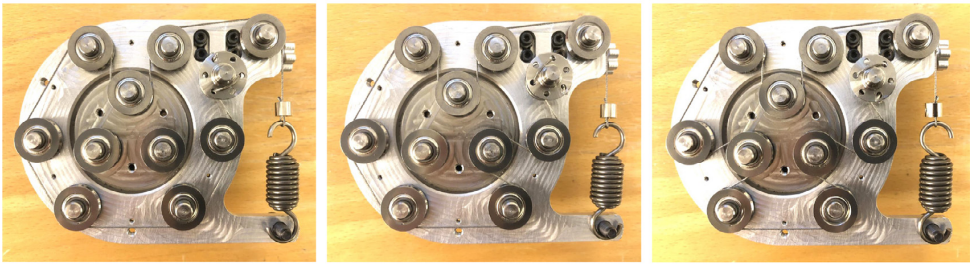

(b)

Fig. 14. (a) A VSM prototype, and (b) internal pictures of the prototype with different configurations.

5. Experiments

5.1. Prototyping and test rig setup

A prototype of the VSM has been built at Aalborg University, Denmark, as shown in Fig. 14. The size of the prototype is 113.5 × 89 × 21 mm (length × height × width), and the weight is about 0.214 kg including the spring. The geometric parameters are given in Table 1. Two linear extension springs which are given in Table 2 are separately used for tests.

Fig. 15 shows the test rig setup. In the test rig, the input shaft of VSM prototype is connected to a Maxon EC-max motor (40 W) through a Koaxdrive KD 32 gearbox (gear ratio: 1:63). A Forsentek FSSM-200N force sensor is used to measure the spring tension with an accuracy of 0.2N. A Forsentek FTE-20NM torque sensor is placed on the output shaft of the VSM prototype to measure the applied torque with an accuracy of 0.04 Nm. A pendulum is designed to facilitate applying torque on the output shaft of VSM, and is connected to the shaft through torque sensor. The rotations of the pendulum are acquired using a RLS RMB20 encoder with an accuracy of 0.5°. The sensor data are acquired with Arduino DUE board.

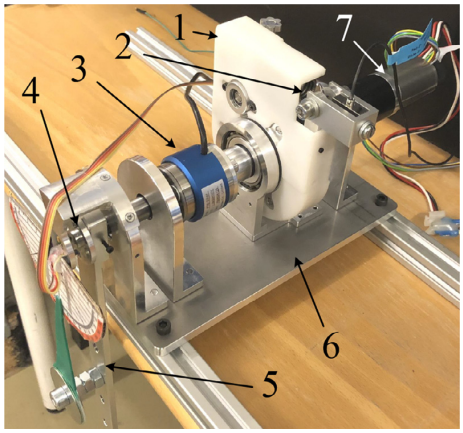

Fig. 15. Test rig used for experiments, which was constructed with (1) VSM prototype, (2) load cell, (3) torque sensor, (4) absolute encoder, (5) pendulum, (6) base, (7) motor and gearbox.

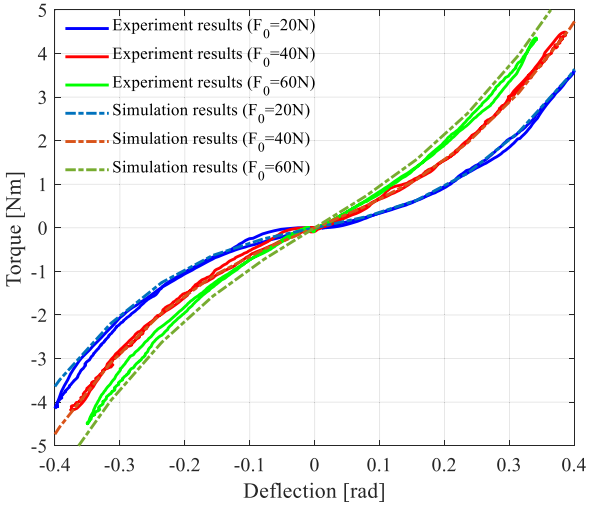

Fig. 16. Plot of torque v.s. deflection angle for varying pretension with $N = 3$ and $k = 4.42$ N/mm.

5.2. Static characterization

Quasi-static experiments were performed on the test rig to acquire the torque-deflection characteristic of VSM. In the experiments, the input shaft of VSM was fixed, and torque was applied on the output shaft of VSM through offsetting the pendulum, the value being measured by the torque sensor.

5.2.1. Torque-deflection characteristics for varying pretension F_0

Three different spring pretensions, namely $F_0 = 20$ N, 40 N and 60 N, were applied to the VSM with $N = 3$ and $k = 4.42$ N/mm. Fig. 16 shows the torque-deflection curves of the measurements, along with the simulation results. As can be seen, the simulation results are in accordance with experimental results with maximum absolute error 0.43 Nm, or maximum 10.8% of relative error, showing an accurate mathematical model we developed. The relative error e_p is calculated from

$$e_p = \frac{e_a}{\tau_{max}} \times 100\% \tag{32}$$

where e_a denotes the absolute error, and $\tau_{\max}$ is the maximum measured torque.

As the pretension increases, the joint stiffness increases, as shown clearly from the experimental torque-deflection relationships. Also, the nonlinear torque-deflection characteristics with hardening behavior can be observed, which is consistent

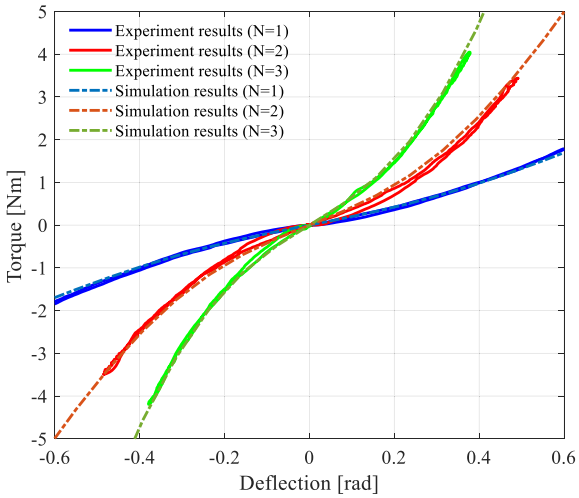

Fig. 17. Plot of torque v.s. deflection angle for varying configuration with $F_0 = 40$ N and $k = 4.42$ N/mm.

with the simulations in Section 3. The experiment results shown in Fig. 16 were measured for both loading and unloading phases. Due to the system hysteresis, the torques measured in loading phases for a given deflection are slightly higher than the ones in unloading phases. The maximum hysteresis is 9% of measurements between loading and unloading phases. The hysteresis is obtained from

$$e_h = \frac{\max\left(\tau_d(\theta) - \tau_{ud}(\theta)\right)}{\tau_{\max}} \times 100\% \tag{33}$$

where $\tau_d(\theta)$ and $\tau_{ud}(\theta)$ denote the torque values for any given θ in loading and unloading phases respectively.

5.2.2. Torque-deflection characteristics for different configurations N

Fig. 17 shows the torque-deflection curves for different configurations, in which $F_0 = 40$ N was set, and Spring-1 was used. It can be seen that the measured results closely match the simulated ones. The maximum absolute error is about 0.32 Nm, which is about 9.2% of relative error. Hysteresis for measured results is observed in Fig. 17. The maximum hysteresis is 8.8%. Moreover, the three torque-deflection relationships are very different to each other. This indicates that the proposed VSM is able to vary its stiffness in a wide range through changing configuration.

5.2.3. Torque-deflection characteristics for different springs

As the VSM can be rebuilt with different springs which affects performance of VSM, we tested the performance with two springs given in Table 2. During the experiment, $F_0 = 60$ N and $N = 3$ were set. The torque-deflection curves for different springs are shown in Fig. 18. From the figure, it is seen that the measurements agree well with simulation results, with maximum absolute error of 1.2 Nm or 14.6% relative error, which is mainly caused by machining errors and nonlinearity of steel cable [27,35,39]. The hysteresis is also observed in Fig. 18, showing the difference of measured torque between loading and unloading phases. The maximum hysteresis is 3%, which occurs in the condition of $k = 10.9$ N/mm, $F_0 = 60$ N and $N = 3$. Fig. 19 shows the torque-deflection curves for different cable pretensions $F_0 = 60,\ 120$ N with $k = 10.9$ N/mm and $N = 3$. We can see that the measured results match the simulated ones well. The maximum hysteresis for $F_0 = 120$ N is 16%, which is larger than the one for $F_0 = 60$ N.

5.3. Dynamic characterization

5.3.1. Resonant frequency of VSM

Experiment in the form of free vibration was conducted to investigate the dynamic performance of the VSM. Our main interest is the resonant frequency of the mechanism, which is essential for the motion control development. In the experiment, the input shaft of VSM was fixed, and the pendulum shown in Fig. 15 was released from different positions ($\theta_p = \theta = 0.1,\ 0.2,\ 0.3,\ 0.4$ rad). The absolute encoder was employed to record the position. The recorded positions were processed by conducting Fast Fourier Transform (FFT) in MATLAB R2017b. The resonant frequencies measured are shown in Fig. 20. The measured frequency changes from 4.5 Hz to 15.8 Hz, showing the influence of VSM stiffness on the dynamic performance of system. Fig. 20 also shows the comparison between the measured and simulated results. We can see that the measurements meet nearly to the simulated ones obtained from MATLAB/SimMechanics as presented in Section 4. Due to

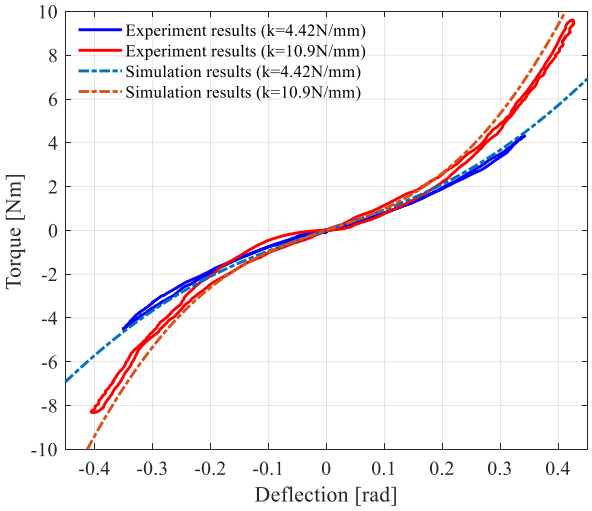

Fig. 18. Plot of torque v.s. deflection angle for different springs with $N = 3$ and $F_0 = 60$ N.

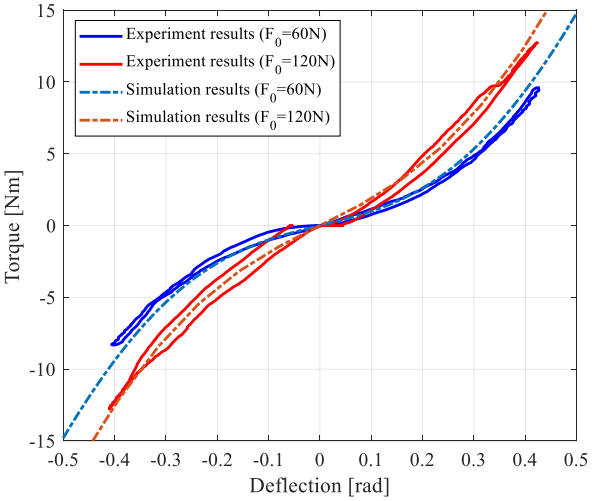

Fig. 19. Plot of torque v.s. deflection angle for varying pretension with $N = 3$ and $k = 10.9$ N/mm.

the hardening behavior of VSM, the measured frequency increases as released position θ_p increases, which is in accordance with the simulation results.

Moreover, with the free vibration experiment, we can obtain the damping coefficient of system. Regarding the construction of test rig, B_p shown in Eq. (17) is much smaller than B_{vsm}. Thus, B_p can be neglected in the dynamics. The Coulomb friction of the pendulum shaft is included in the simulation, of which the value is given in Table 4. To fit the measured results and identify the damping coefficient, a nonlinear grey-box model built in Matlab R2017b, namely, *idnlgrey* was used. The estimated results are shown in Fig. 21. As can be seen, the estimated friction coefficient B_{vsm} varies in the range of [0.001, 0.0697] Nms/rad, depending on the spring pretensions F_0 and configurations N. The variation is mainly caused by the friction between cable and pulley. It is noted that, in the proposed VSM, pulleys with embedded bearings are used to reduce the influence of the friction. From the estimated results, B_{vsm} is found very small, even if the use of pulleys increases the friction of VSM. For sake of simplicity in dynamics, the RMS values of the B_{vsm} for different configurations are used, and they are given in Table 5. Fig. 22 illustrates the time histories of free vibrations for the conditions of $N = 1$ and $F_0 = 50$ N, and $N = 3$ and $F_0 = 50$ N. It can be seen that the experimental results are generally in accordance with the simulated ones, showing that the estimated and actual friction coefficients are well matched to each other. Some deviations are noticeable

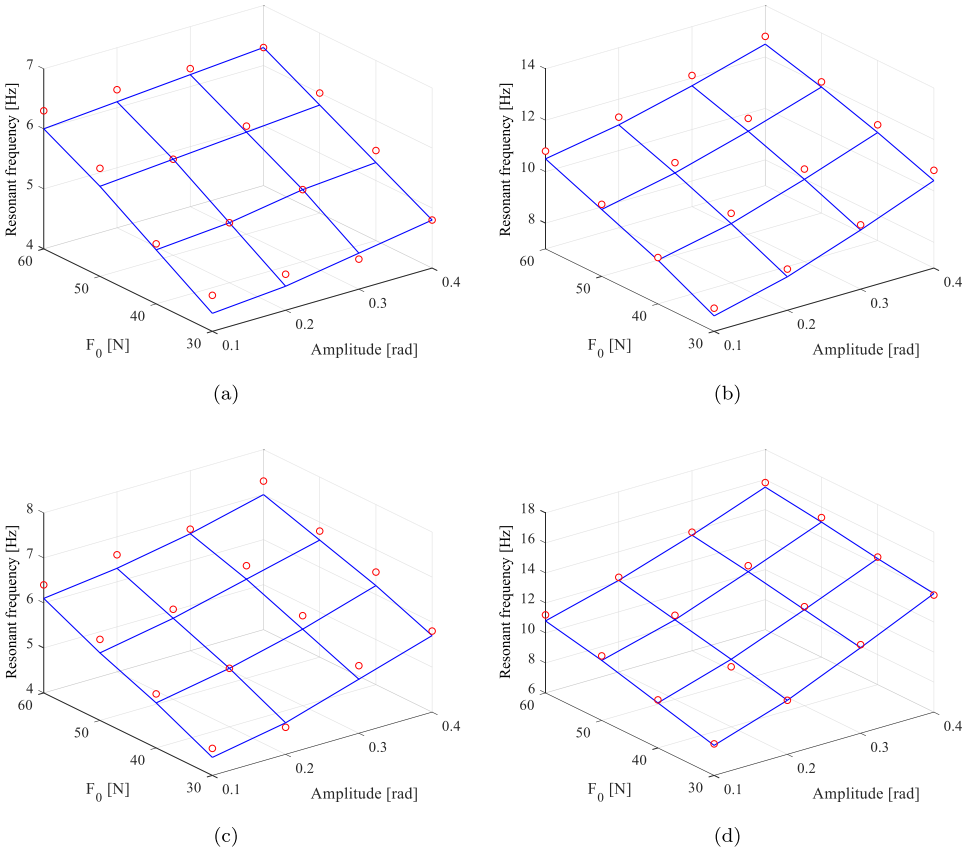

Fig. 20. The variations of resonant frequency for varying spring pretension F_0 and released position θ_p in following four different conditions, (a) $N = 1$ and $k = 4.45$ N/mm, (b) $N = 3$ and $k = 4.42$ N/mm, (c) $N = 1$ and $k = 11.1$ N/mm, and (d) $N = 3$ and $k = 10.91$ N/mm. In the figures, the red dots are measurements, while the blue grid surfaces are simulated resonant frequency distributions. (For interpretation of the references to color in this figure legend, the reader is referred to the web version of this article.)

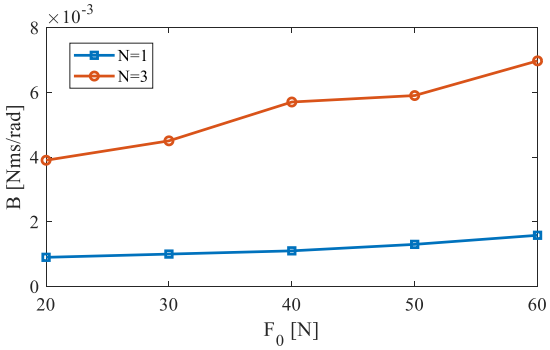

Fig. 21. Estimated results of viscous friction coefficient B_{vsm} for varying spring pretension F_0 and configuration N.

Table 5
Estimated results of B_{vsm}.

Parameter	Estimated value (RMS)		Unit
	$N = 1$	$N = 3$	
B	0.0012	0.0055	Nms/rad

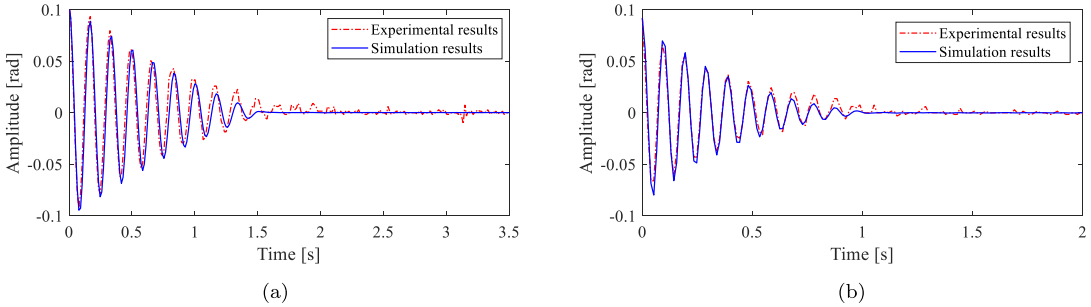

Fig. 22. Time history of free vibrations in the conditions of (a) $N = 1$, $F_0 = 50$ N and $k = 4.45$ N/mm, and (b) $N = 3$, $F_0 = 50$ N and $k = 4.42$ N/mm.

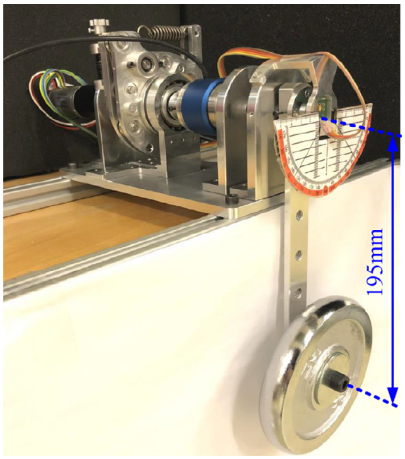

Fig. 23. Experimental setup for dynamic response, in which a 1.1 kg payload is mounted on the end of the pendulum.

at the end of vibration, which is likely due to the nonlinearity of the system and also the noise in measurement. As a matter of fact, the reading should be close to zero at the end, but due to noise, slight reading changes are observed in the results.

5.3.2. Dynamic response

Preliminary experiments were conducted to test dynamic response of system under different VSM stiffnesses. Fig. 23 shows the experimental setup. To acquire a high load torque in the experiment, a 1.1 kg mass is attached at the end of the pendulum, where the distance between the mass center and pendulum rotation axis is 195 mm. In the experiments, the motor was commanded to follow a sinusoidal position trajectory with the control diagram shown in Fig. 24. The reference position for the motor is described as

$$\theta_{m,ref} = A_{ref} \cdot \sin\left(2\pi f_{ref} t\right) \tag{34}$$

where A_{ref} =0.5 rad and f_{ref} =0.5 Hz are the amplitude and frequency of the sinusoidal trajectory respectively, and t is time.

Fig. 25 shows two experimental results of the system response to the sinusoidal motor position trajectory. Due to the compliance from the VSM, the system outputs θ_p does not follow exactly the motor rotation trajectory. As can be seen from the figure, θ_p is closer to θ_m with a higher pretension of VSM in which a larger stiffness is obtained.

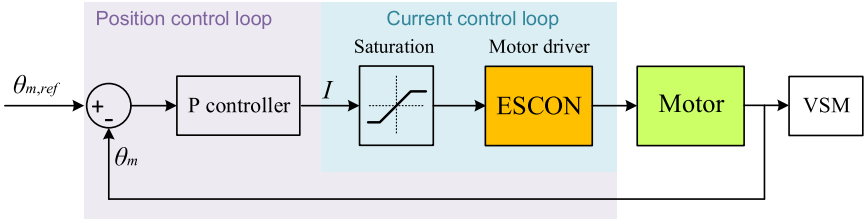

Fig. 24. Schematic diagram of the motor control, where ESCON is a servo controller for Maxon motor.

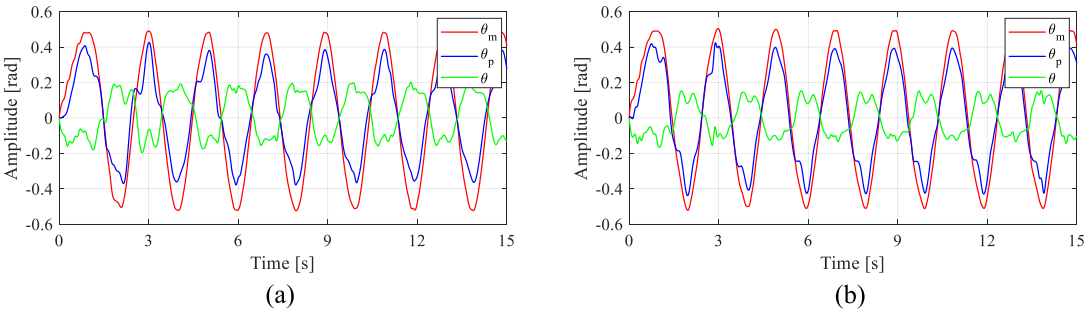

Fig. 25. Dynamic responses of system under different conditions, (a) $F_0 = 20$ N, $k = 4.42$ N/mm, $N = 3$, and (b) $F_0 = 60$ N, $k = 4.42$ N/mm, $N = 3$.

Table 6
Specifications of the elbow exoskeleton.

Specification	Value	Unit
Maximum output torque	11.69	Nm
Range of stiffness	[4.31, 56.13]	Nm/rad
Range of motion	[0, 145]	deg
Weight	0.94	kg

6. A wearable elbow exoskeleton

The new VSM is a passive compliant rotary joint which can be used as a standalone module or integrated with electric motors to construct compliant actuators. Fig. 26 shows the 3D model of a compliant actuator designed with the new VSM. In the model, a Maxon EC-4pole motor (90 W) in combination with a GP 22 HP gearbox (gear ratio: 1:5.4) connects the proposed VSM through a worm gear (gear ratio: 1:50). The VSM in actuator is used as a compliant coupling between the motor and the output shaft, of which variable stiffness is achieved by adjusting spring pretension or changing the VSM configuration.

The compliant actuator can then be applied for different applications. Herein, a case illustrating an application of compliant actuator in the joint of a wearable elbow exoskeleton is included, as shown in Fig. 27. In the figure, the elbow exoskeleton is mounted on an user's arm through two cuffs, and can provide physical assistance to the elbow joint of user. According to the torque model Eq. (5), the joint can output a maximum torque of 11.69 Nm, if the Spring-2 of $k = 11.4$ N/mm given in Table 2 is used, and $N = 3$ is set in the VSM. The exoskeleton can thus help users to lift a maximum payload of about 8.0 kg, if the exoskeleton provides a 50% physical assistance to the elbow joint of user. The exoskeleton joint stiffness varies in the range of [4.31, 56.13] Nm/rad, which can fits the stiffness of human elbow joint [43]. With the compliant actuator, the joint of the exoskeleton is able to realize the range of elbow flexion/extension 0–145 deg, as shown in Fig. 28. The total weight of the elbow exoskeleton is 0.94 kg excluding the weights of power source and controllers. The above characteristics of the elbow exoskeleton are summarized in Table 6.

Preliminary evaluation for usability testing on three subjects (A: height 1.8 m, weight 70 kg; B: height 1.73 m, weight 65 kg; C: height 1.87 m, weight 85 kg) has been conducted, with positive response on perceived comfortability and changes of stiffness. Further testing will be conducted in connection with control algorithms.

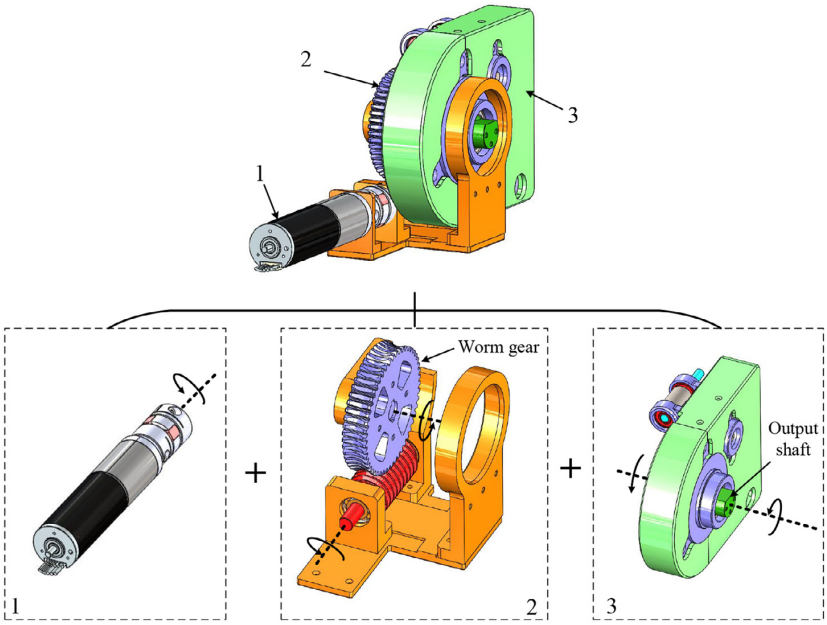

Fig. 26. CAD model of compliant actuator used in the wearable elbow exoskeleton, which consists of (1) Motor and gear box, (2) worm gear transmission unit, and (3) VSM.

Fig. 27. Wearable elbow exoskeleton prototype mounted on the arm of a subject.

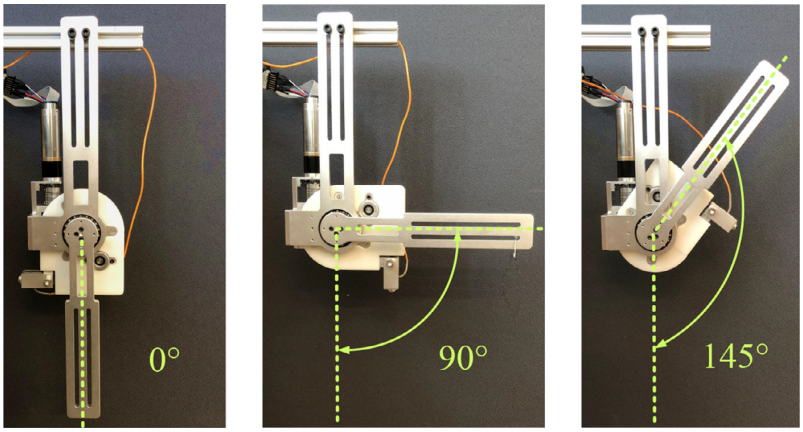

Fig. 28. Range of rotation of the wearable elbow exoskeleton.

7. Discussion and conclusions

The main objective of this work is to design a variable stiffness mechanism which can be applicable to wearable exoskeletons. A new design of VSM which is simple, compact and light weight was achieved. In addition, the VSM employs a reconfigurable design, which allows the mechanism to vary stiffness in adjustable ranges. In this work, torque and stiffness models are developed for the VSM, with which the performances of VSM are analyzed. The models are validated experimentally with both static and dynamic tests performed.

A main contribution of the work is the novel mechanical design of VSM. The new VSM is designed as a standalone module which can be integrated with motor to build variable stiffness actuator. In addition, the new design is able to change stiffness in adjustable ranges by multiple means including reconfiguration, change spring and varying preload.

As mentioned in Introduction, some VSAs use a second motor to change their stiffness online [5,8]. By this way, the actuation system can automatically adapt the compliance to different tasks. These actuators are suitable for the devices mounted on fixed supports, such as rehabilitation robots. For the case of a wearable exoskeleton applications, design with only one motor, such as the one developed in this work, is more preferable.

In this work, the frequency analysis of the mechanism has its implication in the motion control development. First. it limits the closed-loop bandwidth in both trajectory and force control, determining the minimal bandwidth. The analysis results show that the mechanism is able to change widely its natural frequency through varying the mechanism stiffness. This characteristic can enable a closed-loop bandwidth with a wide range, which makes the mechanism flexible in the usages of different applications. Secondly, the analysis can be helpful for mechanism design, for which the running speed of actuators should be away from the fundamental frequency.

It is noted that the proposed VSM has nonlinear stiffness behaviors, which makes difficult to model and analyze the dynamics. The natural frequency of such mechanism is also varying with the amplitude of joint deflection of mechanism, as shown in Fig. 20. The nonlinear stiffness behaviors are needed for many applications, with design examples of exoskeletons [1,32]. VSM can offer desirable interaction forces to human or environment. Moreover, a VSM improves energy efficiency and stability of the system [20,44,45,46], which will be a topic of future study for the proposed VSM.

The proposed VSM can be easily integrated with existing systems for various applications, such as exoskeletons [47] and servicing robots [48,49]. In this work, a case is included to show an application of VSM in wearable elbow exoskeleton. For future work, we will focus on the motion control of a system integrated with the proposed VSM. In addition, other implementation cases of robotic joints based on the proposed VSM will be explored.

Declaration of Competing Interest

The authors whose names are listed above certify that they have NO affiliations with or involvement in any organization or entity with any financial interest (such as honoraria; educational grants; participation in speakers' bureaus; membership, employment, consultancies, stock ownership, or other equity interest; and expert testimony or patent-licensing arrangements), or non-financial interest (such as personal or professional relationships, affiliations, knowledge or beliefs) in the subject matter or materials discussed in this manuscript.

Acknowledgments

The research is in part supported by Innovation Fund Denmark through Grand Solutions project Exo-aider. Z. Li acknowledges the CSC scholarship for his study at Aalborg University, Denmark. W. Chen and J. Zhang acknowledge the support of National Natural Science Foundation of China (Grant nos. 51675018 and 61773042).

Appendix A

$$c = \frac{1}{2(l_1+l_2-l_3)}\cdot\left(a\arccos\left(\frac{a-2l_1\sin\theta}{\sqrt{a^2-4al_1\sin\theta+4l_2^2}}\right)+a\arccos\left(\frac{a+2l_1\sin\theta}{\sqrt{a^2+4al_1\sin\theta+4l_2^2}}\right)\right.$$
$$-a\arccos\left(\frac{a}{\sqrt{a^2-4al_1\sin\theta+4l_2^2}}\right)-a\arccos\left(\frac{a}{\sqrt{a^2+4al_1\sin\theta+4l_2^2}}\right)+2\sqrt{l_2^2+al_1^2\sin\theta}$$
$$\left.+2\sqrt{l_2^2-al_1^2\sin\theta}+4l_1-4l_3\right) \tag{A.1}$$

$$\frac{\partial c}{\partial\theta} = \frac{al_1}{l_1+l_2-l_3}\cdot\left(\frac{a(a\cos\theta-2l_3\sin\theta)}{2\left(4l_2^2+a^2-4al_1\sin\theta\right)\sqrt{l_2^2-al_1\sin\theta}}-\frac{a(a\cos\theta+2l_3\sin\theta)}{2\left(4l_2^2+a^2+4al_1\sin\theta\right)\sqrt{l_2^2+al_1\sin\theta}}\right.$$
$$\left.+\frac{2l_3\cos\theta-2l_1+a\sin\theta}{4l_2^2+a^2-4al_1\sin\theta}+\frac{2l_1-2l_3\cos\theta+a\sin\theta}{4l_2^2+a^2+4al_1\sin\theta}\right)-\frac{l_1l_3\sin\theta}{2l_2(l_1+l_2)^2+2l_2l_3(l_3-2l_1-2l_2)}$$
$$\cdot\left(a\arccos\left(\frac{a-2l_1\sin\theta}{\sqrt{a^2-4al_1\sin\theta+4l_2^2}}\right)+a\arccos\left(\frac{a+2l_1\sin\theta}{\sqrt{a^2+4al_1\sin\theta+4l_2^2}}\right)+4l_1-4l_3\right.$$
$$-a\arccos\left(\frac{a}{\sqrt{a^2-4al_1\sin\theta+4l_2^2}}\right)-a\arccos\left(\frac{a}{\sqrt{a^2+4al_1\sin\theta+4l_2^2}}\right)+2\sqrt{l_2^2+a\sin\theta}$$
$$\left.+2\sqrt{l_2^2-a\sin\theta}\right) \tag{A.2}$$

$$\frac{\partial J}{\partial\theta} = \frac{l_1l_3\cos\theta}{l_2}-\frac{l_1^2l_3^2\sin^2\theta}{l_2^3} \tag{A.3}$$

References

[1] V. Grosu, C. Rodriguez-Guerrero, S. Grosu, B. Vanderborght, D. Lefeber, Design of smart modular variable stiffness actuators for robotic-assistive devices, IEEE/ASME Trans. Mechatron. 22 (4) (2017) 1777–1785.
[2] G. Grioli, S. Wolf, M. Garabini, M. Catalano, E. Burdet, D. Caldwell, R. Carloni, W. Friedl, M. Grebenstein, M. Laffranchi, D. Lefeber, S. Stramigioli, N. Tsagarakis, M. van Damme, B. Vanderborght, A. Albu-Schaeffer, A. Bicchi, Variable stiffness actuators: the user's point of view, Int. J. Robot. Res. 34 (6) (2015) 727–743.
[3] B. Chen, B. Zi, Z. Wang, L. Qin, W.H. Liao, Knee exoskeletons for gait rehabilitation and human performance augmentation: a state-of-the-art, Mech. Mach. Theory 134 (2019) 499–511.
[4] R.R. Torrealba, S.B. Udelman, E.D. Fonseca-Rojas, Design of variable impedance actuator for knee joint of a portable human gait rehabilitation exoskeleton, Mech. Mach. Theory 116 (2017) 248–261.
[5] O. Baser, H. Kizilhan, Mechanical design and preliminary tests of VS-AnkleExo, J. Braz. Soc. Mech. Sci. Eng. 40 (9) (2018) 442.
[6] M.A. Gull, S. Bai, T. Bak, A review on design of upper limb exoskeletons, Robotics 9 (2020) 16.
[7] A. De Santis, B. Siciliano, A. De Luca, A. Bicchi, An atlas of physical human-robot interaction, Mech. Mach. Theory 43 (3) (2008) 253–270.
[8] L. Liu, S. Leonhardt, B.J. Misgeld, Experimental validation of a torque-controlled variable stiffness actuator tuned by gain scheduling, IEEE/ASME Trans. Mechatron. 23 (5) (2018) 2109–2120.
[9] G. Tonietti, R. Schiavi, A. Bicchi, Design and control of a variable stiffness actuator for safe and fast physical human/robot interaction, in: IEEE International Conference on Robotics and Automation (ICRA), 2005, pp. 526–531.
[10] G.A. Pratt, M.M. Williamson, Series elastic actuators, in: IEEE/RSJ International Conference on Intelligent Robots and Systems (IROS), 1, Human Robot Interaction and Cooperative Robots, 1995, pp. 399–406.
[11] D.W. Haldane, M.M. Plecnik, J.K. Yim, R.S. Fearing, Robotic vertical jumping agility via series-elastic power modulation, Sci. Robot. 1 (1) (2016).
[12] S. Curran, D.E. Orin, Evolution of a jump in an articulated leg with series-elastic actuation, in: IEEE International Conference on Robotics and Automation (ICRA), 2008, pp. 352–358.
[13] D.W. Robinson, J.E. Pratt, D.J. Paluska, G.A. Pratt, Series elastic actuator development for a biomimetic walking robot, in: IEEE/ASME International Conference on Advanced Intelligent Mechatronics (AIM), 1999, pp. 561–568.
[14] J.W. Hurst, J.E. Chestnutt, A.A. Rizzi, An actuator with physically variable stiffness for highly dynamic legged locomotion, in: IEEE International Conference on Robotics and Automation (ICRA), 5, 2004, pp. 4662–4667.
[15] W.M. dos Santos, G.A. Caurin, A.A. Siqueira, Design and control of an active knee orthosis driven by a rotary series elastic actuator, Control Eng. Pract. 58 (2017) 307–318.
[16] S. Kim, J. Bae, Force-mode control of rotary series elastic actuators in a lower extremity exoskeleton using model-inverse time delay control, IEEE/ASME Trans. Mechatron. 22 (3) (2017) 1392–1400.

[17] S. Crea, M. Cempini, M. Moisé, A. Baldoni, E. Trigili, D. Marconi, M. Cortese, F. Giovacchini, F. Posteraro, N. Vitiello, A novel shoulder-elbow exoskeleton with series elastic actuators, in: IEEE International Conference on Biomedical Robotics and Biomechatronics (BioRob), 2016, pp. 1248–1253.
[18] K. Kong, J. Bae, M. Tomizuka, Control of rotary series elastic actuator for ideal force-mode actuation in human–robot interaction applications, IEEE/ASME Trans. Mechatron. 14 (1) (2009) 105–118.
[19] M.I. Awad, I. Hussain, D. Gan, A. Az-zu'bi, C. Stefanini, K. Khalaf, Y. Zweiri, T. Taha, J. Dias, L. Seneviratne, Passive discrete variable stiffness joint (pDVSJ-II): modeling, design, characterization, and testing toward passive haptic interface, J. Mech. Robot. 11 (1) (2018) 11005.
[20] S. Wolf, G. Grioli, O. Eiberger, W. Friedl, M. Grebenstein, H. Höppner, E. Burdet, D.G. Caldwell, R. Carloni, M.G. Catalano, et al., Variable stiffness actuators: review on design and components, IEEE/ASME Trans. Mechatron. 21 (5) (2016) 2418–2430.
[21] N. Vitiello, T. Lenzi, S. Roccella, S.M.M.D. Rossi, E. Cattin, F. Giovacchini, F. Vecchi, M.C. Carrozza, NEUROExos: a powered elbow exoskeleton for physical rehabilitation, IEEE Trans. Robot. 29 (1) (2013) 220–235.
[22] T. Noda, T. Teramae, B. Ugurlu, J. Morimoto, Development of an upper limb exoskeleton powered via pneumatic electric hybrid actuators with Bowden cable, in: IEEE/RSJ International Conference on Intelligent Robots and Systems (IROS), 2014, pp. 3573–3578.
[23] B. Zi, N. Wang, S. Qian, K. Bao, Design, stiffness analysis and experimental study of a cable-driven parallel 3D printer, Mech. Mach. Theory 132 (2019) 207–222.
[24] A. Jafari, N.G. Tsagarakis, D.G. Caldwell, A novel intrinsically energy efficient actuator with adjustable stiffness (AwAS), IEEE/ASME Trans. Mechatron. 18 (1) (2013) 355–365.
[25] S.S. Groothuis, G. Rusticelli, A. Zucchelli, S. Stramigioli, R. Carloni, The variable stiffness actuator vsaUT-II: mechanical design, modeling, and identification, IEEE/ASME Trans. Mechatron. 19 (2) (2014) 589–597.
[26] J. Sun, Z. Guo, D. Sun, S. He, X. Xiao, Design, modeling and control of a novel compact, energy-efficient, and rotational serial variable stiffness actuator (SVSA-II), Mech. Mach. Theory 130 (2018) 123–136.
[27] M. Dežman, A. Gams, Rotatable cam-based variable-ratio lever compliant actuator for wearable devices, Mech. Mach. Theory 130 (2018) 508–522.
[28] L. Liu, S. Leonhardt, B.J. Misgeld, Design and control of a mechanical rotary variable impedance actuator, Mechatronics 39 (2016) 226–236.
[29] J. Choi, S. Hong, W. Lee, S. Kang, M. Kim, A robot joint with variable stiffness using leaf springs, IEEE Trans. Robot. 27 (2) (2011) 229–238.
[30] M. Cestari, D. Sanz-Merodio, J.C. Arevalo, E. Garcia, An adjustable compliant joint for lower-limb exoskeletons, IEEE/ASME Trans. Mechatron. 20 (2) (2015) 889–898.
[31] R.V. Ham, B. Vanderborght, M.V. Damme, B. Verrelst, D. Lefeber, MACCEPA, the mechanically adjustable compliance and controllable equilibrium position actuator: design and implementation in a biped robot, Robot. Auton. Syst. 55 (10) (2007) 761–768.
[32] T. Bacek, M. Moltedo, C. Rodriguez-Guerrero, J. Geeroms, B. Vanderborght, D. Lefeber, Design and evaluation of a torque-controllable knee joint actuator with adjustable series compliance and parallel elasticity, Mech. Mach. Theory 130 (2018) 71–85.
[33] J. Vantilt, K. Tanghe, M. Afschrift, A.K. Bruijnes, K. Junius, J. Geeroms, E. Aertbeliën, F.D. Groote, D. Lefeber, I. Jonkers, J.D.S. Tanghe, Model-based control for exoskeletons with series elastic actuators evaluated on sit-to-stand movements, J. Neuroeng. Rehabil. 16 (1) (2019) 65.
[34] R. Furnémont, G. Mathijssen, T. van der Hoeven, B. Brackx, D. Lefeber, B. Vanderborght, Torsion MACCEPA: a novel compact compliant actuator designed around the drive axis, in: IEEE International Conference on Robotics and Automation (ICRA), 2015, pp. 232–237.
[35] M. Moltedo, G. Cavallo, T. Bavek, J. Lataire, B. Vanderborght, D. Lefeber, C. Rodriguez-Guerrero, Variable stiffness ankle actuator for use in robotic-assisted walking: control strategy and experimental characterization, Mech. Mach. Theory 134 (2019) 604–624.
[36] Y. Liu, X. Liu, Z. Yuan, J. Liu, Design and analysis of spring parallel variable stiffness actuator based on antagonistic principle, Mech. Mach. Theory 140 (2019) 44–58.
[37] Y.-S. Wu, C.C. Lan, Linear variable-stiffness mechanisms based on preloaded curved beams, J. Mech. Des. 136 (12) (2014) 122302.
[38] Z. Li, W. Chen, S. Bai, A novel reconfigurable revolute joint with adjustable stiffness, in: IEEE International Conference on Robotics and Automation (ICRA), 2019, pp. 8388–8393.
[39] Z. Li, S. Bai, A novel revolute joint of variable stiffness with reconfigurability, Mech. Mach. Theory 133 (2019) 720–736.
[40] E. Saerens, R. Furnémont, T. Verstraten, P.L. García, S. Crispel, V. Ducastel, D. Lefeber, Scaling laws of compliant elements for high energy storage capacity in robotics, Mech. Mach. Theory 139 (2019) 482–505.
[41] P. Beckerle, T. Verstraten, G. Mathijssen, R. Furnémont, B. Vanderborght, D. Lefeber, Series and parallel elastic actuation: influence of operating positions on design and control, IEEE/ASME Trans. Mechatron. 22 (1) (2017) 521–529.
[42] V. Giurgiutiu, Structural Health Monitoring with Piezoelectric Wafer Active Sensors: Chapter 3 - Vibration Fundamentals, Academic Press, 2014, pp. 51–143.
[43] H. Gomi, M. Kawato, Human arm stiffness and equilibrium-point trajectory during multi-joint movement, Biol. Cybern. 76 (1997) 163–171.
[44] J. Austin, A. Schepelmann, H. Geyer, Control and evaluation of series elastic actuators with nonlinear rubber springs, in: IEEE/RSJ International Conference on Intelligent Robots and Systems, 2015, pp. 6563–6568.
[45] J.-J. Park, Y.-J. Lee, J.-B. Song, H.S. Kim, Safe joint mechanism based on nonlinear stiffness for safe human-robot collision, in: IEEE International Conference on Robotics and Automation, 2008, pp. 2177–2182.
[46] D. Owaki, A. Ishiguro, Enhancing stability of a passive dynamic running biped by exploiting a nonlinear spring, in: IEEE/RSJ International Conference on Intelligent Robots and Systems, 2006, pp. 4923–4928.
[47] S. Christensen, S. Bai, Kinematic analysis and design of a novel shoulder exoskeleton using a double parallelogram linkage, J. Mech. Robot. 10 (4) (2018) 41008.
[48] L. Zhou, S. Bai, M.R. Hansen, Design optimization on the drive train of a light-weight robotic arm, Mechatronics 21 (3) (2011) 560–569.
[49] L. Zhou, S. Bai, A new approach to design of a lightweight anthropomorphic arm for service applications, J. Mech. Robot. 7 (3) (2015) 31001.

Chapter 7

Paper IV

Mechatronics design and testing of a novel actuator with nonlinear compliances

Zhongyi Li, Muhammad Raza Ul Islam, Weihai Chen, Jianbin Zhang, and Shaoping Bai

The paper has been submitted to
IEEE/ASME Transactions on Mechatronics

Mechatronics design and testing of a novel actuator with nonlinear compliance

Zhongyi Li, *Student member, IEEE,* Muhammad Raza Ul Islam, Weihai Chen, *Member, IEEE,*Jianbin Zhang, and Shaoping Bai, *Senior member, IEEE*

***Abstract*—In this paper, a novel compliant actuator of nonlinear stiffness is presented. The compliant actuator is designed with a variable stiffness mechanism (VSM), thereby enabling adjustable impedance of the actuator. Moreover, the VSM has self-sensing function to detect torque applied, with high sensitivity to small load. This makes possible for us to control torque conveniently. In the paper, static calibrations are performed to obtain the torque sensing capacity of the VSM. Torque control of the actuator is realized using the VSM-based torque sensor. Both simulations and experiments are performed to validate the feasibility of actuator in controlling torque.**

***Index Terms*—compliant actuator, variable stiffness mechanism, torque control, physical human-robot interaction**

I. Introduction

ROBOTS that interact with humans, such as assistive exoskeletons and rehabilitation robots [1], [2], [3], [4], have to be developed with a certain level of compliance. In other words, the actuators in these robots need to have a low impedance, so as to be compliant to the human motions. In this regard, traditional stiff actuators in industrial applications cannot meet this critical requirement. Instead, compliant actuators represented by serial elastic actuators (SEAs) and variable stiffness actuators (VSAs) can provide effective solutions for the problem.

The concept of SEA was first proposed by Pratt and Williamson in [5], in which a serial elasticity was introduced between the motor and the actuator output. The introduced elasticity reduces the mechanical impedance of the system, thus help to improve the adaptability of the actuator in dealing with unstructured environments. Moreover, considering the torque-deflection relationship, the elastic element introduced in the actuator can be used to measure the torque applied on actuator output. These features make the SEA suitable for robots which interact with human. Up to date, various SEAs have been constructed, and some of them have been employed in robots. In [6], Kong et al. proposed an orthosis robot which is integrated with a rotary SEA. The rotary SEA working with a torque control algorithm can generate ideal torque when the orthosis interacts with a human. In [7], another SEA for knee joint assistance was proposed by Kong et al. too. Compared with the SEA presented in [6], the new one used a torsional spring with a lower stiffness to achieve a lower impedance and a higher torque resolution for the actuator. In [8], a custom-designed spring was presented and used in an active knee orthosis to achieve an accurate torque sensing capability. The SEA concept was also employed in hopping and walking robots [9], [10], [11], [12], enabling large energy efficiency and high stability of these robots to shocks. However, the SEA has a very limited force/torque resolution and bandwidth resulting from the fixed compliance of the used elastic element. A soft elastic element is sensitive to small force/torque, but results in a low bandwidth of the actuator. A stiff elastic element has advantage in increasing the bandwidth, but reduces the torque resolution. These limitations highly reduce the adaptability of a SEA to application variability and change.

To overcome the limitations of SEAs, compliant actuators with capacity of stiffness adjustment, i.e. VSA, have been studied. A variable stiffness enables actuators to have a high bandwidth at high stiffness level and high torque resolution at low stiffness level. In general, a variable stiffness mechanism (VSM) is used in VSA to regulate its compliance rather than a fixed compliance in SEA. Stiffness variation of the VSM can be achieved by taking advantages of different methods, e.g. varying transmission ratio, adjusting the physical properties of spring, and changing the spring preload. In [13], Jafari et al. proposed a VSA, namely AwAS, where its stiffness variation is achieved through changing the transmission ratio of a lever mechanism. Based on the same principle, Jafari et al. also presented another VSA, namely AwAS-II [14], which is an evolution of AwAS with more compact size. Liu et al. developed MeRIA, which was used in lower limb exoskeleton for rehabilitation training [15]. In the MeRIA design, two leaf springs were adopted, and their physical properties were changed through varying the effective length, thereby enabling the stiffness variation of actuator. Other VSAs, such as vsaUT [16], SVSA-II [17], PLVL-VSA [18] JVSR [19] and VSJ [20] are noticeable too.

In most of aforementioned cases, double-actuation configuration is adopted. With such configuration, while these actuators can change their stiffness online, and thereby be adaptive to environments, the double-actuation configuration leads to increased size, weight and complexity, which brings limitations in employing actuators of this type in wearable device.

In this paper, a novel nonlinear elastic actuator is presented. The actuator is developed from a VSM which was recently reported in [21]. The VSM is compact and lightweight, and

Zhongyi Li, Muhammad Raza Ul Islam and Shaoping Bai are with the Department of Materials and Production, Aalborg University, 9220 Aalborg, Denmark e-mail: shb@mp.aau.dk.

Weihai Chen is the School of Automation Science and Electrical Engineering, Beihang University, 100191 Beijing, China.

Jianbin Zhang is the School of Mechanical Engineering and Automation, Beihang University, 100191 Beijing, China.

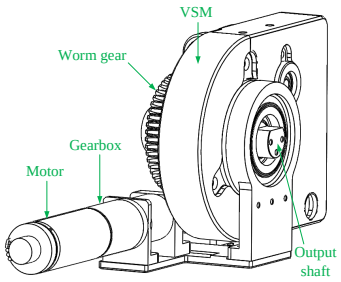

Fig. 1. CAD model of a compliant actuator constructed with a VSM.

TABLE I
SPECIFICATIONS OF THE COMPLIANT ACTUATOR

Specification	Value	Unit
Maximum continuous output torque	9.6	[Nm]
Maximum stiffness	26.91	[Nm/rad]
Minimum stiffness	2.17	[Nm/rad]
Maximum deflection	0.53	[rad]
Dimension	200×97.5×58.5	[mm]
Weight	0.6	[kg]

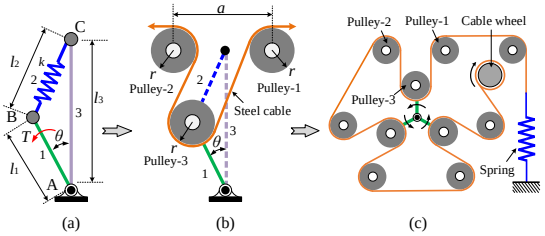

Fig. 2. Working principle of stiffness variation of the VSM, (a) two bars coupled with a spring, (b) an implementation with cable and pulley, (c) a configuration with three branches (N=3).

can be readily integrated with motor to construct a compliant actuator. In this work, the VSM is used as a torque generator, as well as a torque sensor which enables feedback control for the actuator. The variable stiffness of the VSM allows an adjustable sensitivity for torque measurement, and results in a variable control bandwidth. With the VSM, torque control was realized on this actuator by using a position controller, with which tests were performed to show the feasibility of actuator in controlling torque. Both simulations and experiments are carried out to evaluate the performance of the controller.

The paper is organized as follows: Section II presents the mechanical design of the compliant actuator. In Section III, the characteristics of the VSM in torque sensing, including measurement range, hysteresis and repeatability, was obtained. Section IV describes a controller design to implement torque control. Test results were presented in Section V, and Section VI concludes this work.

II. MECHANICAL DESIGN OF A COMPLIANT ACTUATOR

This section introduces the mechanical design and working principle of a compliant actuator which is constructed by integrating a motor with a variable stiffness mechanism.

Fig. 1 depicts the compliant actuator, in which a variable stiffness mechanism (VSM) is employed to provide serial elasticity between the worm gear and the output shaft. The joint stiffness of the actuator can be adjusted thanks to the employed VSM. A Maxon EC-4pole motor (power: 90W) provides power source for the actuator, which is driven by ESCON servo controller. The motor torque is transmitted to the VSM through a gearbox (gear ratio n_1= 1:5.4) and a worm gear (gear ration n_2= 1:50). The details about the actuator specifications are given in Table I. Noting that, the stiffness adjustment range and joint deflection of the actuator depend on the employed VSM which is described as follows.

In the compliant actuator, the VSM plays double roles as an buffer isolating the motor from external load, as well as a torque sensing device. Herein, we briefly describe the working principle and the mechanical design of the VSM. The variable stiffness of the designed VSM is achieved based on a spring-loaded mechanism, as shown in Fig. 2 (a). In the mechanism, bar-1 and 3 are the output and input links respectively, which rotate around a pin joint A. Bar-2 is a linear spring which connects the output and input links at pin joints B and C, thereby introducing serial elasticity between the output and the input of the mechanism. According to the virtual work principle, the relationship between joint deflection θ and joint torque T of the mechanism can be obtained as

$$T = Jk\delta l_2 + JF_0 \tag{1}$$

with

$$J = \frac{l_1 l_3 \sin\theta}{\sqrt{l_1^2 + l_3^2 - 2l_1 l_3 \cos\theta}} \tag{2}$$

$$\delta l_2 = \sqrt{l_1^2 + l_3^2 - 2l_1 l_3 \cos\theta} + l_1 - l_3 \tag{3}$$

where l_1, l_2 and l_3 are the lengths of three bars, k is the spring constant, F_0 is the spring pretension applied at $\theta = 0$.

In the VSM design, the spring-loaded mechanism is implemented using the configuration shown in Fig. 2 (b). In this configuration, pulleys and cable are used allowing the linear spring to be placed away from the output and input links as shown in Fig. 2 (c), thereby avoiding interference between the spring and links. Based on the configuration shown in Fig. 2 (c), the VSM was constructed as shown in Fig. 3. In the VSM, two flanges are design on two coaxial shafts, input and output shafts. The two flanges are coupled through a cable-pulley-spring system.

The VSM is constructed with three branches, and each branch has the same configuration shown in Fig. 2 (b). Based on Eq. (1), the static model of the VSM is formulated as

$$T_{vsm} = c^2 N^2 Jk\delta l_2 + cNJF_0 \tag{4}$$

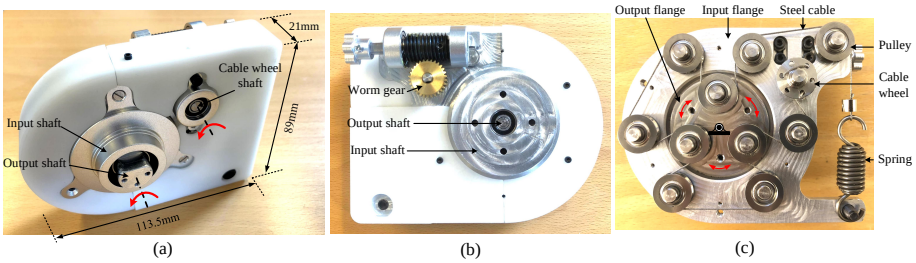

Fig. 3. VSM design. The worm gear in (b) is used to adjust pretension F_0.

where N is the number of branches in the VSM, and $c \approx 2$ which is a factor describing the influences of geometry of the VSM namely, dimensions of a and r in Fig. 2(b), on the spring elongation [21].

According to Eq. (4), the stiffness model can be obtained as

$$K = N^2 \left(c^2 J^2 + c^2 \frac{\partial J}{\partial \theta} \delta l_2 \right) + N c F_0 \frac{\partial J}{\partial \theta} \tag{5}$$

where

$$\frac{\partial J}{\partial \theta} = \frac{l_1 l_3 \cos\theta}{l_2} - \frac{l_1^2 l_3^2 \sin^2\theta}{l_2^3} \tag{6}$$

Eq. (4) implies that the torque-deflection characteristic of the VSM can be modified by adjusting the spring pretension F_0. Fig. 4 shows torque-deflection and stiffness-deflection curves with the influences of F_0, with which the changes of T_{vsm} and K with parameter variation can be observed clearly. The design parameters of the VSM for simulation are given in Table II, which are also parameters of the prototype shown in Fig. 3. It can be observed from the plots in Fig. 4 (b) that the stiffness increases with the deflection. Moreover, the mechanism exhibits zero stiffness at θ=0 if no pretention is applied.

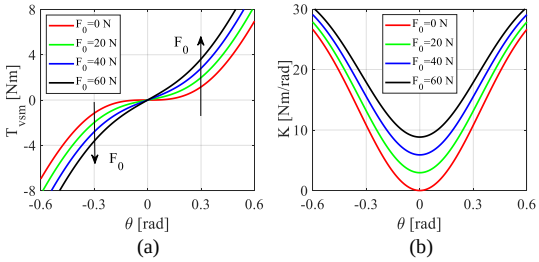

Fig. 4. (a) Joint torque T_{vsm} versus deflection θ curves and (b) stiffness curves.

III. VSM-BASED TORQUE SENSOR

Eq. (4) implies that the VSM, after calibration, can be used a torque sensor. Static calibration was carried out by using the test rig shown in Fig. 5. In the test rig, a torque sensor

TABLE II
DESIGN PARAMETERS OF THE VSM

Parameters	Value	Unit
l_1	13.5	[mm]
l_3	30	[mm]
k	4.42	[N/mm]

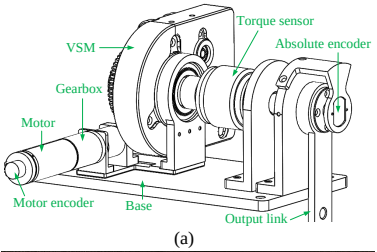

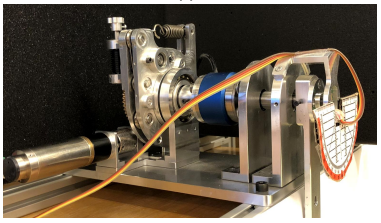

Fig. 5. (a) CAD model and (b) real construction of the test rig.

(model: Forsentek FTE-20NM) is connected to the output shaft of the VSM for calibration. An absolute encoder (model: RLS RMB20) is used to measure deflection. The position of the motor shaft is measured by using an encoder (model: Encoder MR, Type ML). By fixing the input shaft of the VSM in the calibration experiment, the joint deflection θ of the VSM is identical to the output link rotation θ_{out}. Thus, the value of θ can be directly measured by the absolute encoder. By offsetting the output link, external torque was applied on the VSM, and its value was measured using the torque sensor. In the experiments, the sensors' signals were acquired with

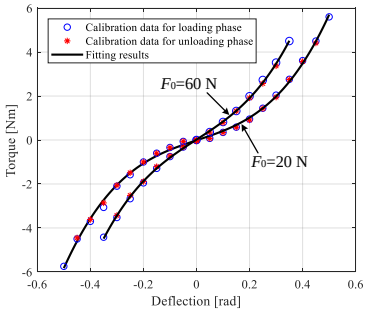

Fig. 6. Static calibration results.

Arduino DUE board.

The torque-deflection characteristics of the actuator were evaluated experimentally. Tests with two spring pretension levels: $F_0 = 20$ and 60 N, were considered. In the test for $F_0 = 20$ N, we applied torque on the output link to rotate the joint following the sequence:

$$0 \underbrace{\rightarrow 0.5}_{\text{ld}} \underbrace{\rightarrow 0}_{\text{ud}} \underbrace{\rightarrow -0.5}_{\text{ld}} \underbrace{\rightarrow 0}_{\text{ud}} \text{ rad}$$

where ld and ud stand for the loading and unloading phase respectively. The sequence was repeated for three times to obtain the device's repeatability. The sensor signals were recorded in every 0.05 rad joint angle steps. Similar procedure was followed for the test with $F_0 = 60$ N, except the maximum rotation angle changing to 0.35 rad.

Fig. 6 shows the calibration results, in which the torque-deflection characteristics of both loading and unloading phases are given. In Fig. 6, cubic polynomial curve fittings yield

$$f(\theta, F_0) = 30.066\theta^3 - 0.203\theta^2 + 4.011\theta, \ F_0 = 20 \text{ N} \quad (7)$$

$$f(\theta, F_0) = 41.283\theta^3 - 0.034\theta^2 + 7.799\theta, \ F_0 = 60 \text{ N} \quad (8)$$

These curve fittings achieve R-squared values of 0.998 and 0.999 for $F_0 = 20$ N and $F_0 = 60$ N, respectively. Based on the calibration, the performances of torque sensing by the VSM are obtained, as listed in Table III. Of these performances, hysteresis is obtained from

$$\xi_h = \frac{\max\left(\bar{T}_{vsm,d}(\theta_i) - \bar{T}_{vsm,ud}(\theta_i)\right)}{T_{vsm,max}} \times 100\% \quad (9)$$

where $\bar{T}_{vsm,d}(\theta)$ and $\bar{T}_{vsm,ud}(\theta)$ are the average values of the loading and unloading joint torques measured at $\theta = \theta_i$, and $T_{vsm,max}$ is the maximum torque measured in the experiments.

TABLE III
STATIC CALIBRATION RESULTS

Property	Value	
	$F_0 = 20$ N	$F_0 = 60$ N
Range [Nm]	[-5.8, 5.8]	[-4.5, 4.5]
Repeatability	6.34% FS	8.6% FS
Hysteresis	3.16% FS	4.67% FS

*FS: Full Scale

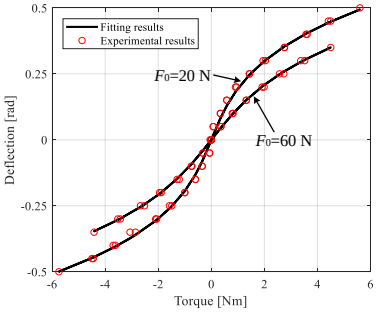

Fig. 7. Fitting results for deflection-torque curves of the VSM.

The repeatability is obtained by

$$\xi_r = \frac{t_{0.95} \cdot \max\left(\sqrt{\frac{1}{3}\sum_{j=1}^{3}\left(T_{vsm}(\theta_{i,j}) - \bar{T}_{vsm}(\theta_i)\right)^2}\right)}{T_{vsm,max}} \times 100\% \quad (10)$$

where $T_{vsm}(\theta_{i,j})$ is the measured torque value at $\theta = \theta_i$ for j-th cycle, and $\bar{T}_{vsm}(\theta_i)$ is the average value of the measured torques at $\theta = \theta_i$, and $t_{0.95} = 4.303$ is reliability factor [22].

Eqs. 7 and 8 build the nonlinear relationships between the joint torque T_{vsm} and the deflection θ of the VSM. By inverting these equations, the actuator's compliance for an applied torque is found as

$$\theta = f^{-1}(T_{vsm}, F_0) \quad (11)$$

It is noted that, due to the complexity of the nonlinearity of the VSM, $f^{-1}(T_{vsm}, F_0)$ cannot be obtained directly. In this work, we use multilayer perceptron networks based regression method, namely, *newff*, embedded in MatLab, to estimate the compliance. In the networks, the input and output parameters are the torque and deflection angle respectively. The data for training regression models is obtained from Eqs. 7 and 8. Two regression models for $F_0 = 20$ and $F_0 = 60$ N are built in Matlab R2017b. The mean squared errors for the two regression models are 3.2353×10^{-6} and 3.6168×10^{-8}. The fitting results are shown in Fig. 7. As can be seen that the experimental results are close to the fitting curves simulated from the regression models. Given a desired torque, the joint

deflection can be predicted with a high accuracy through the regression models. Thus, the built models can be further used in the torque control, as presented in Section IV.

IV. Torque controller design

In assistive applications such as exoskeletons, their motion control is essentially a problem of torque control. The calibrated compliance model of the VSM allows us to convert a torque control problem into a position control, which makes it readily to implement.

It is noted that many control methods have been developed for SEA and VSA [13], [23], for example, using a simple proportional (P) controller or proportional derivative (PD) controller, which can realize torque control with good stability. Moreover, some methods including H_∞ and gain-scheduled methods have been used to further improve the controller stability [8], [15]. In this work, a PD torque controller is developed to validate the feasibility of the proposed actuator.

A. Control system

The control system includes a ESCON 50/5 servo controller, maxon EC motor, encoders, Arduino DUE board and a computer. The ESCON is responsible to control the motor in velocity mode, of which the control commands are sent by the computer through Arduino. The encoder readings are collected by Arduino, and then the data is transmitted to computer through serial communication with the frequency of 500 Hz.

Fig. 8 shows a block diagram of torque controller. In this controller, given the desired joint torque $T_{vsm,ref}$, the regression model built in Section III estimates the reference deflection angle θ_{ref} in real time from Eq. (11). The reference deflection angle is tracked through a PD control which outputs the desired velocity for the motor. The inner velocity control loop is performed in the ESCON. The motor velocity $\dot{\theta}_m$ is measured by a hall sensor built in the EC motor. The motor rotation θ_m and the angle of output shaft θ_{out} are measured by encoders.

B. Torque controller design

Fig. 9 illustrates the scheme of the dynamics of the compliant actuator. According to Newton's 2nd law, the motor torque can be expressed as

$$T_m = J_e\ddot{\theta}_m + B_e\dot{\theta}_m + n^2\beta_2 T_{vsm}(\theta) \tag{12}$$

with

$$J_e = J_m + \beta_1 J_g + \beta_1 J_{wg} + \beta_2 J_{ww} + \beta_2 J_{vsm} \tag{13a}$$
$$B_e = B_m + \beta_2 B_{vsm} \tag{13b}$$
$$\beta_1 = \frac{1}{n_1^2\eta_g} \quad \text{and} \quad \beta_2 = \frac{1}{n^2\eta_g} \tag{13c}$$

where all parameters are given in Table IV.

The joint deflection θ of the VSM can be found

$$\theta = \frac{\theta_m}{n} - \theta_{out} \tag{14}$$

TABLE IV
Descriptions of dynamic parameters

Parm.	Description	Value
I_m	inertia of the motor	5.54×10^{-7} kgm^2
I_g	inertia of the gearbox	6×10^{-8} kgm^2
I_{wg}	inertia of the worm gear	4.46×10^{-6} kgm^2
I_{ww}	inertia of the worm wheel	2.3×10^{-5} kgm^2
I_{vsm}	inertia of the VSM	3×10^{-5} kgm^2
B_m	viscous damping coeff. of the motor	1.35×10^{-6}Nms/rad
B_{vsm}	viscous damping coeff. of the VSM	5.5×10^{-3}Nms/rad
n_1	gear ratio of the gearbox	1:5.4
n_2	gear ratio of the worm gear	1:50
n	the total gear ratio of the drivetrain	1:270
η_g	gearbox efficiency	84 %

For the purpose of analysis of torque control performance, we set the output angle θ_{out} to zero [24]. In this way, the joint deflection θ of the VSM is proportional to the rotation θ_m of the motor,

$$\theta_m = n \cdot \theta \tag{15}$$

According to Kirchhoff's voltage law, the dynamic model of the motor is given by

$$U = L\dot{I} + RI + k_s\dot{\theta}_m \tag{16}$$

with

$$T_m = k_t I \tag{17}$$

where U is the motor voltage, and I is the actual motor current, and k_s and k_t are the speed and torque constants, and L and R are the terminal inductance and resistance respectively. The motor parameters, k_s, k_t, L and R are available on the motor datasheet. Herein, they are specified in Table V.

Combining Eqs. 12 and 16 yields the electro-mechanical model of the whole system, which is expressed in state space as

$$\dot{\mathbf{x}} = \mathbf{f} + \mathbf{g}u \tag{18}$$

where

$$\mathbf{x} = \begin{bmatrix} x_1 & x_2 & x_3 \end{bmatrix}^T = \begin{bmatrix} \theta_m & \dot{\theta}_m & I \end{bmatrix}^T \tag{19a}$$
$$u = U \tag{19b}$$
$$\mathbf{f} = \begin{bmatrix} x_2 & \frac{-B_e x_1 - n^2\beta_2 T_{vsm}(x_1) + k_t x_3}{J_e} & \frac{-k_s x_2 - R x_3}{L} \end{bmatrix}^T \tag{19c}$$
$$\mathbf{g} = \begin{bmatrix} 0 & 0 & \frac{1}{L} \end{bmatrix}^T \tag{19d}$$

So far, we have obtained the system dynamics, with which the torque controller is designed. As shown in Fig. 8, the desired compliance $\theta_{m,ref}$ is first calculated using Eq. (11).

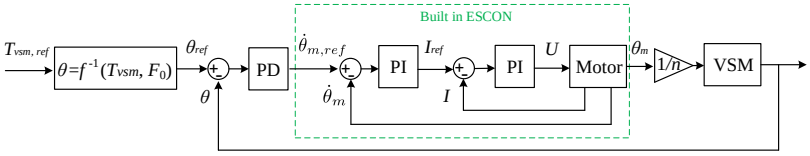

Fig. 8. Schematic diagram of torque control of the system.

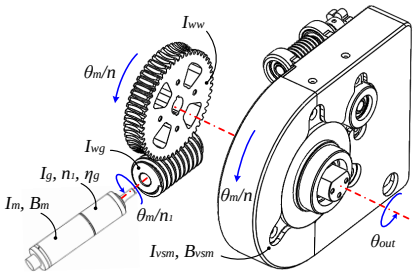

Fig. 9. Dynamic model of compliant actuator integrated with the VSM.

The compliance is then tracked through the PD controller which outputs the desired motor velocity

$$\dot{\theta}_{m,ref}(s) = nk_p^p e_{ref}(s) + nk_d^p \dot{e}_{ref}(s)\, s \tag{20}$$

where $e_{ref}(s) = \theta_{ref}(s) - \theta(s)$, k_p^p and k_d^p are the proportional and derivative gains, respectively.

The motor tracks the desired velocity $\dot{\theta}_{m,ref}$ through a PI controller which is built in the ESCON. The PI controller is formulated as

$$I_{ref}(s) = k_p^v e_m(s) + \frac{k_i^v}{s} e_m(s) \tag{21}$$

where $e_m(s) = \dot{\theta}_{m,ref}(s) - \dot{\theta}_m(s)$, I_{ref} is the desired current for the motor control, and k_p^v and k_i^v are the proportional and integral gains, respectively.

In the ESCON, a cascade PI current controller is implemented to track the desired current I_{ref}, which is given by

$$U(s) = k_p^i e_i(s) + \frac{k_i^i}{s} e_i(s) \tag{22}$$

where $e_i(s) = I_{ref}(s) - I(s)$, k_p^i and k_i^i are the proportional and integral gains, respectively.

The following limitations in velocity and current controllers are applied for anti windup purpose,

TABLE V
MOTOR PROPERTIES

Parameter	Description	Value
k_s	speed constant	35.59 rad/s/V
k_t	torque constant	0.0281 Nm/A
L	terminal inductance	1.005×10^{-4} H
R	terminal resistance	1.15 Ω

$$\dot{\theta}_{m,ref} = \begin{cases} \dot{\theta}_{m,max}, & \dot{\theta}_m > \dot{\theta}_{m,max} \\ \dot{\theta}_{m,ref}, & -\dot{\theta}_{m,max} < \dot{\theta}_{m,ref} < \dot{\theta}_{m,max} \\ -\dot{\theta}_{m,max}, & \dot{\theta}_{m,ref} < -\dot{\theta}_{m,max} \end{cases} \tag{23a}$$

$$I_{ref} = \begin{cases} I_{max}, & I > I_{max} \\ I_{ref}, & -I_{max} < I < I_{max} \\ -I_{max}, & I < -I_{max} \end{cases} \tag{23b}$$

where $\dot{\theta}_{m,max} = 1570$ rad/s and $I_{max} = 8$ A are the maximum allowable motor velocity and current.

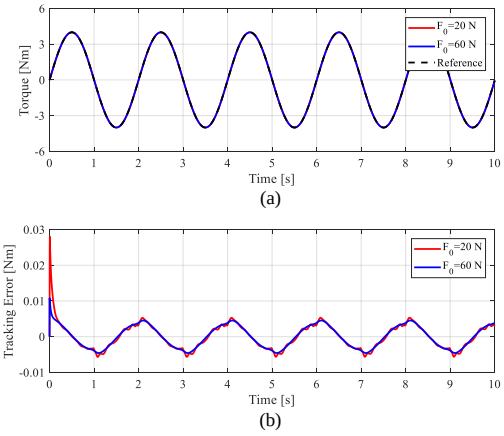

Fig. 10. Simulation results of torque profile tracking.

C. Simulations

Simulations were carried out with MATLAB/Simulink to evaluate the performance of the designed controller. In simu-

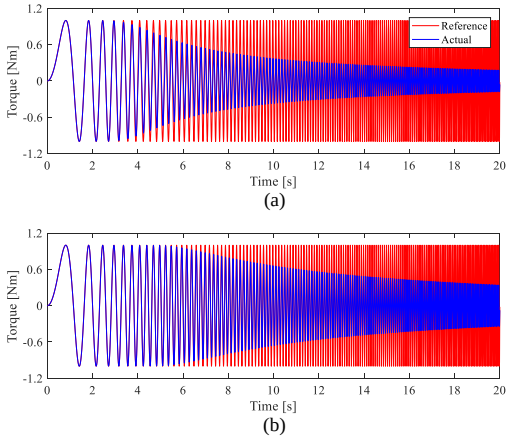

Fig. 11. Simulation results for (a) F_0 =20 N and (b) F_0 =60 N, when the desired torque is a chirp signal.

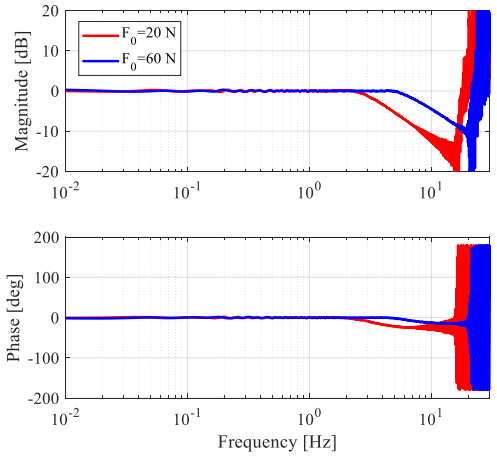

Fig. 12. Frequency responses of the torque control for the system in the conditions of F_0 =20 N and F_0 =60 N.

lations, the control plant is defined by the model of Eq. (12), in which the values of parameters are given in Table IV. The values of control gains are specified in Table VI, which are consistent with the ones in experiments in Section V.

In the simulations, the actuator was controlled to track a torque profile which is defined as

$$T_{vsm,ref} = A \cdot \sin(2\pi f \cdot t) \tag{24}$$

where A =4 Nm, and f =0.5 Hz.

Fig. 10 shows the simulation results. We can see from the figure that the actual torque profiles closely match the reference ones. The maximum errors for $F_0 = 20$ and 60 N are 0.028 and 0.01 Nm respectively.

TABLE VI
CONTROL GAINS

Parameter	Description	Value
k_p^p	proportional gain of PD position controller	12
k_d^p	derivative gain of PD position controller	0.4
k_p^v	proportional gain of PI velocity controller	47
k_i^v	integral gain of PI velocity controller	3.3
k_p^i	proportional gain of PI current controller	608
k_i^i	integral gain of PI current controller	8

To investigate the control bandwidth, another simulation was performed, in which the desired torque, $T_{vsm,ref}$, is defined as a chirp signal which has amplitude of 1 Nm and frequency varying from 1 to 15 Hz in 20 s.

Fig. 11 shows the time history of simulation results for the system in conditions of $F_0 = 20$ and 60 N. we can see from the figure that the actual torque follows the reference profile well at low frequency, but a noticeable attenuation of the actual torque amplitude occurs at high frequency. This is due to the motor current and velocity saturation limits given in Eq. (23). When these limits are exceeded, nonlinear disturbances are introduced into the system, which affects the control performance [23]. Moreover, the joint stiffness affects the attenuation speed. As can be seen from Fig. 11, a lower joint stiffness (F_0 =20 N) results in a faster attenuation. This is due to that the deflection angle and motor velocity for F_0 =20 N needed to achieve desired torque are larger than the one for F_0 =60 N. It is thus easier to exceed the saturation limits for F_0 =20 N. Bode plots of the torque controller are further obtained, as shown in Fig. 12. The torque control bandwidth for $F_0 = 20$ and 60 N are 3.7 and 7.7 Hz respectively.

V. LOW IMPEDANCE TEST

The torque controller is able to generate a low impedance in actuation, which is desirable to improve the system transparency when it interacts with human. This is achieved by setting the desired torque $T_{vsm,ref}$ of the presented controller to zero, so that the system does not generate any resistance to the human. Tests were performed by manually pushing the end of the output link to rotate back and forth. while the desired torque $T_{vsm,ref}$ sets to zero. The output link's rotating frequency varies from 0 to 0.6 Hz in 50 s, and with an amplitude about 0.26 rad.

Fig. 13 shows the results of system responses to the human motion. In the experiment, the spring pretension of the VSM in system was set to 20 N. The motion of output link is assumed to be totally contributed by the human. Fig. 13 (a) shows the measured angles of θ_{out}, θ_m/n and θ. As can be seen from this figure, the amplitude of the joint deflection θ of the VSM increases as the frequency increases, and θ has a maximum amplitude of 0.2075 rad at $t = 48$ s. Based on the data of θ, the resistive torque to the subject can be calculated using

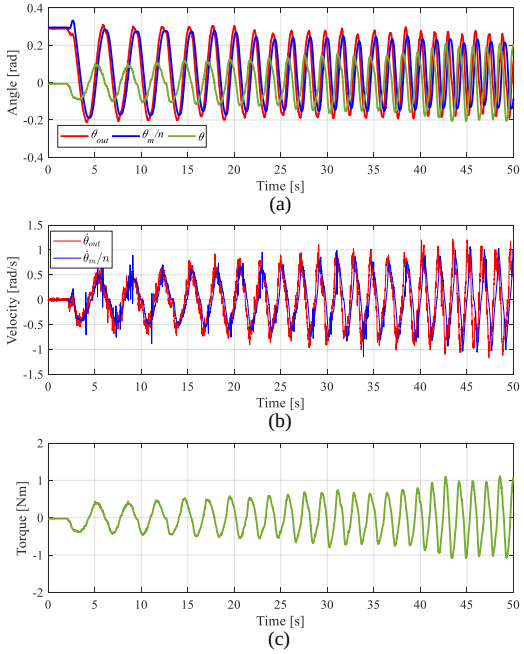

Fig. 13. Experimental results of zero torque control for $F_0 = 20$ N. (a) The joint angles, (b) joint velocities and (c) VSM joint torque.

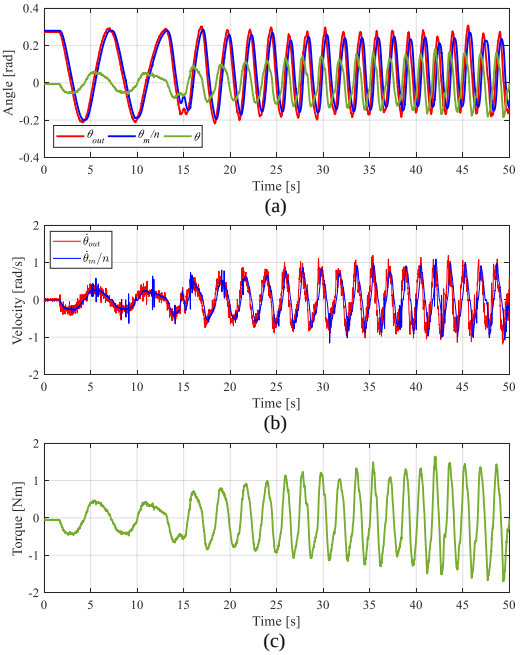

Fig. 14. Experimental results of zero torque control for $F_0 = 60$ N. (a) The joint angles, (b) joint velocities and (c) VSM joint torque.

Eq. (7), as shown in Fig. 13 (c). We can see from Fig. 13 (b) and (c) that the resistance is proportional to the joint velocities of $\dot{\theta}_{out}$ and $\dot{\theta}_m$, which is caused by the presence of damping in the system.

In another test, the spring pretension F_0 of VSM is set to 60 N, which increases the joint stiffness. The results are displayed in Fig. 14. As can be seen from Fig. 14 (a), the maximum amplitude of the joint deflection θ for F_0=60 N is 0.184 rad, which is slightly lower than the one for F_0=20 N. Due to the higher stiffness of the VSM joint for F_0=60 N, the system can generate a larger resistance to the subject with a smaller joint deflection angle. We can see from Fig. 14 (c), the maximum resistance torque is 1.69 Nm, while the one for F_0=20 N is 1.09 Nm.

The compliant actuation system was also controlled to track a desired torque profile given in Eq. (24). Knowing the desired torque, the joint deflection θ can be obtained using the regression models built in section III. In the tests, the output link of the system was fixed, and the motor was commanded to track the reference deflection θ_{ref} predicted by the regression models. Fig. 15 shows the experimental results for both $F_0 = 20$ and 60 N. As can be seen from Fig. 15 that the measured torque can follow the reference profile well. However, phase lags are noticeable in the torque control. This is likely due to the intrinsic damping of the motor which increases the response in motor velocity control, as well as the limitation of communication frequency in control hardware.

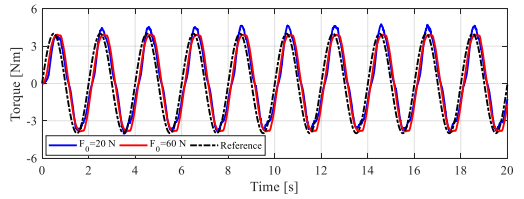

Fig. 15. Experiments results for $F_0 = 20$ and 60 N, when the desired torque varies as harmonic function.

On the other hand, the phase lag problem does not affect the stability.

VI. Discussion and Conclusions

The aim of this work is to design and control of a novel compliant actuator of nonlinear stiffness. In the design, a VSM is used to provide adjustable compliance. The VSM is used as a torque generator, as well as a torque sensor, which makes the torque control to be implemented conveniently. In this work, the torque sensing capacity of the VSM is modelled and experimentally verified. Based on the VSM-based torque sensing capacity, torque control of the actuator is realized, and its feasibility is validated with both simulations and experiments.

The main contribution of this work is the novel design of compliant actuator. In the new design, a VSM is integrated into the system, enabling the stiffness adjustment capacity of the actuator. This capacity allows the actuator changing torque resolution and bandwidth, which makes the actuator flexible in fitting various tasks in physical human-robot applications such as exoskeletons.

The developed actuator can achieve a very low compliance and a very large joint deflection angle, which has benefits in increasing the safety of the actuator to impact loads. It has to be noted that the low compliance also reduces the control bandwidth. With low joint compliance, the motor must be controlled to generate a large joint deflection to achieve a desired torque. In other words, the motor should be worked in a high velocity level, so that the desired torque can be reached in time. However, this cannot be done as expected, due to the velocity limitation of motor. This has been shown in Fig. 11. Moreover, the control response is limited by the communication frequency in control hardware. A common problem is the delay in tracking the torque profile, as shown in Fig. 15. To increase the control bandwidth, the motor with higher maximum velocity, and the control hardware with increased communication frequency can be used.

The proposed actuator has nonlinear stiffness behaviors. Based on reported works, the nonlinear behaviors have benefits in improving system stability and energy efficiency [25], [26], [27]. However, they make it difficult to model the actuator. Moreover, the compliance nonlinearity, as well as motor current and velocity limitations, bring nonlinear distortions [23] to the system, which reduces the tracking accuracy in actuator control. In future, the nonlinear distortions will be considered to improve the control performance.

In this work, the compliant actuator is tested with a test rig mounted on fixed support to calibrate its torque versus deflection characteristics and evaluate the performance of the proposed torque controller. In future, we will focus on the application of the compliant actuator in wearable exoskeletons for motion assistance [28]. The performance of the proposed torque controller will be evaluated in motion assistance tasks with humans.

ACKNOWLEDGMENT

The research is in part supported by Innovation Fund Denmark through Grand Solutions project Exo-aider. Z. Li acknowledges the CSC scholarship for his study at Aalborg University, Denmark. W. Chen and J. Zhang acknowledge the support of National Natural Science Foundation of China (Grant nos. 51675018 and 61773042).

REFERENCES

[1] V. Grosu, C. Rodriguez-Guerrero, S. Grosu, B. Vanderborght, D. Lefeber, Design of smart modular variable stiffness actuators for robotic-assistive devices, IEEE/ASME Trans. Mechatron. 22 (4) (2017) 1777–1785.

[2] G. Grioli, S. Wolf, M. Garabini, M. Catalano, E. Burdet, D. Caldwell, R. Carloni, W. Friedl, M. Grebenstein, M. Laffranchi, D. Lefeber, S. Stramigioli, N. Tsagarakis, M. van Damme, B. Vanderborght, A. Albu-Schaeffer, A. Bicchi, Variable stiffness actuators: The user's point of view, Int. J. Robot. Res. 34 (6) (2015) 727–743.

[3] A. D. Santis, B. Siciliano, A. D. Luca, A. Bicchi, An atlas of physical human–robot interaction, Mech. Mach. Theory 43 (3) (2008) 253–270.

[4] M. Gull, S. Bai, T. Bak, A review on design of upper limb exoskeletons, Robotics 9 (2020) 16.

[5] G. A. Pratt, M. M. Williamson, Series elastic actuators, in: IEEE/RSJ International Conference on Intelligent Robots and Systems (IROS). Human Robot Interaction and Cooperative Robots, Vol. 1, 1995, pp. 399–406.

[6] K. Kong, J. Bae, M. Tomizuka, Control of rotary series elastic actuator for ideal force-mode actuation in human–robot interaction applications, IEEE/ASME Trans. Mechatron. 14 (1) (2009) 105–118.

[7] K. Kong, J. Bae, M. Tomizuka, A compact rotary series elastic actuator for human assistive systems, IEEE/ASME Trans. Mechatron. 17 (2) (2012) 288–297.

[8] W. M. dos Santos, G. A. Caurin, A. A. Siqueira, Design and control of an active knee orthosis driven by a rotary series elastic actuator, Control Eng. Pract 58 (2017) 307–318.

[9] D. W. Haldane, M. M. Plecnik, J. K. Yim, R. S. Fearing, Robotic vertical jumping agility via series-elastic power modulation, Sci. Robot. 1 (1) (2016).

[10] S. Curran, D. E. Orin, Evolution of a jump in an articulated leg with series-elastic actuation, in: 2008 IEEE International Conference on Robotics and Automation (ICRA), 2008, pp. 352–358.

[11] D. W. Robinson, J. E. Pratt, D. J. Paluska, G. A. Pratt, Series elastic actuator development for a biomimetic walking robot, in: IEEE/ASME International Conference on Advanced Intelligent Mechatronics (AIM), 1999, pp. 561–568.

[12] J. W. Hurst, J. E. Chestnutt, A. A. Rizzi, An actuator with physically variable stiffness for highly dynamic legged locomotion, in: IEEE International Conference on Robotics and Automation (ICRA), Vol. 5, 2004, pp. 4662–4667.

[13] A. Jafari, N. G. Tsagarakis, D. G. Caldwell, A novel intrinsically energy efficient actuator with adjustable stiffness (AwAS), IEEE/ASME Trans. Mechatron. 18 (1) (2013) 355–365.

[14] A. Jafari, N. G. Tsagarakis, D. G. Caldwell, AwAS-II: A new actuator with adjustable stiffness based on the novel principle of adaptable pivot point and variable lever ratio, in: IEEE International Conference on Robotics and Automation (ICRA), 2011, pp. 4638–4643.

[15] L. Liu, S. Leonhardt, B. J. Misgeld, Design and control of a mechanical rotary variable impedance actuator, Mechatron. 39 (2016) 226–236.

[16] S. S. Groothuis, G. Rusticelli, A. Zucchelli, S. Stramigioli, R. Carloni, The variable stiffness actuator vsaUT-II: Mechanical design, modeling, and identification, IEEE/ASME Trans. Mechatron. 19 (2) (2014) 589–597.

[17] J. Sun, Z. Guo, D. Sun, S. He, X. Xiao, Design, modeling and control of a novel compact, energy-efficient, and rotational serial variable stiffness actuator (SVSA-II), Mech. Mach. Theory 130 (2018) 123–136.

[18] M. Dežman, A. Gams, Rotatable cam-based variable-ratio lever compliant actuator for wearable devices, Mech. Mach. Theory 130 (2018) 508–522.

[19] Z. Li, W. Chen, S. Bai, A novel reconfigurable revolute joint with adjustable stiffness, in: IEEE International Conference on Robotics and Automation (ICRA), 2019, pp. 8388–8393.

[20] J. Choi, S. Hong, W. Lee, S. Kang, M. Kim, A robot joint with variable stiffness using leaf springs, IEEE Trans. Robot. 27 (2) (2011) 229–238.

[21] Z. Li, S. Bai, O. Madsen, W. Chen, J. Zhang, Design, modeling and testing of a compact variable stiffness mechanism for exoskeletons, Mech. Mach. Theory 151 (2020) 103905.

[22] R.S. Figliola, D.E. Beasley, Theory and design for mechanical measurements, Wiley, 2010.

[23] M. Moltedo, G. Cavallo, T. Baček, J. Lataire, B. Vanderborght, D. Lefeber, C. Rodriguez-Guerrero, Variable stiffness ankle actuator for use in robotic-assisted walking: Control strategy and experimental characterization, Mech. Mach. Theory 134 (2019) 604–624.

[24] L. Liu, S. Leonhardt, C. Ngo, B. J. E. Misgeld, Impedance-Controlled Variable Stiffness Actuator for Lower Limb Robot Applications, IEEE Trans. Autom. Sci. Eng. 17 (2) (2020) 991–1004.

[25] S. Wolf, G. Grioli, O. Eiberger, W. Friedl, M. Grebenstein, H. Höppner, E. Burdet, D. G. Caldwell, R. Carloni, M. G. Catalano, et al., Variable stiffness actuators: review on design and components, IEEE/ASME Trans. Mechatron. 21 (5) (2016) 2418–2430.

[26] J. Austin, A. Schepelmann, H. Geyer, Control and evaluation of series elastic actuators with nonlinear rubber springs, in: IEEE/RSJ International Conference on Intelligent Robots and Systems, 2015, pp. 6563–6568.

[27] D. Owaki, A. Ishiguro, Enhancing stability of a passive dynamic running biped by exploiting a nonlinear spring, in: IEEE/RSJ International Conference on Intelligent Robots and Systems, 2006, pp. 4923–4928.

[28] L. Teng, M. A. Gull, S. Bai, PD based fuzzy sliding mode control of a wheelchair exoskeleton robot, IEEE/ASME Trans. Mechatron. (2020).

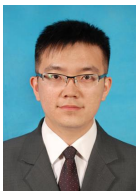

Zhongyi Li received the B.S. degree in mechanical engineering from Chongqing University of Technology, Chongqing, China, in 2012, and the M.S. degree in mechanical engineering from North China University of Technology, Beijing, China, in 2015. He is currently working torward the Ph.D degree at Aalborg University, under the guidance of Prof. Shaoping Bai. His research interests include serial elastic actuator, variable stiffness actuator and exoskeleton.

Muhammad Raza Ul Islam received his Masters degree (MS) in Electrical Engineering from COMSATS institute of Information Tech. (CIIT), Islamabad, Pakistan, 2013. After MS, he served as Research Assistant at CIIT. Currently, he is a PhD scholar at Dept. of Materials and Production, Aalborg University, Denmark since Aug. 2015. His research interests include control theory, industrial, medical and assistive robotics and exoskeleton, physical and cognitive human-robot interaction and artificial intelligence.

Weihai Chen received the B.S. degree in detection technology from Zhejiang University, Hangzhou, China, in 1982, and the M.S. and Ph.D. degrees in mechanical engineering from Beihang University, Beijing, China, in 1988 and 1996, respectively. He was an Associate Professor in 1999 and a Professor in 2007 with Beihang University, where he is currently the Director of the Intelligent Robotics and Measurement and Control Technology Laboratory. His research interests include bioinspired robotics, micromanipulation, and computer vision. Dr. Chen is a member of the Technical Committee on Manufacturing Automation of the IEEE Robotics and Automation Society, and a Senior Member of the Chinese Mechanical Engineering Society.

Jianbin Zhang obtained his B.Eng. and M.Eng. degrees from Beihang University, China, in 1983 and 1986, respectively. He is currently a Professor in the School of Mechanical Engineering and Automation, Beihang University, Beijing, China. His research interest is the engineering manufacturing and robotics.

Shaoping Bai is currently a Professor with the Department of Materials and Production, Aalborg University, Aalborg, Denmark. His research interests include dynamics and design, medical and assistive robots, parallel manipulators, and walking robots. Dr. Bai is a member of ASME and a senior member of IEEE ROBOTICS AND AUTOMATION and an Associate Editor for the ASME Journal Mechanisms and Robotics.

Chapter 8

Conclusions

The main scope of this research work covers the mechanical design, mathematical modeling and controlling of a novel compliant joint for upper-body exoskeletons. The compliant joint was developed based on a new mechanism which can adjust its stiffness in multiple modes. A unified stiffness model was developed for comprehensive stiffness analysis of the joint. The dynamics of the joint was analyzed, with which the natural frequency and bandwidth of the joint are acquired. A torque controller for the joint was developed and verified with both simulations and experiments.

8.1 Summary of papers

The research results are summarized in four articles.

Paper I

Paper I presents a new design of compliant joint mechanism. In this mechanism, adjustable stiffness is achieved by changing spring pretension. Moreover, the mechanism has nonlinear torque-deflection relationships whose behaviors is varying with different spring pretensions. Based on the mechanism, a revolute joint was developed. In the joint design, a reconfigurable concept was implemented, which is helpful in increasing the stiffness adjustment range of the joint. Then, the stiffness model of the joint was built for stiffness analysis with the effects of design parameters. Static tests were performed with a prototype to validate the developed stiffness model. The torque-deflection curves from experimental results match the ones predicted from stiffness model well, verifying the accuracy of the model. Furthermore, three stiffness behaviors, i.e. linear, softening and hardening behaviors can be obtained by changing the spring pretension, which is as expected.

In paper I, the revolute joint design was further optimized to be applicable for an upper-body exoskeleton. An embodiment of the optimized joint was presented in the article, which is very compact and light-weight. The size of the embodiment is 92 $\times$ 89 $\times$ 88 mm, and the total weight is 0.987 kg. The maximum torque and stiffness of the joint are 20 Nm and 75 Nm/rad, which can fit the torque and stiffness requirements in physical assistance for human upper-body.

Paper II

Paper II extends the work in paper I to develop a unified stiffness model of mechanisms with inherent compliance, which enables us to comprehensively analyze the stiffness performances of the mechanism presented in paper I. With this model, the basic stiffness characteristics which only relate to the geometry of the mechanism can be formulated, which facilitates the systematic stiffness analysis. Furthermore, based on the unified model, a new mechanism design approach for constructing mechanisms with desired stiffness behaviors was proposed, with illustrations of two design cases. Prototypes were built and tested. Experimental results show that the constructed mechanisms can exhibit desired stiffness behaviors as designed, verifying the feasibility of mechanism design approach, as well as the accuracy of the unified model.

Paper III

Paper III studies the dynamics of a novel compliant joint. This joint was designed with the mechanism proposed in paper I, thereby enabling adjustable stiffness. Torque and stiffness model were developed to investigate the static performance of the joint. Afterwards, dynamic model for the compliant joint was built, and dynamic analysis was performed to find its natural frequencies with stiffness variation. The mathematical models were verified with both static and dynamic experiments.

Testing results show that the designed joint can vary stiffness in adjustable ranges due to its reconfigurability. The natural frequencies of the joint can be changed widely through adjusting the joint stiffness. Moreover, the mechanism can be scalable to various applications through changing configuration and spring of different stiffness. In the paper, a design case illustrating the usage of the developed joint for an elbow exoskeleton was introduced. With the new joint, the exoskeleton can vary its stiffness in the range of [4.31, 56.13] Nm/rad, and can output a maximum torque of 11.69 Nm, which fits the torque and stiffness of human elbow joint.

Table 8.1. Torque sensing performance

Property	Value	
	$F_0^* = 20$ N	$F_0 = 60$ N
Range [Nm]	[-5.8, 5.8]	[-4.5, 4.5]
Repeatability	6.34% FS	8.6% FS
Hysteresis	3.16% FS	4.67% FS

* : F_0 denotes the spring pretension

Paper IV

Paper IV focuses on the mechatronics design of the compliant joint. The joint can be controlled to generate a desired torque through a proper joint deflection. Therefore, a torque control problem can be converted to a position problem. In the paper, static calibration tests were performed to obtain the torque sensing performance. The detailed performances are given in Table 8.1. Close-loop control of the joint can be realized using the VSM-based torque sensor. Both simulations and experiments were performed to validate the feasibility of actuator in controlling rotation and also torque.

The compliant joint is able to generate a low impedance in torque control, which is desirable to improve the system transparency when it interacts with human. In experiments, when the input torque signal is set to zero, the joint position can be controlled to follow the human motion well. The generated resistance torque to the human was measured by the VSM-based torque sensor. Results show that the resistance torque is affected by both human motion frequency and amplitude, as well as joint stiffness. A higher frequency, amplitude and joint stiffness result in a larger resistance torque.

8.2 Contributions

The work in this thesis is focused on developing a novel compliant joint for upper-body exoskeletons to increase pHRI safety and comfort. The main contributions are described as follows:

- Novel design of compliant joint mechanism with reconfigurability was proposed. The new mechanism has capacity to vary stiffness in three working modes, e.g. linear, softening and hardening modes. As far as the author's knowledge, this is the first time that these three working modes are realized in a compliant joint. Moreover, spring preload based approach was adopted in stiffness adjustment of the new mechanism.

Compared with other mechanisms based on spring preload based approach, the new design enables an enlarged stiffness range due to its reconfigurability.

- Secondly, a unified stiffness model of compliant joint mechanism was built and experimentally validated. The model allows us to comprehensively study the stiffness performance of the mechanism, with which the influences of design parameters can be analyzed readily, and all possible stiffness behaviors in the mechanism can be found and investigated. The developed model can be applied to other mechanisms with inherent compliance.

- A unified stiffness model was developed to analyze stiffness behaviors. With the unified model, it is possible to achieve a desired stiffness behavior by proper compliance design. Two design cases were illustrated to validate the method. More new mechanism designs for desired stiffness behaviors could be implemented using this approach.

- Mechatronics design of the compliant joint for upper-body exoskeleton was proposed. The joint is designed with the variable stiffness mechanism, which enables adjustable stiffness, thereby allowing the actuator to change system impedance for safe control. The developed joint has a self-sensing function to measure torque, with high sensitivity to small load, which makes possible to control torque accurately.

8.3 Future work

The following research works could be considered in the future:

- Design optimization will be implemented to get a compact and lightweight design of compliant joint for the wearable exoskeletons applications. Through optimization of the mechanical design, the size and weight of proposed compliant joints can be reduced.

- The proposed compliant joints have nonlinear stiffness behaviors which have benefits in improving system stability and energy efficiency. However, nonlinear behaviors bring nonlinear distortions to the system, which reduces the tracking accuracy in both joint position control and torque control. In future, the nonlinear distortions will be considered in designing controller to improve control performance.

- As introduced in Chapters 6 and 7, the compliant joint developed can achieve a very low compliance and a very large joint deflection angle, which has benefits in increasing the safety of the actuator to impact

loads. It has to be noted that the low compliance also reduces the control bandwidth. With low joint compliance, the motor must be controlled to generate a large joint deflection to achieve a desired torque. In other words, the motor should be worked in a high velocity level, so that the desired torque can be reached in time. However, this cannot be done as expected, due to the velocity limitation of motor. Moreover, the control response is limited by the communication frequency in control hardware. A common problem is the delay in tracking the torque profile. To increase the control bandwidth, the motor with higher maximum velocity, and the control hardware with increased communication frequency can be used.

- In this work, a novel compliant joint mechanism has been developed for the active upper-body exoskeleton. In future, interesting work is to employ this mechanism in the design of passive exoskeleton. This can be done in the fact that the mechanism is able to produce both active and negative stiffness behaviors which are essential for gravity compensation. Parts of this work including a virtual embodiment of passive lower-body exoskeleton have been completed. Other works including prototyping and testing will be studied.

Bibliography

[1] G. A. Pratt and M. M. Williamson. Series elastic actuators. In *Proceedings 1995 IEEE/RSJ International Conference on Intelligent Robots and Systems. Human Robot Interaction and Cooperative Robots*, vol. 1, p. 399–406, 1995.

[2] R. Brooks, C. Breazeal, M. Marjanovic, B. Scassellati, and M. Williamson,. Cog Project: Building a Humanoid Robot. In *Computation for Metaphors, Analogy and Agents*, 1998.

[3] R. Van Ham, B. Vanderborght, M. Van Damme, B. Verrelst, and D. Lefeber. MACCEPA, the mechanically adjustable compliance and controllable equilibrium position actuator: design and implementation in a biped robot. *Robotics and Autonomous Systems*, 55(10):761–768, 2007.

[4] M. A. Gull, S. Bai, and T. Bak. A review on design of upper limb exoskeletons. *Robotics*, 9(16), 2020.

[5] S. Christensen and S. Bai. Kinematic analysis and design of a novel shoulder exoskeleton using a double parallelogram linkage. *Journal of Mechanisms and Robotics*, 10(4):041008, 2018.

[6] T. Nef, M. Guidali, and R. Riener. ARMin III–arm therapy exoskeleton with an ergonomic shoulder actuation. *Applied Bionics and Biomechanics*, 6(2):127–142, 2009.

[7] X. Cui, W. Chen, X. Jin, and S. K. Agrawal. Design of a 7-dof cable-driven arm exoskeleton (CAREX-7) and a controller for dexterous motion training or assistance. *IEEE/ASME Transactions on Mechatronics*, 22(1):161–172, 2017.

[8] L. Zhou, S. Bai, M. S. Andersen, and J. Rasmussen. Modeling and design of a spring-loaded, cable-driven, wearable exoskeleton for the upper extremity. *Modeling, Identification and Control*, 36(3):167–177, 2015.

[9] L. Bishop and J. Stein. Three upper limb robotic devices for stroke rehabilitation: A review and clinical perspective. *NeuroRehabilitation*, 33(1):3–11, 2013.

[10] Y. Sankai. HAL: hybrid assistive limb based on cybernics. In *Robotics Research*, p. 25–34, 2011.

[11] R.A.R.C. Gopura, D.S.V. Bandara, K. Kiguchi, and G.K.I. Mann. Developments in hardware systems of active upper-limb exoskeleton robots: a review. *Robotics and Autonomous Systems*, 75:203–220, 2016.

[12] L. Zhou, W. Chen, W. Chen, S. Bai, J. Zhang, and J. Wang. Design of a passive lower limb exoskeleton for walking assistance with gravity compensation. *Mechanism and Machine Theory*, 150:103840, 2020.

[13] S. Wang, L. Wang, C. Meijneke, E. van Asseldonk, and T. Hoellinger et al. Design and control of the mindwalker exoskeleton. *IEEE Transactions on Neural Systems and Rehabilitation Engineering*, 23(2):277–286, 2015.

[14] B. Kim and A. D. Deshpande. An upper-body rehabilitation exoskeleton harmony with an anatomical shoulder mechanism: design, modeling, control, and performance evaluation. *The International Journal of Robotics Research*, 36(4):414–435, 2017.

[15] N. Vitiello, T. Lenzi, S. Roccella, S. M. M. De Rossi, and E. Cattin et al. NEUROExos: a powered elbow exoskeleton for physical rehabilitation. *IEEE Transactions on Robotics*, 29(1):220–235, 2013.

[16] J. Meuleman, E. van Asseldonk, G. van Oort, H. Rietman, and H. van der Kooij. Lopes II–design and evaluation of an admittance controlled gait training robot with shadow-leg approach. *IEEE Transactions on Neural Systems and Rehabilitation Engineering*, 24(3):352–363, 2016.

[17] O. Baser and H. Kizilhan. Mechanical design and preliminary tests of VS-AnkleExo. *Journal of the Brazilian Society of Mechanical Sciences and Engineering*, 40(9):442, 2018.

[18] L. Liu, S. Leonhardt, and B. J. E. Misgeld. Experimental validation of a torque-controlled variable stiffness actuator tuned by gain scheduling. *IEEE/ASME Transactions on Mechatronics*, 23(5):2109–2120, 2018.

[19] S. Wolf, G. Grioli, O. Eiberger, and W. Friedl et al. Variable stiffness actuators: review on design and components. *IEEE/ASME transactions on mechatronics*, 21(5):2418–2430, 2016.

[20] J. Austin, A. Schepelmann, and H. Geyer. Control and evaluation of series elastic actuators with nonlinear rubber springs. In *IEEE/RSJ International Conference on Intelligent Robots and Systems*, p. 6563–6568, 2015.

[21] D. Owaki and A. Ishiguro. Enhancing stability of a passive dynamic running biped by exploiting a nonlinear spring. In *IEEE/RSJ International Conference on Intelligent Robots and Systems*, p. 4923–4928, 2006.

[22] Y. Zhao, Z. Song, T. Ma, and J. S. Dai. Optimization of stiffness to achieve increased bandwidth and torque resolution in nonlinear stiffness actuators. *IEEE Transactions on Industrial Electronics*, 67(4):2925–2935, 2020.

[23] W. Roozing, J. Malzahn, N. Kashiri, D. G. Caldwell, N. G. Tsagarakis. On the stiffness selection for torque-controlled series-elastic actuators. *IEEE Robotics and Automation Letters*, 2(4):2255–2262, 2017.

[24] R. V. Ham, T. G. Sugar, B. Vanderborght, K. W. Hollander, and D. Lefeber. Compliant actuator designs. *IEEE Robotics Automation Magazine*, 16(3):81–94, 2009.

[25] B. Vanderborght, A. Albu-Schäffer, A. Bicchi, and E. Burdet et al. Variable impedance actuators: a review. *Robotics and autonomous systems*, 61(12):1601–1614, 2013.

[26] H. Yu, S. Huang, N. V. Thakor, G. Chen, S. Toh, M. Sta Cruz, Y. Ghorbel, and C. Zhu. A novel compact compliant actuator design for rehabilitation robots. In *2013 IEEE 13th International Conference on Rehabilitation Robotics (ICORR)*, p. 1–6, 2013.

[27] H. Yu, S. Huang, G. Chen, Y. Pan, and Z. Guo. Human–robot interaction control of rehabilitation robots with series elastic actuators. *IEEE Transactions on Robotics*, 31(5):1089–1100, 2015.

[28] K. Kong, J. Bae, and M. Tomizuka. Control of rotary series elastic actuator for ideal force-mode actuation in human–robot interaction applications. *IEEE/ASME transactions on mechatronics*, 14(1):105–118, 2009.

[29] K. Kong, J. Bae, and M. Tomizuka. A compact rotary series elastic actuator for human assistive systems. *IEEE/ASME Transactions on Mechatronics*, 17(2):288–297, 2012.

[30] W. M dos Santos, G. AP Caurin, and A. AG Siqueira. Design and control of an active knee orthosis driven by a rotary series elastic actuator. *Control Engineering Practice*, 58:307–318, 2017.

[31] S. Kim and J. Bae. Force-mode control of rotary series elastic actuators in a lower extremity exoskeleton using model-inverse time delay control. *IEEE/ASME Transactions on Mechatronics*, 22(3):1392–1400, 2017.

[32] S. Curran and D. E. Orin. Evolution of a jump in an articulated leg with series-elastic actuation. In *2008 IEEE International Conference on Robotics and Automation*, p. 352–358, 2008.

[33] D. W. Haldane, M. M. Plecnik, J. K. Yim, and R. S. Fearing. Robotic vertical jumping agility via series-elastic power modulation. *Science Robotics*, 1(1), 2016.

[34] T. Verstraten, P. Beckerle, R. Furnémont, G. Mathijssen, B. Vanderborght, and Dirk Lefeber. Series and parallel elastic actuation: impact of natural dynamics on power and energy consumption. *Mechanism and Machine Theory*, 102:232–246, 2016.

[35] Z. Li, S. Bai, O. Madsen, W. Chen, and J. Zhang. Design, modeling and testing of a compact variable stiffness mechanism for exoskeletons. *Mechanism and Machine Theory*, 151:103905, 2020.

[36] T. G. Sugar. A novel selective compliant actuator. *Mechatronics*, 12(9):1157–1171, 2002.

[37] P. Beyl, K. Knaepen, S. Duerinck, M. Van Damme, B. Vanderborght, R. Meeusen, and D. Lefeber. Safe and compliant guidance by a powered knee exoskeleton for robot-assisted rehabilitation of gait. *Advanced Robotics*, 25(5):513–535, 2011.

[38] C. Everarts, B. Dehez, and R. Ronsse. Variable stiffness actuator applied to an active ankle prosthesis: principle, energy-efficiency, and control. In *2012 IEEE/RSJ International Conference on Intelligent Robots and Systems*, p. 323–328, 2012.

[39] H. Vu Quy, L. Aryananda, F. I. Sheikh, F. Casanova, and R. Pfeifer. A novel mechanism for varying stiffness via changing transmission angle. In *2011 IEEE International Conference on Robotics and Automation*, p. 5076–5081, 2011.

[40] K. C. Galloway, J. E. Clark, and D. E. Koditschek. Variable stiffness legs for robust, efficient, and stable dynamic Running. *Journal of Mechanisms and Robotics*, 5(1), 2013.

[41] J. W. Hurst. The electric cable differential leg: a novel design approach for walking and running. *International Journal of Humanoid Robotics*, 8(2):301–321, 2011.

[42] A. Jafari, N. G. Tsagarakis, B. Vanderborght, and D. G. Caldwell. A novel actuator with adjustable stiffness (AwAS). In *2010 IEEE/RSJ International Conference on Intelligent Robots and Systems*, p. 4201–4206, 2010.

[43] A. Jafari, N. G. Tsagarakis, and D. G. Caldwell. A novel intrinsically energy efficient actuator with adjustable stiffness (AwAS). *IEEE/ASME transactions on mechatronics*, 18(1):355–365, 2013.

[44] N. G. Tsagarakis, I. Sardellitti, and D. G. Caldwell. A new variable stiffness actuator (CompAct-VSA): Design and modelling. In *2011 IEEE/RSJ International Conference on Intelligent Robots and Systems (IROS)*, p. 378–383. IEEE, 2011.

[45] L. C. Visser, R. Carloni, and S. Stramigioli. Energy-efficient variable stiffness actuators. *IEEE Transactions on Robotics*, 27(5):865–875, 2011.

[46] S. S. Groothuis, G. Rusticelli, A. Zucchelli, S. Stramigioli, and R. Carloni. The variable stiffness actuator vsaUT-II: mechanical design, modeling, and identification. *IEEE/ASME Transactions on Mechatronics*, 19(2):589–597, 2014.

[47] H. Q. Vu, H. Hauser, D. Leach, and R. Pfeifer. A variable stiffness mechanism for improving energy efficiency of a planar single-legged hopping robot. In *2013 16th International Conference on Advanced Robotics (ICAR)*, p. 1–7, 2013.

[48] H. Q. Vu and L. G. Marcantini. Knee stiffness adjustment for energy efficient locomotion of a legged robot on surfaces with different stiffness. In *2013 IEEE International Conference on Robotics and Biomimetics (ROBIO)*, p. 1825–1831, 2013.

[49] K. W. Hollander, T. G. Sugar, and D. E. Herring. Adjustable robotic tendon using a 'Jack Spring'. In *9th International Conference on Rehabilitation Robotics*, p. 113–118, 2005.

[50] K. W. Hollander, T. G. Sugar, and D. E. Herring. A robotic Jack Spring for ankle gait gssistance. In *International Design Engineering Technical Conferences and Computers and Information in Engineering Conference*, p. 25–34, 2005.

[51] T. Morita and S. Sugano. Design and development of a new robot joint using a mechanical impedance adjuster. In *Proceedings of 1995 IEEE International Conference on Robotics and Automation*, vol. 3, p. 2469–2475, 1995.

[52] S. S. Bi, C. Liu, H. Z. Zhao, and Y. L. Wang. Design and analysis of a novel variable stiffness actuator based on parallel-assembled-folded serial leaf springs. *Advanced Robotics*, 31(18):990–1001, 2017.

[53] J. Choi, S. Hong, W. Lee, S. Kang, and M. Kim. A robot joint with variable stiffness using leaf springs. *IEEE Transactions on Robotics*, 27(2):229–238, 2011.

[54] L. Liu, S. Leonhardt, C. Ngo, and B. J. E. Misgeld. Impedance-controlled variable stiffness actuator for lower limb robot applications. *IEEE Transactions on Automation Science and Engineering*, 17(2):991–1004, 2020.

[55] S. Wolf, G. Grioli, O. Eiberger, and W. Friedl et al. Variable stiffness actuators: review on design and components. *IEEE/ASME Transactions on Mechatronics*, 21(5):2418–2430, 2016.

[56] S. A. Migliore, E. A. Brown, and S. P. DeWeerth. Biologically inspired joint stiffness control. In *Proceedings of the 2005 IEEE International Conference on Robotics and Automation*, p. 4508–4513, 2005.

[57] T. Noda, T. Teramae, B. Ugurlu, and J. Morimoto. Development of an upper limb exoskeleton powered via pneumatic electric hybrid actuators with bowden cable. In *2014 IEEE/RSJ International Conference on Intelligent Robots and Systems*, p. 3573–3578, 2014.

[58] B. Vanderborght, N. G. Tsagarakis, C. Semini, R. Van Ham, and D. G. Caldwell. MACCEPA 2.0: adjustable compliant actuator with stiffening characteristic for energy efficient hopping. In *IEEE International Conference on Robotics and Automation*, p. 544–549, 2009.

[59] S. Wolf and G. Hirzinger. A new variable stiffness design: matching requirements of the next robot generation. In *IEEE International Conference on Robotics and Automation*, p. 1741–1746, 2008.

[60] S. Wolf, O. Eiberger, and G. Hirzinger. The DLR FSJ: Energy based design of a variable stiffness joint. In *2011 IEEE International Conference on Robotics and Automation*, p. 5082–5089, 2011.

[61] J. Park, H. Kim, and J. Song. Safe robot arm with safe joint mechanism using nonlinear spring system for collision safety. In *2009 IEEE International Conference on Robotics and Automation*, p. 3371–3376, 2009.

[62] D. Hyun, H. S. Yang, J. Park, and Y. Shim. Variable stiffness mechanism for human-friendly robots. *Mechanism and Machine Theory*, 45(6):880–897, 2010.

[63] V. Grosu, C. R.-Guerrero, S. Grosu, B. Vanderborght, and D. Lefeber. Design of smart modular variable stiffness actuators for robotic-assistive devices. *IEEE/ASME Transactions on Mechatronics*, 22(4):1777–1785, 2017.

[64] J. Vantilt, K. Tanghe, M. Afschrift, and A. K.B.D Bruijnes et al. Model-based control for exoskeletons with series elastic actuators evaluated on sit-to-stand movements. *Journal of Neuroengineering and Rehabilitation*, 16(1):65, 2019.

[65] M. Moltedo, T. Bacek, K. Junius, B. Vanderborght, and D. Lefeber. Mechanical design of a lightweight compliant and adaptable active ankle foot orthosis. In *2016 6th IEEE International Conference on Biomedical Robotics and Biomechatronics (BioRob)*, p. 1224–1229, 2016.

[66] M. Moltedo, T. Baek, K. Langlois, K. Junius, B. Vanderborght, and D. Lefeber. Design and experimental evaluation of a lightweight, high-torque and compliant actuator for an active ankle foot orthosis. In *2017 International Conference on Rehabilitation Robotics (ICORR)*, p. 283–288, 2017.

[67] M. Moltedo, G. Cavallo, T. Baek, J. Lataire, B. Vanderborght, D. Lefeber, and C. R.-Guerrero. Variable stiffness ankle actuator for use in robotic-assisted walking: Control strategy and experimental characterization. *Mechanism and Machine Theory*, 134:604–624, 2019.

[68] T. Bacek, M. Moltedo, C. R.-Guerrero, J. Geeroms, B. Vanderborght, and D. Lefeber. Design and evaluation of a torque-controllable knee joint actuator with adjustable series compliance and parallel elasticity. *Mechanism and Machine Theory*, 130:71 – 85, 2018.

[69] Y. Liu, X. Liu, Z. Yuan, and J. Liu. Design and analysis of spring parallel variable stiffness actuator based on antagonistic principle. *Mechanism and Machine Theory*, 140:44–58, 2019.

[70] R. Furnémont, G. Mathijssen, T. van der Hoeven, B. Brackx, D. Lefeber, and B. Vanderborght. Torsion MACCEPA: a novel compact compliant actuator designed around the drive axis. In *2015 IEEE International Conference on Robotics and Automation (ICRA)*, p. 232–237, 2015.

[71] Y.-S. Wu and C.-C. Lan. Linear variable-stiffness mechanisms based on preloaded curved beams. *Journal of Mechanical Design*, 136(12):122302, 2014.

[72] Z. Li, W. Chen, and S. Bai. A novel reconfigurable revolute joint with adjustable stiffness. In *IEEE International Conference on Robotics and Automation*, p. 8388–8393, 2019.

[73] Z. Li, and S. Bai. A novel revolute joint of variable stiffness with reconfgurability. *Mechanism and Machine Theory*, 133:720–736, 2019.

[74] A. Omer, R. Ghorbani, K. Hashimoto, H.O. Lim, and A. Takanishi. A novel design for adjustable stiffness artificial tendon for the ankle joint of a bipedal robot: modeling and simulation. *Machines*, 4(1):1–22, 2015.

[75] L. Xiang, Y. Pan, G. Chen, and H. Yu. Continuous tracking control for a compliant actuator with two-stage stiffness. *IEEE Transactions on Automation Science and Engineering*, 15 (1):57–66, 2018.

[76] J. Park, B. Kim, and J. Song,. Safe link mechanism based on passive compliance for safe human-robot collision. In *IEEE International Conference on Robotics and Automation*, p. 1152–1157, 2007.

[77] J. Park, Y. Lee, J. Song, and H. Kim. Safe joint mechanism based on nonlinear stiffness for safe human-robot collision. In *IEEE International Conference on Robotics and Automation*, p. 2177–2182, 2008.

[78] J. Park, and J. Song. A nonlinear stiffness safe joint mechanism design for human robot interaction. *Journal of Mechanical Design*, 132(6):061105, 2010.

[79] R.R. Torrealba, and S.B. Udelman. Design of cam shape for maximum stiffness variability on a novel compliant actuator using differential evolution. *Mechanism and Machine Theory*, 95:114–124, 2016.

[80] C.-P. Chou, and B. Hannaford. Measurement and modeling of mckibben pneumatic artificial muscles. *IEEE Transactions on Robotics and Automation*, 12 (1):90–102, 1996.

[81] B. Verrelst, R. Van Ham, B. Vanderborght, F. Daerden, and D. Lefeber. The pneumatic biped LUCY actuated with pleated pneumatic artificial muscles. *Autonomous Robots*, 18 (13):201–213, 2005.

[82] D. W. Robinson, J. E. Pratt, D. J. Paluska, and G. A. Pratt. Series elastic actuator development for a biomimetic walking robot. In *IEEE/ASME International Conference on Advanced Intelligent Mechatronics*, p. 561–568, 1999.

[83] D. W. Robinson. Series elasticity in closed-loop actuator force control. PhD Thesis, *Department of Mechanical Engineering, Massachusetts Institute of Technology*, 2000.

[84] F. Sergi, D. Accoto, G. Carpino, N.L. Tagliamonte, and E. Guglielmelli. Design and characterization of a compact rotary series elastic actuator for knee assistance during overground walking. In *IEEE RAS/EMBS International Conference on Biomedical Robotics and Biomechatronics*, p. 1931–1936, 2012.

[85] H. Vallery, R. Ekkelenkamp, H. van der Kooij, and M. Buss. Passive and accurate torque control of series elastic actuators. In *Proceedings of the IEEE/RSJ International Conference on Mechatronic and Embedded Systems and Applications*, p. 1–6, 2006.

[86] G. Wyeth. Control issues for velocity sourced series elastic actuators. In *Proceedings of the Australasian Conference on Robotics and Automation*, 2006.

[87] L. Liu, S. Leonhardt, and B. J. Misgeld. Design and control of a mechanical rotary variable impedance actuator. *Mechatronic*, 39:226–236, 2016.

[88] M. Grun, R. Muller, U. Konigorski. Model based control of series elastic actuators. In *IEEE RAS/EMBS International Conference on Biomedical Robotics and Biomechatronics*, p. 538–543, 2012.

ISSN (online): 2446-1636
ISBN (online): 978-87-7210-689-2 AALBORG UNIVERSITY PRESS